COMPUTATIONAL STUDIES INTO TRANSITION METAL CATALYZED

CROSS-COUPLING REACTIONS

by

JENNA ALISE BILBREY

(Under the Direction of Jason Locklin)

ABSTRACT

This thesis discusses mechanistic aspects of transition metal catalyzed cross-coupling reactions. Improved methods for quantifying sterics in a transition metal complex are presented in Chapters 2 and 3 with the exact cone angle and the exact solid angle. These methods provide insight into the role sterics play in such catalytic complexes. Additionally, as these methods can use computationally obtained structures to quantify sterics, a change in sterics can be tracked over the course of a reaction to further understand the dynamics of transition metal complexes. Chapters 4–7 details mechanistic properties of two popular cross-coupling methods, Kumada and Stille cross-coupling, which can be modified for the synthesis of conjugated polymers. Of particular interest is the oxidative addition step in the reaction cycle, discussed in Chapters 5–7, which must occur through an intramolecular insertion method for polymerizations to be chain-growth in character and produce polymer of controlled molecular weight and narrow dispersity.

INDEX WORDS: Exact Cone Angle, Exact Solid Angle, Kumada Catalyst-Transfer Polycondensation, Stille Cross-Coupling, Disproportionation, Intramolecular Oxidative Addition

COMPUTATIONAL STUDIES INTO TRANSITION METAL CATALYZED

CROSS-COUPLING REACTIONS

by

JENNA ALISE BILBREY

B.S., The University of West Florida, 2009

A Dissertation Submitted to the Graduate Faculty of The University of Georgia in Partial

Fulfillment of the Requirements for the Degree

DOCTOR OF PHILOSOPHY

ATHENS, GEORGIA

2014

COMPUTATIONAL STUDIES INTO TRANSITION METAL CATALYZED

CROSS-COUPLING REACTIONS

by

JENNA ALISE BILBREY

Major Professor: Jason Locklin

Committee: Wesley D. Allen

Tina T. Salguero

Electronic Version Approved:

Maureen Grasso

Dean of the Graduate School

The University of Georgia

May 2014

DEDICATION

For Kitty and Tim and Mom and Dad and Ross and Ty and Chrissy and Claire and Chloe and

Cate and Logan, and not necessarily in that order.

"Research is what I'm doing when I don't know what I'm doing."

— Wernher von Braun

"If we knew what it was we were doing, it would not be called research, would it?"

— Albert Einstein

TABLE OF CONTENTS

LIST OF TABLES

LIST OF FIGURES

CHAPTER 1

INTRODUCTION AND LITERATURE REVIEW

Introduction to Conjugated Polymers

Conjugated polymers (CPs) are prevalent not only in academic research but in commercial applications as well.[1,2] Organic CPs are a particularly interesting semiconductor material due to variable mechanical flexibility and optical properties—depending on the polymeric structure, CPs can be transparent or have tunable absorptions and/or emissions. Transparent solar cells, bendable electronic paper, and stretchable electronic displays, all made of organic CPs, are already present in academic laboratories.[3-5]

Polythiophenes were one of the first materials used to model charge transport in CPs, favored for processing ease, corrosion resistance, and structural versatility.[6] The use of thiophene oligomers for photovoltaics[7] expanded to thiophene polymers, where much progress has been made in the optimization of charge carrier generation, separation, mobility, and collection.[8-10] In organic electronic devices, neutral polythiophenes act as p-type materials by donating electrons to n-type materials. Polythiophenes can undergo both p-type and n-type doping through electrochemical methods and are highly stable in both doped and undoped states.[11] Often, polythiophene is the polymer of choice when studying a new method of polymerization.

So far, the majority of experimental work has revolved around the polymerization of p-type conjugated polymers, which work as donor moieties.[12,13] However, many groups are now expanding these methods to n-type materials.[14,15] These unique materials act as acceptor moieties

and have the potential to replace conventional fullerene derivatives in photovoltaic devices.[16] A method to polymerize both p-type and n-type polymers simultaneously would be preferred, as alternating donor-acceptor block copolymers have been shown to enhance efficiencies in polymer photovoltaics.[17-19]

CPs are made by two general methods: chemical or electrochemical syntheses.[6,20-22] We have chosen to study chemical methods for synthesizing CPs to obtain a controlled film growth with low dispersity and uniform end groups. To have a highly controlled polymerization and result in homogeneous polymer chains, the polymerization must work through a chain-growth mechanism.[12,21,23] A suitable mechanism will be chain-growth in nature and display "living" characteristics, which includes a linear relationship between monomer conversion and number average molecular weight (M_n), M_n control based on the monomer:catalyst ratio, and the formation of block copolymers with sequential addition of a second monomer.[21] Understanding the characteristics of a potential mechanism will clarify the monomer scope, determine reaction conditions, and potentially avoid unforeseen pitfalls.

My dissertation work has revolved around computational studies of transition metal catalyzed polymerization of conjugated polymers, specifically Kumada catalyst-transfer polycondensation (KCTP) and Stille cross-coupling polymerization, which are discussed in Chapters 4–7. The general reaction involves cross-coupling of two aryl species through the use of AB-type monomers and a zerovalent group 10 transition metal catalyst (Fig. 1.1). In the first step of the reaction cycle, the zerovalent metal undergoes oxidative addition (OA) with the aryl–halogen bond of the substrate. The now divalent metal undergoes transmetalation (TM) with a metalating agent, a Grignard reagent in Kumada coupling or an organotin reagent in Stille coupling, to bind the second aryl group to the metal center. Finally, reductive elimination (RE)

occurs to form the final cross-coupled product and regenerate the zerovalent catalyst. There is much discussion that after RE the zerovalent complex does not diffuse away from the ring, but rather forms a π-complex.[23,24] This topic is the focus of discussion in Chapters 5–7.

In the process of elucidating polymerization mechanisms, it came to my attention that steric descriptors, specifically the cone angle and solid angle, were outdated and/or not applicable to a wide range of ligand types. Chapters 2 and 3 present new mathematical improvements to both the cone angle and solid angle methods, so that both may be applicable to any ligand in any conformation bound to any atom center.[25,26] The improved mathematics allows for the steric size to be calculated for a complex in a specific conformation rather than using universal descriptors for a ligand as with previous methods. This opens up the ability to track the sterics over the course of a reaction through computational modeling. With this mapping, steric influences of a mechanism can be further understood, as demonstrated in Chapters 6 and 7.
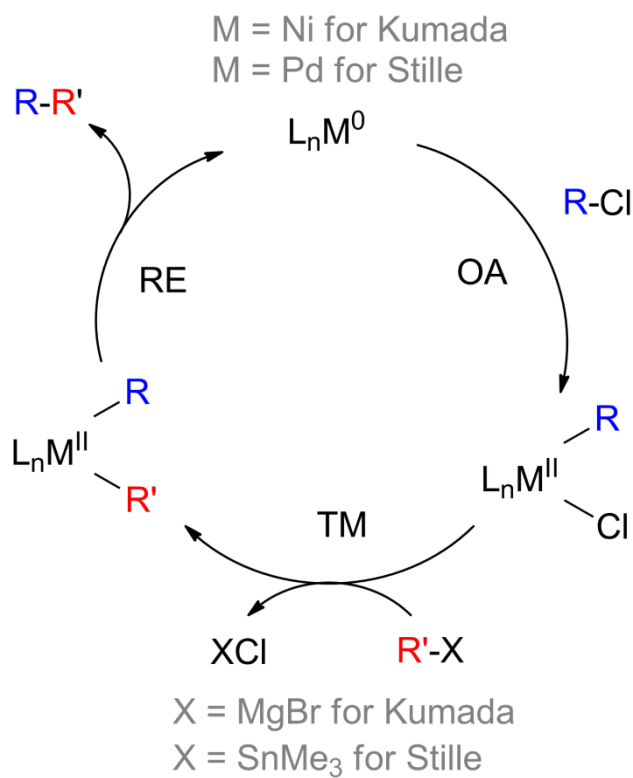
Figure 1.1. Representative scheme for Kumada and Stille cross-coupling reactions.

Computational Methods

The accuracy of any modeled system depends on the theoretical method used and the mathematical model of orbitals, called the basis set.[27] The computational methods used in this dissertation to compute molecular geometries, vibrational frequencies, and energetics are based off of density functional theory (DFT), specifically the B3LYP functional.[28,29] DFT was chosen over other *ab initio* methods to limit computational costs arising from the size of the studied complexes and the inclusion of transition metals.

DFT defines the electronic energy of a system as an electron probability density (ρ) in terms of a functional $E[\rho]$.[30,31] For a given system, the ground-state energy and electronic properties are defined by the electron density.[32] As all properties rely on the computation of the density, the functional must be chosen carefully. Though there is a theoretical functional that will exactly relate the density to the energy, none has yet been found. Instead researchers have formulated a variety of functionals, developed either empirically, though quantum mechanical definitions, or a combination thereof.

The energy of a system can be computed through the Kohn–Sham formalism, which proposes a reference system of non-interacting electrons whose density is equal to that of a system of fully interacting electrons.[33] The ground state electronic energy with *n* electrons and *N* nuclei can be found by the following equation:

$$E[\rho] = -\frac{1}{2}\sum_{i=1}^{n}\int \psi_i^*(r_1)\nabla_i^2\psi_i(r_1)\mathrm{d}r_1 - \sum_{X=1}^{N}\int \frac{Z_X}{r_{Xi}}\rho(r_1)\mathrm{d}r_1$$

$$+ \frac{1}{2}\iint \frac{\rho(r_1)\rho(r_2)}{r_{12}}\mathrm{d}r_1\mathrm{d}r_2 + E^{XC}[\rho]. \tag{1}$$

This equation is a variation of the Schrödinger equation used with wavefunction-based methods where the first term describes the kinetic energy of non-interaction electrons, the second term describes nuclear–electronic interactions, the third term describes Coulombic repulsions between

two electrons, and the fourth term describes the exchange and correlation of interacting electrons. Differences in this equation versus the Hartree-Fock Schrödinger equation include ψ as Kohn-Sham orbitals and the use of electron density ρ to describe electronic interactions.

The density can be written as a set of Kohn-Sham orbitals with the equation:

$$\rho(r) = \sum_{i=1}^{n} |\psi_i(r)|^2. \tag{2}$$

where the orbitals (ψ) are determined with application of the variational principle to the electronic energy, similar to what is done in Hartree-Fock calculations. It should be noted that increasing the number of orbitals (by increasing the basis set) does not guarantee increased accuracy in DFT methods, as opposed to Hartree-Fock methods where larger basis sets, in principle, lead to more exact results.

The biggest challenge to the Kohn-Sham method is the formulation of the exchange–correlation term E^{XC}. This term can be decomposed into two terms: the exchange term E^X and the correlation term E^C. Both of these terms are functionals of the electron density and are called the exchange functional and the correlation functional, respectively. As opposed to the Hartree-Fock method, the exchange potential is not exact; instead, the Kohn-Sham method uses an effective potential to model both the exchange and correlation effects.[31]

In the popular B3LYP functional, which is used throughout this dissertation, the exchange–correlation term is described by a generalized gradient approximation (GGA), where both the exchange and the correlation energies depend on the density as well as the gradient of the density. This exchange–correlation is combined with a percentage of Hartree-Fock (HF) exchange to create a hybrid density functional. The Becke88 (B) exchange functional[34] appended with the Lee, Yang, Parr (LYP) correlation functional[28] forms an exchange–correlation functional specific to B3LYP:

$$E_{xc}^{\text{B3LYP}} = E_x^{\text{LDA}} + a_0(E_x^{\text{HF}} - E_x^{\text{LDA}}) + a_x(E_x^{\text{GGA}} - E_x^{\text{LDA}}) + E_c^{\text{LDA}} + a_c(E_c^{\text{GGA}} - E_c^{\text{LDA}}). \quad (3)$$

where the three parameters (hence, the 3 in B3LYP) are $a_0 = 0.20$, $a_x = 0.72$, and $a_c = 0.81$.[29]

The density is dependent on three coordinates, regardless of the number of electrons in the system.[35] This is contrary to wavefunction-based methods where systems of n electrons depends on $4n$ coordinates. Thus, the scaling based on system size and, therefore, the computational cost is less with DFT [$O(\text{N}^3)$] than with wavefunction methods [$O(\text{N}^4)$ or higher].

In all molecular systems, especially those containing transition metals, the geometry optimization step is highly important as one is often looking for minima and saddle points on the potential energy surface in order to model a reaction.[36] While relativistic corrections introduced by relativistic effective core potentials are sufficient to model second- and third-row transition metal complexes,[37] first-row transition metal complexes are not computed so easily. Near degeneracies arising from compact 3d orbitals, which are often used in bonding, lead to multireference character that isn't well-described by single references methods such as HF or MP2.[38] In fact, in the study of ligand insertion with first-row transition metal carbonyls, the Møller-Plesset perturbation series failed to optimize to a single geometry, instead oscillating between the reactant, the transition state, and an intermediate.[39,40]

The systems studied herein are much too large to consider multireference *ab initio* methods. However, DFT, especially with the B3LYP functional, has been shown to be both accurate and efficient in dealing with large systems.[36,41,42] In the case above, where Møller-Plesset perturbation failed to achieve accurate geometries, the B3LYP functional was able to give results in agreement with higher order electron correlation methods, such as coupled cluster methods, experimentally estimated energetics, and X-ray structures.[39,40]

DFT methods are less basis-set dependent than conventional *ab initio* methods since the electron correlation is treated through the use of a functional rather than electron excitation.[36] In this dissertation, variations of Pople's split-valence double-zeta basis set, 6-31G,[43-46] are used for non-transition metals and non-halogens to compute molecular geometry and vibrational frequencies. This type of basis set is made from contracted Gaussian-type orbitals where core orbitals are comprised of six primitive Gaussian functions and valence orbitals are split into a set of three primitive Gaussian functions and a single primitive Gaussian function. Polarization functions are added to all atoms (p polarization for hydrogen and d polarization for heavy atoms) to give the 6-31G(d,p) basis, also called 6-31G**.[47] Diffuse functions can be added to a basis set to define the electron density far from the nucleus, which is important when computing Rydberg states, anions, or compounds with many lone pairs. However, the cases presented in this dissertation involve none of these situations so diffuse functions are not included in the basis sets, though it could be argued that diffuse functions on the halogens would be desirable but not essential.

After geometries and vibrational frequencies are computed with the Pople-type basis set, energetics are computed using a larger basis set to increase the accuracy of the computations. The TZ2P basis set was chosen for its proven accuracy with B3LYP computations.[48] This Dunning-type basis is of triple zeta quality with two polarization functions and is contracted as ($5s2p/3s2p$) for hydrogen, ($10s6p2d/5s3p2d$) for first-row atoms, and ($14s10p2d/7s5p2d$) for second-row atoms.

Transition metals and halogens typically have electronically dense cores that are not involved in bonding. Each electron present in the system greatly slows the computational time; thus, it is beneficial in some cases to model the core as a whole. Effective core potentials (ECPs)

replace core electrons with a pseudopotential while leaving valence electrons open to interact explicitly.[49] Not only do ECPs lower computational cost, they also recover relativistic effects not present in the computation, which are otherwise recovered only through the use of a relativistic Hamiltonian and multicomponent wave functions with extensive all-electron basis sets.[49]

ECPs are paired with matching basis sets. For geometry optimizations and frequency computations, the double zeta quality basis, denoted LANL2DZ,[50,51] is used to match the 6-31G(d,p) basis set used by non-transition metals and non-halogens. The use of these basis sets in conjunction with one another has proven beneficial for computing a wide variety of molecular properties including heats of formation and ionization potentials for transition metal containing compounds.[52] For energetic computations, a larger basis set is used on the transition metals and halogens to match the TZ2P basis used by the other atoms. For transition metals a triple zeta basis set with f polarization, denoted LANL2TZ(f), is used.[53] Halogens use the LANL08 basis set, which is also of triple zeta quality.[53]

A drawback to the B3LYP functional is its neglect of dispersion interactions, which are needed to describe medium and long range interactions.[54] In this dissertation, dispersion is especially important as π-complexation, an intermediate step in cross-coupling reactions with conjugated species, involves π-backbonding between the nickel d-orbitals and the aryl antibonding π-orbitals.[55] Fortunately, much work has been done by theorists to formulate a correction to account for dispersion, specifically by Grimme with–D and –D3 and Head-Gordon with–CHG.[56-58] Corrections are based on a pair-wise interaction which are not present in short-range interactions but bring about the correct asymptotic behavior at long-range interactions. In general, dispersion corrections have the form of r^{-6} with varying empirical components, including a damping function to determine the range of the correction.[56]

Table 1.1 presents the effects of different dispersion corrections on the energetics of the complexation reaction of benzene with Ni(dhpe), which is a truncated derivative of the common zerovalent cross-coupling catalyst Ni(dppe). Coupled-cluster single and double excitations (CCSD) with the TZ2P-LANL2TZ(f)-LANL08d basis set, described above, acts as the high-level standard from which to compare results from other methods. CCSD gives a binding energy of –30.81 kcal mol^{-1}. MP2 overestimates the binding by 14.63 kcal mol^{-1}, while B3LYP underestimates the binding by 7.49 kcal mol^{-1}. The addition of the –D correction brings the B3LYP reaction energy to within 1 kcal mol^{-1} of the CCSD result, with a slight underestimation of binding energetics. The –D3 correction also displays similar binding energy, 1.23 kcal mol^{-1} lower than the CCSD value. The –CHG correction does not do as well, giving a reaction energy 3.75 kcal mol^{-1} lower than the CCSD result. Thus, the B3LYP functional with the use of either the –D or –D3 correction is used in this dissertation for systems involving the complexation of an aryl species to a zerovalent nickel complex.
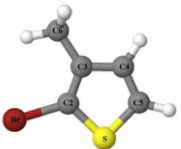
Table 1.1. Energetic Comparison of Computational Methods with the TZ2P-LANL2TZ(f)-LANL08d Basis Set for the Complexation of Benzene with Ni(dhpe)

	Single Point Energies (hartree)			E_{rxn} (hartree)	E_{rxn} (kcal mol^{-1})	δCCSD (kcal mol^{-1})
Method	Ni(dhpe)benzene	Ni(dhpe)	Benzene			
CCSD	–1162.3495	–930.8722	–231.4282	–0.0491	–30.81	—
MP2	–1163.0369	–931.4903	–231.4742	–0.0724	–45.44	–14.63
B3LYP	–1165.3294	–933.0459	–232.2464	–0.0372	–23.32	7.49
B3LYP–D	–1165.3626	–933.0613	–232.2538	–0.0475	–29.82	0.99
B3LYP–D3	–1165.3557	–933.0571	–232.2515	–0.0471	–29.58	1.23
B3LYP–CHG	–1165.3470	–933.0534	–232.2506	–0.0431	–27.06	3.75

As functionals are developed with a specific test set in mind, new systems must be benchmarked before results can be trusted.[59] With this in mind, the effect of the –D correction on geometry optimization was tested.

The geometry of 2-bromo-3-methylthiopehene is consistent within 0.01 Å and 0.1° when optimized with the B3LYP functional alone or with the added –D correction, as shown in Table 1.2. Minimal change in geometry is expected when a dispersion correction is added to the substrate as there are no long-range interactions.

Table 1.2. Molecular geometry of 2-bromo-3-methylthiophene computed at the B3LYP/6-31G(dp)-LANL2DZ and B3LYP-D/6-31G(dp)-LANL2DZ level of theory

	B3LYP	B3LYP-D		B3LYP	B3LYP-D		B3LYP	B3LYP-D
Bond	Bond Length (Å)		Angle	Bond Angle (°)		Out of Plane Atom	Out of Plane Angle (°)	
C2-C3	1.37	1.37	C2-S-C5	90.4	90.4	S oop	0.1	0.1
C3-C4	1.44	1.44	S-C2-C3	113.8	113.8	Br oop	0.0	0.0
C4-C5	1.36	1.36	C2-C3-C4	109.9	109.9	C6 oop	0.0	0.0
C2-S	1.74	1.74	C3-C4-C5	114.2	114.2			
C5-S	1.74	1.74	C4-C5-S	111.6	111.6			
C6-C3	1.50	1.50	C6-C3-C2	126.6	126.6			
Br-C2	1.94	1.94	Br-C2-S	119.1	119.1			

The complexation of Ni(dhpe) with 2-bromo-3-methylthiopehene presents a case where dispersion becomes important. When Ni(dhpe) is π-complexed at the C4=C5 position, bond lengths do not differ by more than 0.01 Å, as listed in Table 1.3. The largest deviation in bond angle is at the C4-C5-S bond with a decrease of 1.2° when the –D correction is included. Out of plane angles do not differ by more than 0.6°. In the optimization of such π-complexed minima, the amount of deviation between the B3LYP computed geometry and the B3LYP-D geometry is negligible.

Table 1.3. Molecular geometry of Ni(dhpe) complexed to 2-bromo-3-methylthiophene at the C4 and C5 position computed at the B3LYP/6-31G(dp)-LANL2DZ and B3LYP-D/6-31G(dp)-LANL2DZ level of theory

	B3LYP	B3LYP-D		B3LYP	B3LYP-D		B3LYP	B3LYP-D
Bond	Bond Length (Å)		Angle	Bond Angle (°)		Out of Plane Atom	Out of Plane Angle (°)	
Ni-C5	2.00	1.99	P1-Ni-P2	90.1	90.3	S oop	0.4	0.3
Ni-C4	2.02	2.03	C4-Ni-C5	41.7	41.5	C6 oop	0.4	0.2
Ni-P1	2.22	2.21	C2-S-C5	91.1	90.1	Br oop	4.4	3.8
Ni-P2	2.22	2.22	S-C2-C3	115.0	115.5			
C2-C3	1.36	1.36	C2-C3-C4	111.0	111.0			
C3-C4	1.46	1.46	C3-C4-C5	113.9	113.2			
C4-C5	1.43	1.43	C4-C5-S	109.0	110.2			
C2-S	1.75	1.76	C6-C3-C2	126.8	126.9			
C5-S	1.80	1.79	Br-C2-S	118.0	118.0			
C6-C3	1.50	1.50						
Br-C2	1.94	1.95						
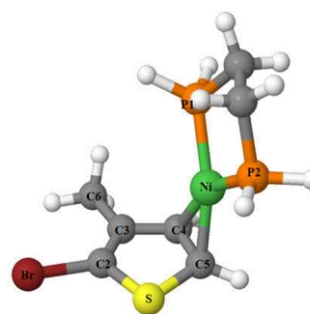
The deviation is also minor in a transition state computation, as shown in Table 1.4. Bond lengths do not differ by more than 0.05 Å, bond angles do not differ by more than 1.3°, and out of plane angles do not differ by more than 0.8°. Thus, geometries computed without a dispersion correction are as accurate as those computed with the correction. In this dissertation, molecular geometries and vibrational frequencies are computed without an added dispersion correction.

Dispersion plays a large role in the energetics of aryl bound transition metal complexes, especially when bond distances between the metal and the aryl substrate are short,[60] and polarization of the π-orbitals in the aromatic substrate produce strong long-range forces.[61] As discussed in Chapter 6, dispersion lowers the binding energy of such complexes by around 10 kcal mol^{-1} and must be included in energetic computations for accurate modeling.

Table 1.4. Molecular geometry of Ni(dhpe) complexed to 2-bromo-3-methylthiophene at the transition state for ring-walking computed at the B3LYP/6-31G(dp)-LANL2DZ and B3LYP-D/6-31G(dp)-LANL2DZ level of theory

Bond	B3LYP	B3LYP-D	Angle	B3LYP	B3LYP-D	Out of Plane Atom	B3LYP	B3LYP-D
	Bond Length (Å)			Bond Angle (°)			Out of Plane Angle (°)	
Ni-C5	2.42	2.41	P1-Ni-P2	91.8	91.5	S oop	11.6	12.0
Ni-C4	2.11	2.11	C4-Ni-C5	39.7	39.9	C6 oop	6.3	7.3
Ni-C3	2.16	2.14	C2-S-C5	88.4	87.7	Br oop	5.6	6.4
Ni-C2	2.44	2.39	S-C2-C3	114.1	114.1			
Ni-P1	2.21	2.21	C2-C3-C4	109.2	109.0			
Ni-P2	2.18	2.19	C3-C4-C5	113.6	112.8			
C2-C3	1.40	1.40	C4-C5-S	111.4	112.7			
C3-C4	1.45	1.45	C6-C3-C2	126.0	126.0			
C4-C5	1.4	1.39	Br-C2-S	118.3	118.1			
C2-S	1.77	1.77						
C5-S	1.77	1.76						
C6-C3	1.50	1.50						
Br-C2	1.94	1.94						
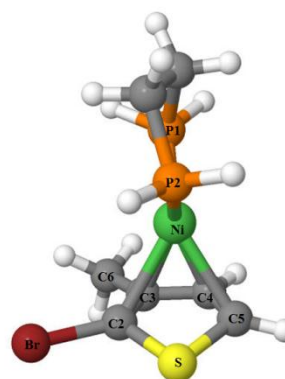
Objectives and Outline

The work presented in this dissertation focuses on two broad topics: (1) accurately quantifying ligand sterics in transition metal complexes and (2) mechanistic steps in transition metal catalyzed cross-coupling reaction. These topics work in unison to further the understanding of catalytic reactions by explaining, in detail, what mechanistic steps are present and important. The quantification of sterics can inform which steps in the reaction cycle are dependent on ancillary ligand sterics, which could aid in the design of more efficient catalysts, while mechanistic steps aid in determining not only catalyst but monomer scope as well.

Chapter 2 describes the first method of accurate ligand quantification, called the exact

ligand cone angle ($\theta°$). This method builds off one of the first methods of steric quantification presented by Tolman.[62] The original cone angle was developed specifically to describe the sterics of a symmetric, monodentate phosphine ligand bound to a nickel center. This leads to several coarse approximations, such as setting a ligand–metal bond length of 2.28 Å (determined from the average of nickel phosphine crystal structures), altering the structure of the ligand so that it is in the most compact conformation possible, and simply averaging apex angles in the case of an asymmetric ligand. We have improved upon this method through the use of a quadratic equation which calculates the exact cone angle using the specific geometry, found through crystallography or computational studies, and the atomic radii. Over 275 structures were analyzed, including complexes with non-phosphine ligands as well as bidentate ligands, to demonstrate the exact cone angle method accurately quantifies sterics of any ligand bound to any metal center.

Chapter 3 describes a second method to quantify sterics, called the exact solid angle ($\Omega°$). This method updates the solid cone angle (Θ), formulated by Immirzi *et al.* and later updated by White *et al.* and Brown *et al.*[63-65] The determination of the solid cone angle relies on calculating the ligand solid angle, which is described as the shadow cast by a ligand onto a surrounding sphere when the central atom acts as a hypothetical light source. To increase the accuracy of the method, the solid angle is calculated through the use of a line integral, rather than complicated addition and subtraction schemes as in previous reports. As with the exact cone angle, all that is needed to calculate the exact solid angle are the Cartesian coordinates of the complex and the accompanying atomic radii. This method is compatible with any ligand of any denticity bound to any sort of atomic center. Again, over 275 structures, with both monodentate and multidentate ligands, were analyzed.

Chapter 4 discusses an alternate reaction pathway present in the Kumada catalyst-transfer polycondensation (KCTP) reaction. The alternate pathway, called disproportionation, occurs when two initiated chains come in close contact and undergo homocoupling to results in polymer of increased dispersity and non-ideal end groups. Disproportionation can be controlled by suitable choice of ancillary ligand on the nickel complex. The tendency for an initiating complex, based on that ancillary ligand, to undergo disproportionation can be quantified by the disproportionation energy, which is simply the energy difference between the disproportionated products and the initiating reactants. Disproportionation energy was computed for complexes containing several common ancillary ligands and compared to reported experimental dispersities. The trend for a complex to disproportionate, based on increasing disproportionation energy, matches trends in increasing dispersity, showing the utility of computing disproportionation energies.

Chapter 5 discusses intramolecular oxidative addition in KCTP. In order for the polymerization to be controlled, the zerovalent nickel catalyst must stay in association with the growing polymer chain after reductive elimination.[23,24] Though evidence of a controlled polymerization has been shown for KCTP through idealized end groups, low dispersity, and small-molecule competition reactions,[21,66,67] the association has not been experimentally observed. Computational studies have shown that a π-complex is formed between the d-orbitals of the zerovalent nickel and the antibonding π-orbitals of the aryl substrate.[55,68] Using the kinetic isotope effect (KIE), we show that initial complexation of the nickel to the aryl substrate occurs before oxidative insertion. This initial π-complex leads to intramolecular oxidative addition, which is needed for a controlled polymerization. Experimental KIEs are found by quantitative ^{13}C NMR while theoretical KIEs for the nickel insertion step are computed through the use of

transition state theory to interpret the results. Energetic reaction profiles show that the movement of π-complexed nickel around the aryl ring, termed ring-walking, has reaction barriers typically lower than 10 kcal mol^{-1}. The barrier to nickel insertion is also low, under 15 kcal mol^{-1}, which makes intramolecular oxidative addition extremely facile.

Chapter 6 further expounds on the ring-walking process in Kumada coupling. The differences between ring-walking in 6-membered rings and 5-membered rings are exemplified by four substrates: *o*-bromotoluene, 2-bromopyridine, 2-bromo-3-methylthiophene, and 2-bromopyrrole. The nickel complex moves around the border of the ring in 6-membered species, while the nickel transverses the ring in 5-membered species. The stabilization brought about by dispersion is discussed as well as the effects of truncating the phenyl groups on the bidentate phosphine ancillary ligand.

Chapter 7 discusses intramolecular oxidative addition and the role of sterics in the Stille cross-coupling reaction. The catalyst in Stille coupling is a zerovalent palladium species with the monodentate phosphine ligand P(t-Bu)$_3$. The computed electrostatic potential of the monomer can determine its suitability for polymerization. If the electrostatic potential is highly negative the palladium complex will stay in association with the aryl species in order to undergo intramolecular oxidative addition. If it is more positive, intramolecular oxidative addition does not occur. Following the computed energetics of a previous report by Ariafard *et al.*,[69] steric changes over the course of the Stille coupling reaction are computed through the use of the exact solid angle. An increase in overlap between separate ligands tracks the energetics of mechanistic steps that are influenced by sterics, showing that tracking the change in sterics over the course of a reaction has the potential to elucidate influences into the energetics of reaction.

References

(1) Heeger, A. J. *Chem. Soc. Rev.* **2010**, *39*, 2354-2371.

(2) McGeehon, D. *Polymer Solutions Newsblog* **2012**,
    http://www.polymersolutions.com/blog/demand-growsfor-conductive-polymers/.

(3) Chen, C.-C.; Dou, L.; Zhu, R.; Chung, C.-H.; Song, T.-B.; Zheng, Y. B.; Hawks, S.; Li, G.;
    Weiss, P. S.; Yang, Y. *ACS Nano* **2012**, *6*, 7185-7190.

(4) Hagedon, M.; Yang, S.; Russell, A.; Heikenfeld, J. *Nat. Commun.* **2012**, *3*, 1173.

(5) Liang, J.; Li, L.; Niu, X.; Yu, Z.; Pei, Q. *Nat. Photon.* **2013**, *7*, 817-824.

(6) Roncali, J. *Chem. Rev.* **1992**, *92*, 711-738.

(7) Schoeler, U.; Tews, K. H.; Kuhn, H. *J. Chem. Phys.* **1974**, *61*, 5009-5016.

(8) Youngkyoo, K.; Cook, S.; Tuladhar, S. M.; Choulis, S. A.; Nelson, J.; Durrant, J. R.; Bradley,
    D. D. C.; Giles, M.; McCulloch, I.; Chang-Sik, H.; Ree, M. *Nature Mater.* **2006**, *5*, 197-203.

(9) Li, Y.; Zou, Y. *Adv. Mater.* **2008**, *20*, 2952-2958.

(10) Ohkita, H.; Cook, S.; Astuti, Y.; Duffy, W.; Tierney, S.; Zhang, W.; Heeney, M.;
    McCulloch, I.; Nelson, J.; Bradley, D. D. C.; Durrant, J. R. *J. Am. Chem. Soc.* **2008**, *130*,
    3030-3042.

(11) Yamamoto, T. *NPG Asia Materials* **2010**, *2*, 54-60.

(12) Beryozkina, T.; Senkovskyy, V.; Kaul, E.; Kiriy, A. *Macromolecules* **2008**, *41*, 7817-7823.

(13) Bao, Z.; Chan, W. K.; Yu, L. *J. Am. Chem. Soc.* **1995**, *117*, 12426-12435.

(14) Wang, J.; Lu, C.; Mizobe, T.; Ueda, M.; Chen, W.-C.; Higashihara, T. *Macromolecules*
    2013, *46*, 1783-1793.

(15) Wang, J.; Ueda, M.; Higashihara, T. *ACS Macro Lett.* **2013**, *2*, 506-510.

(16) Thompson, B. C.; Fréchet, J. M. J. *Angew. Chem. Int. Ed.* **2008**, *47*, 58-77.

(17) Zhou, H.; Yang, L.; Stuart, A. C.; Price, S. C.; Liu, S.; You, W. *Angew. Chem. Int. Ed.* **2011**, *50*, 2995-2998.

(18) Slooff, L. H.; Veenstra, S. C.; Kroon, J. M.; Moet, D. J. D.; Sweelssen, J.; Koetse, M. M. *Appl. Phys. Lett.* **2007**, *90*, 143506.

(19) Zhuang, W.; Lundin, A.; Andersson, M. R. *J. Mater. Chem. A* **2014**.

(20) Waltman, R. J.; Bargon, J.; Diaz, A. F. *J. Phys. Chem.* **1983**, *87*, 1459-1463.

(21) Bryan, Z. J.; McNeil, A. J. *Macromolecules* **2013**.

(22) McCullough, R. D. *Adv. Mater.* **1998**, *10*, 93-116.

(23) Miyakoshi, R.; Yokoyama, A.; Yokozawa, T. *J. Am. Chem. Soc.* **2005**, *127*, 17542-17547.

(24) Iovu, M. C.; Sheina, E. E.; Gil, R. R.; McCullough, R. D. *Macromolecules* **2005**, *38*, 8649-8656.

(25) Bilbrey, J. A.; Kazez, A. H.; Locklin, J.; Allen, W. D. *J. Comp. Chem.* **2013**, *34*, 1189–1197.

(26) Bilbrey, J. A.; Kazez, A. H.; Locklin, J.; Allen, W. D. *J. Chem. Theory Comput.* **2013**, *9*, 5734–5744.

(27) Hehre, W. J.; Radom, L.; Schleyer, P. v. R.; Pople, J. A. *Ab Initio Molecular Obrital Theory*; John Wiley & Sons: New York, 1986.

(28) Lee, C.; Yang, W.; Parr, R. G. *Phys. Rev. B* **1988**, *37*, 785-789.

(29) Becke, A. D. *J. Chem. Phys.* **1993**, *98*, 5648-5652.

(30) Sousa, S. F.; Fernandes, P. A.; Ramos, M. J. *J. Phys. Chem. A* **2007**, *111*, 10439-10452.

(31) Geerlings, P.; Proft, F. D.; Langenaeker, W. *Density Functional Theory : A Bridge between Chemistry and Physics*; VUB Press: Brussels, Belgium, 1999.

(32) Hohenberg, P.; Kohn, W. *Phys. Rev.* **1964**, *136*, B864-B871.

(33) Kohn, W.; Sham, L. J. *Phys. Rev.* **1965**, *140*, A1133-A1138.

(34) Becke, A. D. *Phys. Rev. A* **1988**, *38*, 3098-3100.

(35) Jensen, F. *Introduction to Computational Chemistry*; 1st ed.; John Wiley & Sons: Chichester, England, 2004.

(36) Niu, S.; Hall, M. B. *Chem. Rev.* **2000**, *100*, 353-406.

(37) Pyykko, P. *Chem. Rev.* **1988**, *88*, 563-594.

(38) Siegbahn, P. E. M.; John Wiley & Sons: New York, 1996; Vol. XCIII.

(39) Niu, S.; Hall, M. B. *J. Phys. Chem. A* **1997**, *101*, 1360-1365.

(40) Niu, S.; Hall, M. B. *J. Am. Chem. Soc.* **1997**, *119*, 3077-3086.

(41) Siegbahn, P. E. M. In *Advances in Chemical Physics*; John Wiley & Sons, Inc.: 2007, p 333-387.

(42) Xu, Z.-F.; Xie, Y.; Feng, W.-L.; Schaefer, H. F. *J. Phys. Chem. A* **2003**, *107*, 2716-2729.

(43) Dill, J. D.; Pople, J. A. *J. Chem. Phys.* **1975**, *62*, 2921-2923.

(44) Francl, M. M.; Pietro, W. J.; Hehre, W. J.; Binkley, J. S.; Gordon, M. S.; DeFrees, D. J.; Pople, J. A. *J. Chem. Phys.* **1982**, *77*, 3654-3665.

(45) Hehre, W. J.; Ditchfield, R.; Pople, J. A. *J. Chem. Phys.* **1972**, *56*, 2257-2261.

(46) Rassolov, V. A.; Pople, J. A.; Ratner, M. A.; Windus, T. L. *J. Chem. Phys.* **1998**, *109*, 1223-1229.

(47) Hariharan, P. C.; Pople, J. A. *Theor. Chem. Acc.* **1973**, *28*, 213-222.

(48) Thomas, J. R.; DeLeeuw, B. J.; Vacek, G.; Crawford, T. D.; Yamaguchi, Y.; Schaefer, H. F. *J. Chem. Phys.* **1993**, *99*, 403-416.

(49) Russo, T. V.; Martin, R. L.; Hay, P. J. *J. Phys. Chem.* **1995**, *99*, 17085-17087.

(50) Hay, P. J.; Wadt, W. R. *J. Chem. Phys.* **1985**, *82*, 299-310.

(51) Hay, P. J.; Wadt, W. R. *J. Chem. Phys.* **1985**, *82*, 270-283.

(52) Yang, Y.; Weaver, M. N.; Merz, K. M. *J. Phys. Chem. A* **2009**, *113*, 9843-9851.

(53) Roy, L. E.; Hay, P. J.; Martin, R. L. *J. Chem. Theory Comput.* **2008**, *4*, 1029-1031.

(54) Parsegian, V. A. *Van der Waals Forces: A Handbook for Biologists, Chemists, Engineers, and Physicists*; Cambridge University Press: Cambridge, U.K., 2006.

(55) Massera, C.; Frenking, G. *Organometallics* **2003**, *22*, 2758-2765.

(56) Grimme, S. *Wiley Interdiscip. Rev. Comput. Mol. Sci.* **2011**, *1*, 211-228.

(57) Grimme, S. *J. Comp. Chem.* **2006**, *27*, 1787-1799.

(58) Chai, J.-D.; Head-Gordon, M. *Phys. Chem. Chem. Phys.* **2008**, *10*, 6615-6620.

(59) Granatier, J.; Lazar, P.; Otyepka, M.; Hobza, P. *J. Chem. Theory Comput.* **2011**, *7*, 3743-3755.

(60) Siegbahn, P. E. M.; Blomberg, M. R. A.; Chen, S.-L. *J. Chem. Theory Comput.* **2010**, *6*, 2040-2044.

(61) Margenau, H.; Kestner, N. R. *Theory of Intermolecular Forces*; Pergamon Press: Oxford, New York, 1969.

(62) Tolman, C. A. *Chem. Rev.* **1977**, *77*, 313-348.

(63) Immirzi, A.; Musco, A. *Inorg. Chim. Acta* **1977**, *25*, L41-L42.

(64) Brown, T. L.; Lee, K. J. *Coord. Chem. Rev.* **1993**, *128*, 89-116.

(65) White, D.; Taverner, B. C.; Leach, P. G. L.; Coville, N. J. *J. Comp. Chem.* **1993**, *14*, 1042-1049.

(66) Kiriy, A.; Senkovskyy, V.; Sommer, M. *Macromol. Rapid Commun.* **2011**, *32*, 1503-1517.

(67) Bryan, Z. J.; McNeil, A. J. *Chem. Sci.* **2013**, *4*, 1620-1624.

(68) Yoshikai, N.; Matsuda, H.; Nakamura, E. *J. Am. Chem. Soc.* **2008**, *130*, 15258-15259.

(69) Ariafard, A.; Yates, B. F. *J. Am. Chem. Soc.* **2009**, *131*, 13981-13991.

CHAPTER 2

EXACT LIGAND CONE ANGLES
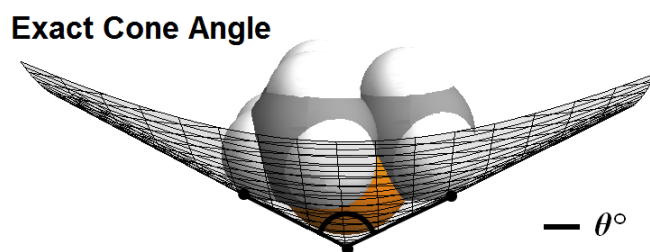
Exact Cone Angle

Abstract

Many properties of transition metal complexes depend on the steric bulk of bound ligands, usually quantified by the Tolman (θ) and solid (Θ) cone angles, which have proven utility but suffer from various limitations and coarse approximations. Here we present an improved, mathematically rigorous method to determine an exact cone angle ($\theta°$) by solving for the most acute right circular cone that contains the entire ligand. The procedure is applicable to any ligand, planar or nonplanar, mono- or polydentate, bound to any metal center in any environment, and it is ideal for analyzing structures from quantum chemical computations as well as X-ray crystallography experiments. Exact cone angles were evaluated for a wide array of phosphine and amine ligands bound to palladium, nickel or platinum by optimizing structures using B3LYP/6-31G* density functional theory with effective core potentials for the transition metals. The mean absolute deviations of the standard θ and Θ parameters from the exact cone angles were 15°– 25°, mostly caused by distortions from the assumed idealized structures.

Introduction

The steric bulk of a ligand plays a major role in controlling the reactivity of a transition metal complex by influencing ligand dissociation rates, insertion barriers, cis-trans isomerization, and trajectories of incoming ligands.[1-7] Several methods have been developed to quantify the steric bulk of a ligand, the Tolman cone angle (θ) being standard.[1,8] The θ parameter is defined by the apex angle of a cone originating at the metal center with edges lying on the van der Waal spheres of the outermost atoms (Fig. 2.1). The Tolman method was originally developed for monodentate phosphine ligands bound to a nickel center and cone angles were measured using a physical CPK model and specialized ruler.[1] The M–P bond distance was empirically set to 2.28 Å (averaged from crystal structures of nickel complexes) and a tetrahedral geometry was assumed about the phosphorus atom. The ligand was folded up to make the smallest possible cone, and the cone axis was fixed along the M–P bond. For asymmetric phosphine ligands, the Tolman scheme averaged the apex angles for the three phosphorus substituents: $\theta = \frac{1}{3}(\theta_1 + \theta_2 + \theta_3)$. The cone angle for a bidentate phosphine ligand was derived from the outer non-bridging phosphine substituents and the bisector of the P–M–P angle (Fig. 2.1).[9] Additional work on steric parameters of amine-based ligands measured cone angles in the same manner but with the M–N bond length set to 2.20 Å;[10] the cone angle was found to be highly dependent on the M–N distance, which is lengthened in bulky ligands. More recently, the Shaughnessy and Dixon groups[11-14] have used the Tolman averaging scheme to obtain cone angles for monodentate phosphine ligands in palladium complexes whose structures were optimized by density functional theory.

The Tolman cone angle suffers from several coarse approximations: restriction of the metal-ligand bond length to 2.28 Å, which is highly inaccurate for non-phosphine ligands and

various metal centers; the assumption of a tetrahedral geometry about the phosphorus atom; free folding of the ligand upwards to form the smallest possible cone; and mathematical imprecision in the treatment of asymmetric and polydentate ligands. Moreover, variations in steric bulk around the metal center, as well as crystal packing effects, can cause conformational changes yielding a range of cone angles for a single type of ligand.[15-17]
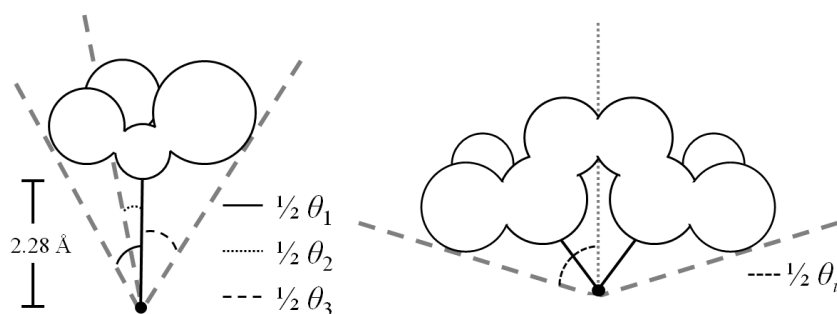
Figure 2.1. Tolman cone angle (θ) of an asymmetric, monodentate ligand (left) and a symmetric bidentate ligand (right).

Another established method for quantifying steric demand is the solid cone angle (Θ) derived from the area filled by the ligands on the surface of an encompassing sphere (S) centered at the metal atom.[8,18,19] The Θ parameter can be visualized by means of the collective shadow cast by the ligands onto sphere S from a light source at the metal atom (Fig. 2.2). The solid angle (Ω_i) for a single atom i, modeled as a sphere, can be calculated through analytic integration of the corresponding shadow (s_i) cast on S: $\Omega_i = 2\pi\left[1 - \cos\left(\frac{1}{2}\theta_i\right)\right]$, where θ_i is the apex angle of the shadow cone.[19] The solid angle for multiple atoms is obtained merely by summing over all the individual shadows if they are disjoint; however, there are severe analytic difficulties because the shadows commonly overlap. An approximate solution to this problem has been achieved by projecting the shadows residing on sphere S onto an underlying plane and computing the areas of

overlap among the resulting ellipses.[20] As the number of atoms casting a shadow on a single region increases, the task of eliminating overcounting of the solid angle contributions becomes increasingly difficult, and to our knowledge, a complete analytic solution to this problem does not appear in the literature. In any event, once an approximate value for the total solid angle Ω has been obtained, the Θ parameter is computed as the apex angle of an equivalent single cone that would yield Ω; in particular, $\Theta = 2b \cos^{-1}\left(1 - \Omega/2\pi\right)$, where $b = 1$ in the ideal case.
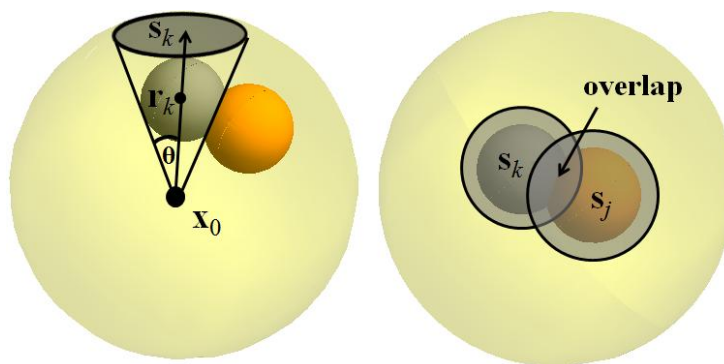
Figure 2.2. The shadow cast by a single ligand atom (left) and overlapping shadows cast by two ligand atoms (right) in the solid cone angle (Θ) method.

The concept of the solid cone angle was recently revised to improve the description of bidentate ligands by modifying the b factor in the above equation for Θ.[21] Simple correction terms were appended to the ideal $b = 1$ value to account for changes in the bite angle of the bidentate ligand and deviation of the metal-ligand bond distances from the 2.28 Å reference length. This scheme was applied to over 900 crystal structures of platinum complexes containing more than 280 different bidentate phosphorus ligands.

A significant disadvantage of the solid angle approach is the treatment of the ligand as frozen. Many monodentate ligands exist in dynamical environments with nearly free internal rotation over low barriers.[22-24] While the solid angle provides an accurate snapshot at a given

time, it does not account for free rotation about the metal-ligand bond. In this case, a circular cone provides a better measurement of dynamical steric demands.

Within the last decade, additional steric models have been developed to quantify steric effects of ligands. A starting point to deal with nonsymmetric ligands such as *N*-heterocyclic carbenes (NHCs) is the percent buried volume ($\%V_{bur}$) model,[25] based on the amount of space occupied by a ligand skeleton inside a coordination sphere of pre-defined radius centered on the metal atom. Values of $\%V_{bur}$ have been calculated for a large number of X-ray structures.[26] Although highly dependent on the radius chosen for the coordination sphere, $\%V_{bur}$ parameters correlate reasonably well with both ligand dissociation energies and Tolman cone angles.[25,26] New steric descriptors, termed He_8_steric and He_8_wedge, were recently introduced as measures of non-bonded *cis* interactions of ligands bound to a metal center in an octahedral complex.[27] In these approaches density functional theory is used to compute the interaction energy between a given ligand and a ring or wedge of eight helium atoms frozen at locations to mimic steric repulsions with adjacent ligands. The metal atom is omitted in the computation, and the positions of the non-donor atoms in the ligand are optimized. These He_8_steric and He_8_wedge methods highlight ligand similarities in bidentate and bulky ligands but have the drawback of being artificial, theoretical quantities.

A new mathematical procedure is presented here for taking a given structure of a complex and exactly determining the cone angle of any ligand therein, based on the idea of enveloping the ligand in the most acute possible cone in which all of its atoms are fully contained. The procedure is applicable to any type of ligand attached to any type of metal, and it can take full advantage of geometric structures computed from electronic structure theory or extracted from X-ray crystallography data. Exact cone angles for both computed and

crystallographic structures are readily calculated through analytic formulas, where the only input is the Cartesian coordinates of the system and the van der Waals radii of included atoms.

Mathematical Formulation

The exact cone angle ($\theta°$) of a ligand is defined here as the apex angle (2α) of the most acute right circular cone that originates at the metal center and contains all ligand atoms, each described by a sphere centered at $\mathbf{r}_k$ with van der Waals radius r_k (Fig. 2.3). The designation "exact" for $\theta°$ refers to the mathematical solution for a given molecular structure and chosen set of van der Waals radii; "exact" does not refer to the accuracy of the input structure itself. The locus of points $\mathbf{x}$ forming the surface of a right circular double-cone with apex at $\mathbf{x}_0$ and axis along unit vector $\mathbf{n}$ is given by

$$\frac{(\mathbf{x}-\mathbf{x}_0)\cdot\mathbf{n}}{|\mathbf{x}-\mathbf{x}_0|} = \pm\cos\alpha \ . \tag{1}$$
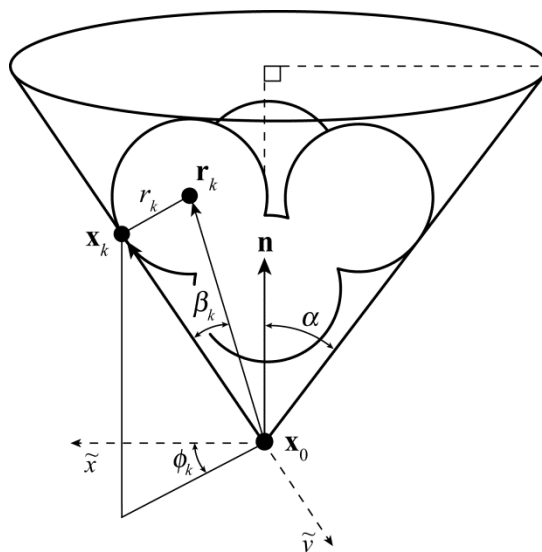
Figure 2.3. Parameters of a right circular cone containing all atoms in a ligand; the exact cone angle is $\theta° = 2\alpha$.

The parametric equation for the cone axis is $\mathbf{y}(t) = \mathbf{x}_0 + t\,\mathbf{n}$ for $t \in (-\infty, +\infty)$. The quadratic form of Eq. (1) is

$$\left[(\mathbf{x} - \mathbf{x}_0) \cdot \mathbf{n}\right]^2 - \cos^2\alpha\left[(\mathbf{x} - \mathbf{x}_0) \cdot (\mathbf{x} - \mathbf{x}_0)\right] = 0 \ . \tag{2}$$

The cone is required to contain all atoms in the ligand and be tangent to one, two, or three of those atoms depending on the spatial arrangement. The outer edge of each defining atom corresponds to a tangent point ($\mathbf{x}_k$), which must be co-planar with the atom center ($\mathbf{r}_k$), metal center ($\mathbf{x}_0$), and the cone axis $\mathbf{y}(t)$. For convenience, we employ a body-fixed coordinate system, denoted by tildes, with the origin at the apex and the cone axis $\mathbf{n}$ directed along the z axis. Accordingly, the body-fixed coordinates of the tangent points are

$$\tilde{\mathbf{x}}_k = R_k\left(\sin\alpha\cos\phi_k, \sin\alpha\sin\phi_k, \cos\alpha\right) , \tag{3}$$

where the distance to the metal center is

$$R_k = \sqrt{(\mathbf{r}_k - \mathbf{x}_0) \cdot (\mathbf{r}_k - \mathbf{x}_0) - r_k^2} \ . \tag{4}$$

The body-fixed position of the center of atom k is

$$\tilde{\mathbf{r}}_k = |\mathbf{r}_k - \mathbf{x}_0|\left[\sin(\alpha - \beta_k)\cos\phi_k, \sin(\alpha - \beta_k)\sin\phi_k, \cos(\alpha - \beta_k)\right] , \tag{5}$$

where the angle between $\mathbf{r}_k - \mathbf{x}_0$ and the cone edge (Fig. 2.3) is given by

$$\sin\beta_k = \frac{r_k}{|\mathbf{r}_k - \mathbf{x}_0|} \ . \tag{6}$$

The unit vector directed from the apex to atomic center k is

$$\mathbf{m}_k = \frac{\mathbf{r}_k - \mathbf{x}_0}{|\mathbf{r}_k - \mathbf{x}_0|} = \left[\sin(\alpha - \beta_k)\cos\phi_k, \sin(\alpha - \beta_k)\sin\phi_k, \cos(\alpha - \beta_k)\right] \ . \tag{7}$$

If the cone is determined only by a single atom k, then $\theta° = 2\alpha_k = 2\beta_k$, and the cone axis $\mathbf{n}$ is directed along $\mathbf{m}_k$. A simple example is a carbonyl ligand, wherein the oxygen is shielded from the metal center by the carbon van der Waals surface (Fig. 2.4).
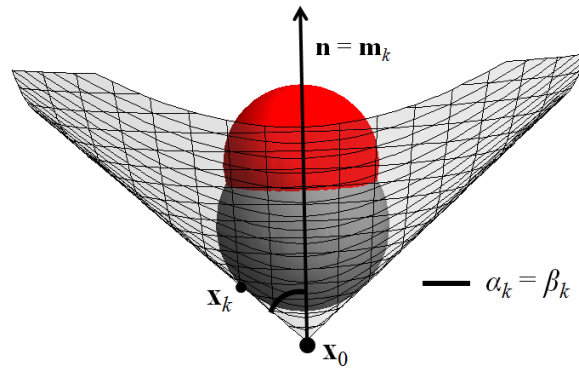
Figure 2.4. The cone of a carbonyl ligand (gray = carbon, red = oxygen) is dependent only on the carbon atom and thus $\alpha_k = \beta_k$. The metal center is located at $\mathbf{x}_0$.

If the cone is determined by two atoms i and j (Fig. 2.5), the cone angle α_{ij} must obey

$$\cos\beta_{ij} = \frac{\tilde{\mathbf{r}}_i \cdot \tilde{\mathbf{r}}_j}{|\tilde{\mathbf{r}}_i||\tilde{\mathbf{r}}_j|} = \sin\left(\alpha_{ij} - \beta_i\right)\sin\left(\alpha_{ij} - \beta_j\right)\cos\phi_{ij} + \cos\left(\alpha_{ij} - \beta_i\right)\cos\left(\alpha_{ij} - \beta_j\right) , \tag{8}$$

where β_{ij} is the angle between $\tilde{\mathbf{r}}_i$ and $\tilde{\mathbf{r}}_j$, and the azimuthal angle difference $\varphi_{ij} = \varphi_i - \varphi_j$ is a variable. Using standard trigonometric identities, Eq. (8) can be simplified to

$$2\cos\beta_{ij} = \left(1 + \cos\phi_{ij}\right)\cos\left(\beta_i - \beta_j\right) + \left(1 - \cos\phi_{ij}\right)\cos\left(2\alpha_{ij} - \beta_i - \beta_j\right) , \tag{9}$$

which gives the key working equation:

$$\cos\left(2\alpha_{ij} - \beta_i - \beta_j\right) = \frac{2\cos\beta_{ij} - \left(1 + \cos\phi_{ij}\right)\cos\left(\beta_i - \beta_j\right)}{1 - \cos\phi_{ij}} . \tag{10}$$

The minimum cone angle is found by differentiating Eq. (10) to obtain

$$\left(\frac{\partial \alpha_{ij}}{\partial \phi_{ij}}\right) = -\frac{\sin\left(\alpha_{ij} - \beta_i\right)\sin\left(\alpha_{ij} - \beta_j\right)\sin\phi_{ij}}{\left(1 - \cos\phi_{ij}\right)\sin\left(2\alpha_{ij} - \beta_i - \beta_j\right)} . \tag{11}$$

The derivative in Eq. (11) vanishes when $\varphi_{ij} = \pi$, and from Eq. (10) the minimum cone angle satisfies

$$\theta° = 2\alpha_{ij} = \beta_{ij} + \beta_i + \beta_j . \tag{12}$$
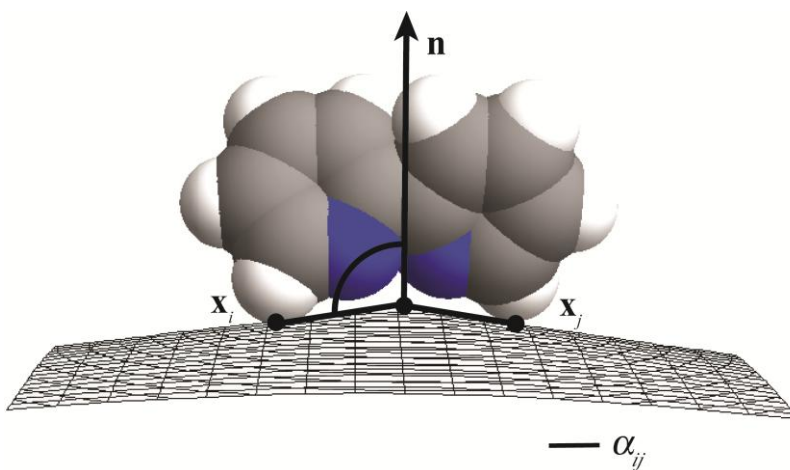
Figure 2.5. The apex angle of a 2,2′-bipyridine (bpy) ligand (gray = carbon, blue = nitrogen, white = hydrogen) determined by two atoms i and j.

Once α is determined from a set of ligand atoms L, the cone axis $\mathbf{n}$ can be derived from

$$\mathbf{m}_k \cdot \mathbf{n} = \cos\left(\alpha - \beta_k\right) , \quad k \in \text{L}. \tag{13}$$

Representing the cone axis in terms of two non-colinear unit vectors $\mathbf{m}_i$ and $\mathbf{m}_j$,

$$\mathbf{n} = a_{ij}\,\mathbf{m}_i + b_{ij}\,\mathbf{m}_j + c_{ij}\,\csc\beta_{ij}\left(\mathbf{m}_i \times \mathbf{m}_j\right) . \tag{14}$$

Application of Eq. (13) for $k = i$ and j gives the coefficients

$$a_{ij} = \frac{\cos\left(\alpha - \beta_i\right) - \cos\left(\alpha - \beta_j\right)\cos\beta_{ij}}{\sin^2\beta_{ij}} \tag{15}$$

and

$$b_{ij} = \frac{\cos(\alpha - \beta_j) - \cos(\alpha - \beta_i)\cos\beta_{ij}}{\sin^2\beta_{ij}} = a_{ji}, \tag{16}$$

whereas the normalization condition on **n** requires

$$c_{ij} = \pm\sqrt{1 - a_{ij}^2 - b_{ij}^2 - 2a_{ij}b_{ij}\cos\beta_{ij}} \ . \tag{17}$$

In the special case of Eq. (12), algebraic reduction with standard trigonometric formulas provides

$$\{a_{ij}, \ b_{ij}, \ c_{ij}\} = \left\{\csc\beta_{ij}\sin\left[\tfrac{1}{2}(\beta_{ij} + \beta_i - \beta_j)\right], \ \csc\beta_{ij}\sin\left[\tfrac{1}{2}(\beta_{ij} - \beta_i + \beta_j)\right], \ 0\right\}. \tag{18}$$
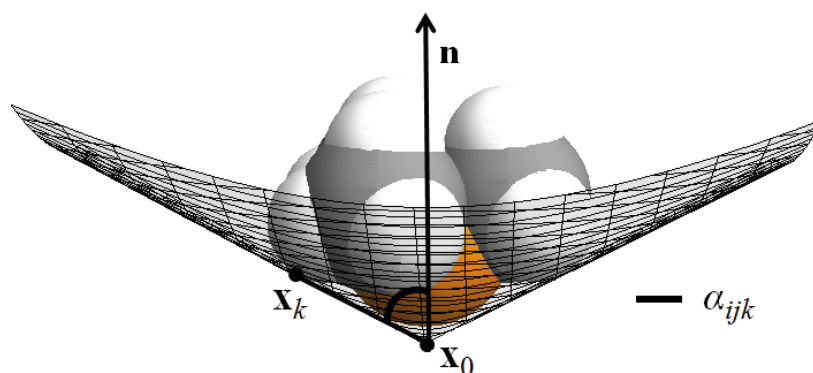
Figure 2.6. The apex angle of a trimethylphosphine ligand (gray = carbon, orange = phosphorus, white = hydrogen) bound to palladium atom centered at $\mathbf{x}_0$. The cone is dependent on three atoms in the ligand; only one tangent point ($\mathbf{x}_k$) is depicted.

If tangency to three atoms (i, j, k) is required to fix the ligand cone (Fig. 2.6), the analysis is significantly more involved. Let

$$\mathbf{M} = \begin{bmatrix} \mathbf{m}_i & \mathbf{m}_j & \mathbf{m}_k \end{bmatrix} \tag{19}$$

be the matrix whose columns contain the units vectors $\mathbf{m}_i$, $\mathbf{m}_j$, and $\mathbf{m}_k$. Equation (13) then provides three conditions that produce the system of equations

$$\mathbf{M}^{\mathrm{T}}\mathbf{n} = \mathbf{u}\cos\alpha_{ijk} + \mathbf{v}\sin\alpha_{ijk} \ , \tag{20}$$

in which

$$\mathbf{u} = \left(\cos\beta_i, \cos\beta_j, \cos\beta_k\right) \text{ and } \mathbf{v} = \left(\sin\beta_i, \sin\beta_j, \sin\beta_k\right) \ . \tag{21}$$

Inverting Eq. (20) provides $\mathbf{n} = \gamma_{ijk}^{-1}\mathbf{p}$, where

$$\mathbf{p} = \mathbf{N}\left(\mathbf{u}\cos\alpha_{ijk} + \mathbf{v}\sin\alpha_{ijk}\right), \tag{22}$$

$$\gamma_{ijk} = \mathbf{m}_i \cdot \left(\mathbf{m}_j \times \mathbf{m}_k\right) \ , \tag{23}$$

and matrix $\mathbf{N}$ satisfies

$$\mathbf{N} = \gamma_{ijk}\left(\mathbf{M}^{\mathrm{T}}\right)^{-1} = \left[\mathbf{m}_j \times \mathbf{m}_k \quad \mathbf{m}_k \times \mathbf{m}_i \quad \mathbf{m}_i \times \mathbf{m}_j\right] \ . \tag{24}$$

The normalization condition on $\mathbf{n}$, or equivalently $\mathbf{p} \cdot \mathbf{p} = \gamma_{ijk}^2$, gives the key equation for

the cone angle:

$$A\cos^2\alpha_{ijk} + B\sin^2\alpha_{ijk} + 2C\sin\alpha_{ijk}\cos\alpha_{ijk} = D \ , \tag{25}$$

whose constants are given by

$$\left(A,\ B,\ C\right) = \left(\mathbf{u}^{\mathrm{T}}\mathbf{P}\mathbf{u},\ \mathbf{v}^{\mathrm{T}}\mathbf{P}\mathbf{v},\ \mathbf{u}^{\mathrm{T}}\mathbf{P}\mathbf{v}\right) \tag{26}$$

and

$$D = \gamma_{ijk}^2 = 1 - \cos^2\beta_{ij} - \cos^2\beta_{jk} - \cos^2\beta_{ik} + 2\cos\beta_{ik}\cos\beta_{jk}\cos\beta_{ij} \ , \tag{27}$$

with

$$\mathbf{P} = \mathbf{N}^{\mathrm{T}}\mathbf{N} = \begin{pmatrix} \sin^2\beta_{jk} & \cos\beta_{jk}\cos\beta_{ik} - \cos\beta_{ij} & \cos\beta_{ij}\cos\beta_{jk} - \cos\beta_{ik} \\ \cos\beta_{jk}\cos\beta_{ik} - \cos\beta_{ij} & \sin^2\beta_{ik} & \cos\beta_{ik}\cos\beta_{ij} - \cos\beta_{jk} \\ \cos\beta_{ij}\cos\beta_{jk} - \cos\beta_{ik} & \cos\beta_{ik}\cos\beta_{ij} - \cos\beta_{jk} & \sin^2\beta_{ij} \end{pmatrix}. \tag{28}$$

Equation (25) can be cast in the form

$$w^2 \left[(A-B)^2 + 4C^2 \right] + 2(A-B)(A+B-2D)w + (A+B-2D)^2 - 4C^2 = 0 \ , \qquad (29)$$

involving the variable $w = \cos 2\alpha_{ijk}$. Solving this quadratic equation for w provides four candidate analytic solutions for the exact cone angle $\theta^\circ = 2\alpha_{ijk}$; specifically,

$$\theta^\circ = \left\{ \cos^{-1} w_<, \ 2\pi - \cos^{-1} w_<, \ \cos^{-1} w_>, \ 2\pi - \cos^{-1} w_> \right\} \ , \qquad (30)$$

where $w_<$ and $w_>$ denote the smaller and larger roots of Eq. (29), respectively.

Among the four possibilities for θ°, only two distinct, physical solutions exist for the cone angle, as seen by testing for extraneous roots with Eq. (25). Of the two proper solutions, the larger ($\theta_>^\circ$) and smaller ($\theta_<^\circ$) ones generally place the tangent spheres inside and outside of an acute cone, respectively. Therefore, $\theta_>^\circ$ is usually the desired solution; however, the ligand cone angle could originate from any of the four possibilities in Eq. (30). After the cone angle is selected, Eqs. (14) – (17) always provide the cone axis $\mathbf{n}$. The sign of c_{ij} in Eq. (17) should be chosen according to

$$\operatorname{sgn}(c_{ij}) = \operatorname{sgn}(\gamma_{ijk}) \operatorname{sgn}\left[\mathbf{p} \cdot (\mathbf{m}_i \times \mathbf{m}_j) \right] \ , \qquad (31)$$

as derived from Eqs. (14) and (22). A special case arises if atoms i, j, and k all happen to be co-planar with the apex atom ($\gamma_{ijk} = 0$). Equation (29) is still valid, but $\gamma_{ijk} = 0$ dictates that $C^2 = AB$ and $D = 0$. These restrictions cause a degeneracy in the w roots, whence both signs for c_{ij} in Eq. (17) correspond to physical solutions.

The condition for atom m to lie completely inside a cone constructed from other atoms is

$$\alpha \geq \beta_m + \cos^{-1}(\mathbf{m}_m \cdot \mathbf{n}) \ , \qquad (32)$$

where $\mathbf{m}_m$ is the unit vector directed from the apex of the cone to atom m. If a cone angle greater

than 180° is dictated by the ligand, all of the above equations and root selection criteria are valid.

The overall procedure for determining $\theta°$ of a ligand involves the compilation and winnowing of a list of candidate cones, as follows:

(1) Iterate over all single atoms of the ligand, setting $\alpha_k = \beta_k$ and taking $\mathbf{n} = \mathbf{m}_k$ from Eq. (7). Select $\alpha_{max1} = \text{Max}[\{\alpha_k\}]$ among all k. If all ligand atoms lie completely inside the α_{max1} cone according to Eq. (32), then take $\theta° = 2\alpha_{max1}$ and exit.

(2) Exclude from further consideration all ligand atoms that lie in the shadow cone of another ligand atom, as revealed by Eq. (32).

(3) Iterate over all pairs of ligand atoms, evaluating α_{ij} from Eq. (12) and $\mathbf{n}$ from Eqs. (14) and (18). Find $\alpha_{max2} = \text{Max}[\{\alpha_{ij}\}]$ among all ij. If all ligand atoms lie completely inside the α_{max2} cone according to Eq. (32), then take $\theta° = 2\alpha_{max2}$ and exit.

(4) Iterate over all unique combinations of three ligand atoms, computing α_{ijk} from Eq. (29). Eliminate all candidates for which α_{ijk} is either less than α_{max2} from step (3) or greater than $\text{max}[\beta_k + \gamma_{k,c}]$ among all k, where $\gamma_{k,c}$ is the angle between $\mathbf{m}_k$ and the vector from the apex metal atom to the centroid of the ligand.

(5) Exhaustively test with Eq. (32) to identify all remaining three-atom cones with angles α_{lmn} that completely contain all ligand atoms. Select $\theta° = 2\text{Min}[\alpha_{lmn}]$ among all lmn as the cone angle if previous solutions were not found in steps (1) and (3).

Computational Methods

The optimized geometries of all molecules were computed using the B3LYP[28,29] density functional with a radial, angular (75, 302) grid by means of the QChem3.2 and QChem4.0 packages.[30] All electronic structure computations employed a Pople-type basis set, 6-31G*, for

first-row[31] and second-row[32] atoms, and a basis set with an effective core potential, LANL2DZ, for transition metals.[33] For molecules with multiple conformers, relative energies were computed with zero-point vibrational energy (ZPVE) corrections using the same methods described above. A *Mathematica*[34] package FindConeAngle was written to compute the $\theta°$ cone angles and visualize the solutions, using minimal computational time once an optimized geometry is obtained. This package is freely available at http://www.ccqc.uga.edu/references/software.php. The adopted van der Waals radii were r = (1.80, 1.20, 1.70, 1.55, 1.52, 1.47, 1.80, 1.75) Å for (P, H, C, N, O, F, S, Cl), in order.[35]

Computational Results

The exact cone angle ($\theta°$) method was applied to over 150 complexes optimized with B3LYP/6-31G* density functional theory, utilizing effective core potentials on the metal atoms. The popular B3LYP/6-31G* level of theory is effective for performing a broad survey of cone angle trends and is expected to give reasonable structures,[36,37] with average bond distances that deviate less than 2.5% from known crystal structures for transition-metal compounds.[38] Naturally, the cone angles depend on the accuracy of the computed geometric structures, and future studies will be required to precisely refine $\theta°$ values for reference compounds. In a comparison of $\theta°$ results from five alternative density functionals (B3LYP-D3, M06, B97, M05-2X, PBE) for 10 different palladium-bound ligands, the mean difference from the B3LYP value is less than 1°, and the corresponding standard deviation is less than 2°. This high level of agreement bolsters confidence in the comprehensive B3LYP data reported here.

Table 2.1 shows comparative cone angle results for a wide array of monodentate phosphine ligands coordinated to palladium, nickel, or platinum with no other ligands present.

Metal-ligand bond lengths are known to vary with coordination geometries of the metal as well as ligand-ligand interactions within the complex.[22,39,40] The B3LYP Pd–P bond lengths in the palladium complexes range from 2.20 to 2.28 Å, the majority falling between 2.22 and 2.24 Å. Thus, the computed Pd–P distances are somewhat shorter than Tolman's assumed value of 2.28 Å. As a ligand moves closer to the metal center, the cone angle should increase in the absence of secondary geometric distortions.

The computed minimum exact cone angles ($\theta°$) for Pd complexes in Table 2.1 have a mean absolute deviation (MAD) of 15.2° and 18.3° relative to the Tolman and solid cone angles, respectively. Only two ligands [P(o-MePh)$_3$, PBz$_3$] out of 41 have min $\theta° < \theta$, while only eight ligands (20%) [PMe$_3$, PEt$_3$, P(n-Bu)$_3$, PMe$_2$Et, PMeEt$_2$, PEt$_2$(t-Bu), PPh(n-Bu)$_2$, PBz$_3$] have min $\theta° < \Theta$. The MAD of $\theta°$ versus (θ, Θ) is (18.6°, 20.4°) for Pt complexes and (21.8°, 23.4°) for Ni analogs. The MAD statistics indicate that the Tolman and solid cone angles tend to underestimate the steric demands of the ligands in these complexes.

For ligands with multiple conformations, a range of $\theta°$ cone angles exists. The minimum and maximum $\theta°$ values among the various conformers are specified in the "min" and "max" columns in Table 2.1. In numerous cases, the values are vastly different; for example, the cone angle of Pd(PEt)$_3$ is 33° larger in the max conformation (Fig. 2.7). Cone angles of both min and max conformations are useful when evaluating the steric demands of a ligand. Indeed, ligands such as alkyl phosphites have been termed "steric chameleons" because they use conformational flexibility to adapt to the chemical environment.[41] Additional substituents, if bulky, could force a ligand into the minimum conformation to relieve steric crowding;[42] hence, the minimum $\theta°$ is more applicable in crowded environments. It is known that ligands in crowded environments display different steric characteristics than uncrowded ligands.[43]

Table 2.1. Exact Cone Angles ($\theta°$) vs. Tolman[1] (θ) and Solid[8] (Θ) Cone Angles in degrees for an Array of Pd, Ni, and Pt Complexes with Monodentate Phosphine Ligands

Ligand	θ	Θ	$\theta°$(Pd)		$\theta°$(Ni)		$\theta°$(Pt)	
			Min	Max	Min	Max	Min	Max
PMe$_3$	118	124	120.4	–	125.8	–	124.7	–
PEt$_3$	132	143	136.0	168.7	142.6	175.8	140.4	171.1
P(n-Bu)$_3$	132	148	136.2	169.3	142.8	176.1	140.7	171.1
P(i-Bu)$_3$	143	173	–	213.8	–	223.7	–	215.6
P(i-Pr)$_3$	160	163	169.0	177.1	176.6	184.7	173.2	181.4
P(t-Bu)$_3$	182	182	187.6	–	196.3	–	191.8	–
PMe$_2$Et	123	133	123.7	142.3	129.3	148.7	127.8	146.8
PMe$_2$(i-Pr)	132	140	147.6	–	154.0	–	150.9	–
PMe$_2$(t-Bu)	139	144	146.0	–	152.6	–	150.2	–
PMeEt$_2$	127	138	129.5	153.3	135.5	160.1	133.8	156.6
PEt$_2$(i-Pr)	141	150	150.9	171.5	157.8	178.7	155.2	175.4
PEt$_2$(t-Bu)	149	156	152.7	175.7	160.1	180.7	157.1	176.8
PMe(i-Pr)$_2$	146	151	159.2	160.9	166.3	167.9	157.4	165.0
PEt(i-Pr)$_2$	151	156	169.8	174.5	177.6	182.4	173.7	179.4
P(i-Pr)$_2$(t-Bu)	167	170	177.2	186.6	185.3	195.3	182.4	182.9
PMe(t-Bu)$_2$	161	163	174.4	–	182.2	–	179.0	–
PEt(t-Bu)$_2$	165	161	175.4	177.2	183.8	184.6	179.8	181.5
P(i-Pr)(t-Bu)$_2$	175	178	181.8	182.5	190.2	190.6	185.6	186.1
PPh$_3$	145	129	170.0	–	177.6	–	174.6	–
P(p-ClPh)$_3$	145	129	170.2	–	177.7	–	174.6	–
P(m-MePh)$_3$	145	140	169.7	178.7	177.2	183.2	172.5	180.9
P(m-ClPh)$_3$	145	136	169.6	172.1	177.3	177.8	174.1	174.5
P(p-MePh)$_3$	145	135	170.7	–	178.2	–	174.6	–
P(p-OMePh)$_3$	145	139	170.3	171.5	177.9	178.9	173.7	175.4
P(p-FPh)$_3$	145	129	170.8	–	178.0	–	174.8	–
P(m-(t-Bu)Ph)$_3$	145	159	168.4	207.3	175.9	212.6	173.3	209.8
P(o-MePh)$_3$	194	142	175.6	208.2	184.4	218.7	179.9	210.7
PPh$_2$H	128	112	146.3	–	156.4	–	149.3	–
PPh$_2$Me	136	124	151.4	–	160.3	–	155.5	–
PPh$_2$Et	140	140	149.9	169.3	155.9	177.8	153.0	172.5
PPh$_2$(n-Bu)	140	140	149.7	173.2	156.5	180.2	153.7	172.8
PPh$_2$(i-Bu)	144	148	150.3	192.9	156.4	201.5	154.2	196.3
PPh$_2$(i-Pr)	150	139	164.1	173.5	170.5	180.8	168.0	178.2
PPh$_2$Bz	152	139	163.2	186.4	169.4	194.7	167.9	187.5
PPh$_2$(t-Bu)	157	149	166.5	–	172.9	–	170.2	–
PPh$_2$Cl	138	117	156.3	–	164.1	–	156.1	–
PPhMe$_2$	122	126	148.5	–	155.5	–	152.9	–
PPhEt$_2$	136	137	153.1	172.8	159.6	180.1	157.1	176.8
PPh(n-Bu)$_2$	136	154	136.2	170.0	142.8	176.2	141.9	173.1
PPh(t-Bu)$_2$	170	168	186.7	–	195.3	–	190.8	–
PBz$_3$	165	163	140.8	202.9	148.0	209.3	145.8	199.3

$$\theta° = 136° \qquad\qquad \theta° = 169°$$
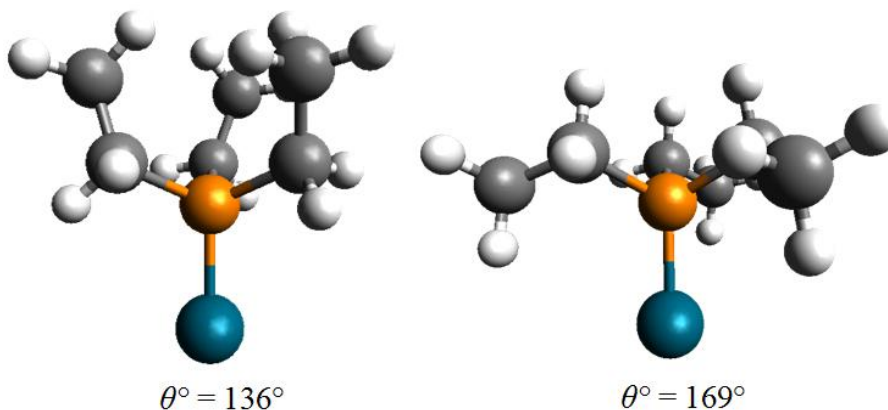
Figure 2.7. Structures and exact cone angles ($\theta°$) of Pd(PEt)$_3$ in the minimum (left) and maximum (right) conformations (blue = palladium; orange = phosphorus; gray = carbon; white = hydrogen).

When a metal center is not crowded, the conformation of maximum $\theta°$ is likely to be present, as this conformation is of lower energy in almost all cases studied. If even one section of the ligand is extended, the maximum $\theta°$ should be most informative, because in general the barrier to internal rotation about the M–P bond is small.[22-24] In an extreme case involving intramolecular arene stacking interactions between crowded ligands, barriers up to 12 kcal mol^{-1} were reported,[39] but such high barriers are not typical. Normally, both compact and extended conformations are seen in crystallographic studies.[44-46] Even so, one should be wary of the influence of crystal packing effects that could force ligands into a more compact conformation.

In the case of P(i-Bu)$_3$, a large disparity exists between the computed $\theta° = 214°$ and the standard Tolman $\theta = 143°$. The Tolman cone angle assumes an idealized model with each CH$_2$ group pointed downward toward the metal center, and each CH(CH$_3$)$_2$ facing up. The idealized structure is not realistic, because the metal center is surrounded by three nonbonded methylene hydrogens within their van der Waals radii. Our B3LYP geometry optimizations found that such a compact, idealized structure is not a minimum on the potential energy surface, and only a more extended ($\theta°$ max) conformer exists.

Table 2.2. Exact Cone Angles ($\theta°$, deg), Pd–P Bond Distances (r, Å), and Ph–P–Ph Angles ($\angle$, deg) of Triphenylphosphine (PPh$_3$) Ligands [a]

Complex	Source (ref.)	$\theta°$	r(Pd–P)	$\angle$ (Ph–P–Ph)
Pd(PPh$_3$)	B3LYP	170.0	2.23	103.1, 103.2, 103.3
Pd(PPh$_3$)$_2$(SN$_2$C$_3$)$_2$Cl	47	150.3	2.36	102.4, 103.4, 110.2
		155.4	2.35	102.5, 105.6, 105.6
Pd(PPh$_3$)(P$_2$OC$_{14}$H$_9$)Cl	48	151.4	2.30	98.1, 105.8, 107.5
Pd(PPh$_3$)(SN$_4$O$_2$C$_8$H$_7$)Cl	49	155.2	2.27	103.8, 105.1, 106.3
Pd(PPh$_3$)(SN$_3$C$_9$H$_{10}$)Cl	49	156.9	2.27	104.6, 104.7, 105.0
Pd(PPh$_3$)(SH)	50	160.8	2.33	103.4, 105.1, 106.6
Pd(PPh$_3$)$_2$(S$_3$NO$_2$C$_7$H$_5$)	50	160.9	2.34	102.9, 104.9, 106.6
		173.6	2.31	101.8, 102.9, 114.0
Pd(PPh$_3$)(SNC$_5$H$_4$)	47	163.1	2.34	99.1, 106.4, 107.3
Pd(PPh$_3$)(NFC$_{15}$H$_{15}$) Cl	51	165.9	2.25	102.1, 103.1, 105.6
Pd(PPh$_3$)(SN$_3$C$_{10}$H$_{11}$)	52	167.4	2.25	102.3, 104.1, 108.5
Pd(PPh$_3$)(S$_2$N$_3$C$_8$H$_9$)	52	167.7	2.24	102.8, 104.2, 108.6
Pd(PPh$_3$)(SN$_4$C$_8$H$_{10}$)	52	170.6	2.26	103.6, 104.6, 108.7
Pd(PPh$_3$)(NFC$_{11}$H$_{15}$) Cl	51	172.2	2.26	103.6, 103.3, 110.3

A striking difference between our cone angle and standard values occurs for triphenylphosphine (PPh$_3$), for which $\theta°$ is 25° and 41° larger than the Tolman and solid cone angles, respectively. Similarly, previous density functional computations[11] on the Pd–PPh$_3$ complex optimized a structure whose average vertex angle was 27° larger than the Tolman standard. To elucidate this disparity, the exact cone angle was calculated here from crystal structures of various complexes containing palladium ligated by PPh$_3$ (Table 2.2).[47-52] The $\theta°$ angle did not cluster around a standard value but varied up to 23° depending on the ligand environment. Two Pd complexes in the survey were ligated by two PPh$_3$ ligands and exhibited considerable internal mismatches (5° and 13°) in their cone angles. This difference in cone angles for the same type of ligand within the same complex shows that the steric bulk of a ligand can be significantly affected by the environment, highlighting the need for calculating exact cone angles for specific ligands rather than using an assumed universal value.

The Tolman method assumes tetrahedral bond angles of 109.5° about the phosphorus atom in totally symmetric ligands. In contrast, the average Ph–P–Ph bond angle among the crystal structures in Table 2.2 is 104.9°; moreover, distortions from local C_3 symmetry lead to differences as large as 12.2° in adjacent Ph–P–Ph bond angles. The flaws in the Tolman assumptions call for a method that gives the cone angle directly from atomic coordinates of the crystal structure with no approximations, as in our $\theta°$ approach.

To demonstrate that the $\theta°$ method is not limited to phosphorus-based ligands, the exact cone angle was computed for several common amine ligands (Table 2.3). The Tolman method sets an approximate Pd–N bond length of 2.20 Å;[10] however, the B3LYP palladium-nitrogen distances vary widely among the ligands, ranging between 2.13 Å to 2.37 Å. Several ligands have multiple conformations for which we have computed exact cone angles. The MAD of minimum $\theta°$ versus (θ, Θ) is (11.6°, 12.5°), (14.7°, 16.0°), and (11.5°, 15.6°) for Pd, Ni, and Pt complexes, respectively.

Table 2.3. Exact Cone Angles ($\theta°$) vs. Tolman[10] (θ) and Solid[8] (Θ) Cone Angles in degrees for an Array of Pd, Ni, and Pt Complexes with Common Amine Ligands[a]

Ligand	θ	Θ	$\theta°$(Pd)		$\theta°$(Ni)		$\theta°$(Pt)	
			Min	Max	Min	Max	Min	Max
NH_3	94	87	95.4	–	112.0	–	101.9	–
NMe_3	132	124	129.6	–	140.6	–	135.4	–
NEt_3	150	142	143.9	188.1	158.8	188.6	152.1	180.8
$N(i\text{-}Pr)_3$	220	161	183.5	195.0	196.8	202.5	187.5	191.7
NBz_3	–	173	148.7	237.6	165.4	228.0	157.9	218.0

[a] For $\theta°$, minimum (min) and maximum (max) values are given over the range of conformers.

No adjustments are needed for extension of the $\theta°$ method to multidentate ligands. The cone will encompass the entirety of the ligand without setting an artificial line at the P–M–P

bisector. We computed $\theta°$ for several common bidentate ligands bound to a palladium center (Table 2.4) and found values much larger than either the Tolman or solid cone angles. Again, a main assumption of the Tolman cone angle is tetrahedral geometry about the phosphorus atom.[1] This rough approximation greatly fails for the bidentate ligands studied. The Ni-P-bridge bond is decreased by roughly 10° compared to the tetrahedral angle, causing the ligand to extend downward and occupy increased area. For this reason, the cone angle for computationally optimized ligands is greater than that of an assumed tetrahedral geometry.

Table 2.4. Exact Cone Angles ($\theta°$) vs. Tolman[1,53] (θ) and Solid[21] ($\varTheta$) Cone Angles in degrees for Several Common Bidentate Ligands Bound to a Palladium Center

Ligand[a]	θ	$\varTheta$	$\theta°$
dmpe	107	156	199.4
depe	115	176	217.0
dppe	125	178	218.6
dppp	127	183	221.6
bpy	118	–	194.6

[a] dmpe, 1,2-bis(dimethylphosphino)ethane; depe, 1,2-bis(diethylphosphino) ethane; dppe, 1,2-bis(diphenylphosphino)ethane; dppp, 1,3-bis(diphenylphosphino)propane; bpy, 2,2′-bipyridine

Another factor is that the Tolman extension to bidentate ligands sets an artificial apex on the bisector of the P–M–P bond. The cone angle for half of the bidentate ligand is calculated using the outer non-bridging phosphine substituents and the bisector of the P–M–P angle; this value is then doubled to find the full cone angle. In contrast, the exact cone angle method constructs the most acute cone that properly encompasses the entire bidentate ligand, leading to larger $\theta°$ values. Because multidentate bonding prevents rotation of the M–P bond, right circular cones may overevaluate the steric demands of ovoid-shaped ligands. In these cases, the solid angle method may provide a more accurate measure of steric bulk. This dilemma is

inconsequential in square planar complexes, where there is no coordination in the axial position regardless of ligand bulk.

Conclusions

In this report, we have presented a new method for quantifying the steric bulk of ligands by computing an exact cone angle from the atomic positions without approximations. The fundamental concept behind the mathematics is finding the solution for the most acute right circular cone that contains all ligand atoms, each assumed to occupy a sphere with the corresponding van der Waals radius. The minimum cone is tangent to a maximum of three atoms, and analytic solutions are obtained by solving a quadratic equation for the cosine of the cone angle. The only information required is the Cartesian coordinates of the metal center and the ligand atoms, which may be provided by quantum chemical geometry optimizations or crystallographic structures, and the associated van der Waals radii. No artificial bond lengths are employed, and no idealized geometry is assumed. Our $\theta°$ method does not restrict the cone angle for a ligand to a universal value but allows variation according to the chemical environment.

We have computed structures for an array of phosphine and amine ligands bound to group 10 metal centers. The mean absolute deviations (MADs) of $\theta°$ were 15.2° compared with θ, and 18.3° with Θ for palladium-phosphine complexes. The MADs of $\theta°$ versus (θ, Θ) were (11.6°, 12.5°) for palladium-amine complexes. The Tolman cone angle typically underestimated sterics in phosphine ligands and overestimated amine ligands. The $\theta°$ for triphenylphosphine and derivatives are ~25° larger than the Tolman cone angles due to distortions in geometry and M–P bond lengths. Our computed cone angles are similar to those calculated from crystallographic data, though the range varies with increased steric crowding about the metal center.

References

(1) Tolman, C. A. *Chem. Rev.* **1977**, *77*, 313-348.

(2) Halpern, J.; Phelan, P. F. *J. Am. Chem. Soc.* **1972**, *94*, 1881-1886.

(3) Verstuyft, A. W.; Nelson, J. H. *Inorg. Chem.* **1975**, *14*, 1501-1505.

(4) Reger, D. L.; Ding, Y.; Garza, D. G.; Lebioda, L. *J. Organomet. Chem.* **1993**, *452*, 263-270.

(5) Alyea, E. C.; Dias, S. A.; Ferguson, G.; Roberts, P. J. *J. Chem. Soc., Dalton Trans.* **1979**, 948-951.

(6) Stockland, R. A.; Levine, A. M.; Giovine, M. T.; Guzei, I. A.; Cannistra, J. C. *Organometallics* **2004**, *23*, 647-656.

(7) Brown, T. L. *Inorg. Chem.* **1992**, *31*, 1286-1294.

(8) Brown, T. L.; Lee, K. J. *Coord. Chem. Rev.* **1993**, *128*, 89-116.

(9) Tolman, C. A.; Seidel, W. C.; Gosser, L. W. *J. Am. Chem. Soc.* **1974**, *96*, 53-60.

(10) Seligson, A. L.; Trogler, W. C. *J. Am. Chem. Soc.* **1991**, *113*, 2520-2527.

(11) Moore, L. R.; Western, E. C.; Craciun, R.; Spruell, J. M.; Dixon, D. A.; O'Halloran, K. P.; Shaughnessy, K. H. *Organometallics* **2008**, *27*, 576-593.

(12) Hill, L. L.; Moore, L. R.; Huang, R.; Craciun, R.; Vincent, A. J.; Dixon, D. A.; Chou, J.; Woltermann, C. J.; Shaughnessy, K. H. *J. Org. Chem.* **2006**, *71*, 5117-5125.

(13) DeVasher, R. B.; Spruell, J. M.; Dixon, D. A.; Broker, G. A.; Griffin, S. T.; Rogers, R. D.; Shaughnessy, K. H. *Organometallics* **2005**, *24*, 962-971.

(14) Hill, L. L.; Smith, J. M.; Brown, W. S.; Moore, L. R.; Guevera, P.; Pair, E. S.; Porter, J.; Chou, J.; Wolterman, C. J.; Craciun, R.; Dixon, D. A.; Shaughnessy, K. H. *Tetrahedron* **2008**, *64*, 6920-6934.

(15) Martín, A.; Orpen, A. G. *J. Am. Chem. Soc.* **1996**, *118*, 1464-1470.

(16) Bart, J. C. J.; Favini, G.; Todeschini, R. *Phosphorous Sulfur Rel. Elem.* **1983**, *17*, 205-220.

(17) White, D.; Coville, N. J. *Adv. Organomet. Chem.* **1994**, *36*, 95-158.

(18) Immirzi, A.; Musco, A. *Inorg. Chim. Acta* **1977**, *25*, L41-L42.

(19) White, D.; Taverner, B. C.; Leach, P. G. L.; Coville, N. J. *J. Comp. Chem.* **1993**, *14*, 1042-1049.

(20) Taverner, B. C. *J. Comp. Chem.* **1996**, *17*, 1612-1623.

(21) Niksch, T.; Görls, H.; Weigand, W. *Eur. J. Inorg. Chem.* **2010**, *2010*, 95-105.

(22) DiMeglio, C. M.; Luck, L. A.; Rithner, C. D.; Rheingold, A. L.; Elcesser, W. L.; Hubbard, J. L.; Bushweller, C. H. *J. Phys. Chem.* **1990**, *94*, 6255-6263.

(23) Muetterties, E. L. *Acc. Chem. Res.* **1970**, *3*, 266-273.

(24) Bushweller, C. H.; Rithner, C. D.; Butcher, D. J. *Inorg. Chem.* **1986**, *25*, 1610-1616.

(25) Hillier, A. C.; Sommer, W. J.; Yong, B. S.; Petersen, J. L.; Cavallo, L.; Nolan, S. P. *Organometallics* **2003**, *22*, 4322-4326.

(26) Clavier, H.; Nolan, S. P. *Chem. Commun.* **2010**, *46*, 841-861.

(27) Fey, N.; Harvey, J. N.; Lloyd-Jones, G. C.; Murray, P.; Orpen, A. G.; Osborne, R.; Purdie, M. *Organometallics* **2008**, *27*, 1372-1383.

(28) Lee, C.; Yang, W.; Parr, R. G. *Phys. Rev. B* **1988**, *37*, 785-789.

(29) Becke, A. D. *J. Chem. Phys.* **1993**, *98*, 5648-5652.

(30) Shao, Y.; Fusti-Molnar, L.; Jung, Y.; Kussmann, J.; Ochsenfeld, C.; Brown, S. T.; Gilbert, A. T. B.; Slipchenko, L. V.; Levchenko, S. V.; O'Neill, D. P.; Distasio Jr, R. A.; Lochan, R. C.; Wang, T.; Beran, G. J. O.; Besley, N. A.; Herbert, J. M.; Yeh Lin, C.; Van Voorhis, T.; Hung Chien, S.; Sodt, A.; Steele, R. P.; Rassolov, V. A.; Maslen, P. E.; Korambath, P. P.; Adamson, R. D.; Austin, B.; Baker, J.; Byrd, E. F. C.; Dachsel, H.; Doerksen, R. J.; Dreuw,

A.; Dunietz, B. D.; Dutoi, A. D.; Furlani, T. R.; Gwaltney, S. R.; Heyden, A.; Hirata, S.; Hsu, C.-P.; Kedziora, G.; Khalliulin, R. Z.; Klunzinger, P.; Lee, A. M.; Lee, M. S.; Liang, W.; Lotan, I.; Nair, N.; Peters, B.; Proynov, E. I.; Pieniazek, P. A.; Min Rhee, Y.; Ritchie, J.; Rosta, E.; David Sherrill, C.; Simmonett, A. C.; Subotnik, J. E.; Lee Woodcock III, H.; Zhang, W.; Bell, A. T.; Chakraborty, A. K.; Chipman, D. M.; Keil, F. J.; Warshel, A.; Hehre, W. J.; Schaefer III, H. F.; Kong, J.; Krylov, A. I.; Gill, P. M. W.; Head-Gordon, M. *Phys. Chem. Chem. Phys.* **2006**, *8*, 3172-3191.

(31) Dill, J. D.; Pople, J. A. *J. Chem. Phys.* **1975**, *62*, 2921-2923.

(32) Francl, M. M.; Pietro, W. J.; Hehre, W. J.; Binkley, J. S.; Gordon, M. S.; DeFrees, D. J.; Pople, J. A. *J. Chem. Phys.* **1982**, *77*, 3654-3665.

(33) Hay, P. J.; Wadt, W. R. *J. Chem. Phys.* **1985**, *82*, 299-310.

(34) Wolfram Research, Inc., *Mathematica*, Version 8.0, Champaign, IL **2010**.

(35) Bondi, A. *J. Phys. Chem.* **1964**, *68*, 441-451.

(36) Niu, S.; Hall, M. B. *Chem. Rev.* **2000**, *100*, 353-406.

(37) Xu, Z.-F.; Xie, Y.; Feng, W.-L.; Schaefer, H. F. *J. Phys. Chem. A* **2003**, *107*, 2716-2729.

(38) Niu, S.; Hall, M. B. *J. Phys. Chem. A* **1997**, *101*, 1360-1365.

(39) Fanizzi, F. P.; Lanfranchi, M.; Natile, G.; Tiripicchio, A. *Inorg. Chem.* **1994**, *33*, 3331-3339.

(40) Costello, J. F.; Davies, S. G. *J. Chem. Soc.-Perkin Trans. 2* **1998**, 1683-1689.

(41) Smith, J. M.; Coville, N. J. *Organometallics* **2001**, *20*, 1210-1215.

(42) Bunten, K. A.; Chen, L.; Fernandez, A. L.; Poë, A. J. *Coord. Chem. Rev.* **2002**, *233–234*, 41-51.

(43) Ferguson, G.; Roberts, P. J.; Alyea, E. C.; Khan, M. *Inorg. Chem.* **1978**, *17*, 2965-2967.

(44) Munro-Leighton, C.; Adduci, L. L.; Becker, J. J.; Gagné, M. R. *Organometallics* **2011**, *30*, 2646-2649.

(45) Charmant, J. P. H.; Espinet, P.; Soulantica, K. *Acta Crystallogr., Sect. E: Struct. Rep. Online* **2001**, *57*, m451-m453.

(46) Englert, U.; Matern, E.; Olkowska-Oetzel, J.; Pikies, J. *Acta Crystallogr., Sect. E: Struct. Rep. Online* **2003**, *59*, m376-m377.

(47) Nadeem, S.; Bolte, M.; Ahmad, S.; Fazeelat, T.; Tirmizi, S. A.; Rauf, M. K.; Sattar, S. A.; Siddiq, S.; Hameed, A.; Haider, S. Z. *Inorg. Chim. Acta* **2010**, *363*, 3261-3269.

(48) Karami, K.; Rizzoli, C.; Salah, M. M. *J. Organomet. Chem.* **2011**, *696*, 940-945.

(49) Paul, P.; Datta, S.; Halder, S.; Acharyya, R.; Basuli, F.; Butcher, R. J.; Peng, S.-M.; Lee, G.-H.; Castineiras, A.; Drew, M. G. B.; Bhattacharya, S. *J. Mol. Cat. A: Chem.* **2011**, *344*, 62-73.

(50) Singh, N.; Singh, B.; Thapliyal, K.; Drew, M. G. B. *Inorg. Chim. Acta* **2010**, *363*, 3589-3596.

(51) Thomas, H. R.; Deeth, R. J.; Clarkson, G. J.; Rourke, J. P. *Organometallics* **2011**, *30*, 5641-5648.

(52) Lobana, T. S.; Kumari, P.; Butcher, R. J.; Akitsu, T.; Aritake, Y.; Perles, J.; Fernandez, F. J.; Vega, M. C. *J. Organomet. Chem.* **2012**, *701*, 17-26.

(53) Bessel, C. A.; Margarucci, J. A.; Acquaye, J. H.; Rubino, R. S.; Crandall, J.; Jircitano, A. J.; Takeuchi, K. J. *Inorg. Chem.* **1993**, *32*, 5779-5784.

CHAPTER 3

EXACT LIGAND SOLID ANGLES
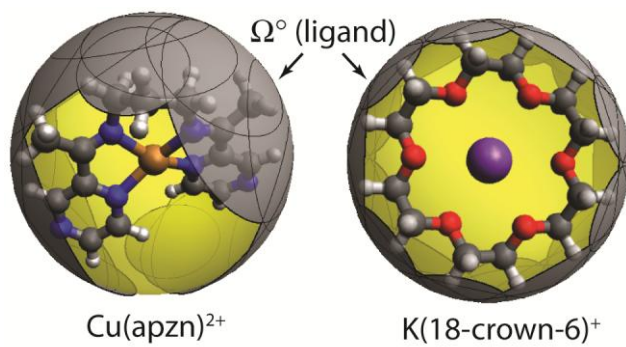
Ω° (ligand)

Cu(apzn)²⁺   K(18-crown-6)⁺

Abstract

Steric demands of a ligand can be quantified by the area occluded by the ligand on the surface of an encompassing sphere centered at the metal atom. When viewed as solid spheres illuminated by the metal center, the ligand atoms generally cast a very complicated collective shadow onto the encompassing sphere, causing mathematical difficulties in computing the subtended solid angle. Herein, an exact, analytic solution to the ligand solid angle integration problem is presented based on a line integral around the multisegmented perimeter of the ligand shadow. The solution, which is valid for any ligand bound to any metal center, provides an excellent method for analyzing geometric structures from quantum chemical computations or X-ray crystallography. Over 275 structures of various metals bound to diverse mono- and multidentate ligands were optimized using B3LYP density functional theory to exhibit exact solid angle ($\Omega°$) computations. Among the intriguing $\Omega°$ solutions, Pd(xantphos) and ferrocene exhibit holes in their ligand shadows, and Fe(EDTA)$^{2-}$ has a surprisingly simple shadow defined by only four arcs, despite having a multitude of overlaps among individual shadow cones.

Introduction

Steric properties of multidentate ligands influence activity and selectivity of organometallic catalysts[1-4] and affect binding affinities to metal ions through the chelate effect.[5] The steric demands of a ligand can be gauged by properties of the backbone such as metal(M)-donor(D) bite angles ($\angle$ D–M–D), or by the entire ligand encumbrance, as in the cone and solid angle descriptions.[6,7] Both types of descriptors have shown correlations to catalyst selectivity for a variety of organometallic reactions.[8-11]

The bite angle of bidentate ligands depends on the donor-donor distance, which is affected by the covalent radius of the chelated metal.[12] Because this radius varies greatly among transition metals,[13] ascribing a single bite angle to a given ligand is unsatisfactory. However, ligand bite angles can be standardized for chelation to a group of metals with similar radii.[12] The bite angle cannot describe additional steric demands of backbone substituents, the dynamic nature of flexible ligands, or the ability of ligands to mesh into one another.[14]

The Tolman cone angle (θ) was developed to measure the steric demands of a monodentate ligand and later extended to bidentate ligands.[6,15] Experimental "cone angle equivalents" have been assigned by measuring the rates for association of P-donor ligands to metal carbonyls.[16] In a recent publication, we developed an analytic method to determine an exact cone angle ($\theta°$) of any ligand in any environment without approximations such as fixing the M−D bond length, centering the cone on the M−D bond, or averaging apex angles for asymmetrical ligands.[17] Our mathematically rigorous method determines $\theta°$ by exactly solving for the most acute cone possible that contains the entire ligand. Nonetheless, the θ and $\theta°$ cone angle approaches are most effective for flexible, monodentate ligands that undergo unhindered rotation and do not satisfactorily treat cases of ligand meshing.[18]

An alternative steric descriptor to the Tolman cone angle is the solid cone angle (Θ),[7,19-21] which is especially beneficial when the ligand is highly asymmetric or rotationally hindered, as in multidentate ligands. Because Θ accounts for indentations in the ligand profile, these parameters should be systematically smaller than their Tolman counterparts, although there is a non-linear relationship between cone and solid angles.[22] In rotationally hindered environments, indentations can allow ligands to mesh together into a more compact shape. The Θ parameter is defined as $2\cos^{-1}(1 - \frac{1}{2\pi}\Omega)$, where Ω is the solid angle of the complete shadow cast by a ligand when hypothetically illuminated from the metal center. Considered as a solid sphere, each ligand atom produces a shadow cone, resulting in a very complicated collective ligand shadow. An arbitrary number of overlapping shadow cones causes daunting analytic difficulties in the computation of Ω. The collective shadow and numerous overlapping cones of the large ligand 2,2′-bis(diphenylphosphino)-1,1′-binaphthyl (BINAP) are depicted in Fig. 3.1.
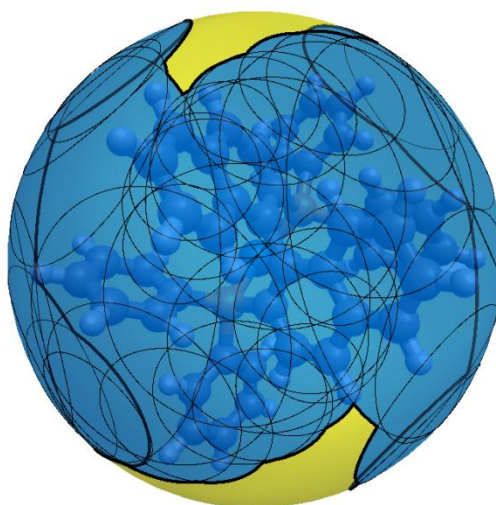
Figure 3.1. The occluded area (blue) determining the ligand solid angle of Pd(BINAP) results from the intricate overlap of many shadow cones (circles) of the individual atoms. Two indentations (yellow) in the ligand profile are prominent.

Because no analytic solution to the solid angle integration problem was known, detailed algorithms were devised in the 1990s to reduce errors in Ω from overlapping shadows. The refined scheme of Taverner[20,23] is based on the equation

$$\Omega = \sum_i 2\pi(1 - \cos\alpha_i) - \sum_{i>j} A_{ij} + \sum_{i>j>k} A_{ijk} - \sum_{i>j>k>l} A_{ijkl} + \cdots, \quad (1)$$

in which the leading term is a sum over the solid angles of the individual ligand shadow cones with apex angle α_i, and the successive corrections (A_{ij}, A_{ijk}, A_{ijkl}, …) approximate the solid angles (Ω_{ij}, Ω_{ijk}, Ω_{ijkl}, …) of (double, triple, quadruple, …) overlaps between these cones. In evaluating each (A_{ij}, A_{ijk}, A_{ijkl}, …) quantity, the ligand shadow is projected from the surface of the encompassing sphere onto an underlying plane (σ_{ij}, σ_{ijk}, σ_{ijkl}, …) specific to each overlap region. The projection yields intersecting ellipses whose common area is numerically integrated and equated to the corresponding (A_{ij}, A_{ijk}, A_{ijkl}, …) overlap correction. The procedure is illustrated in Fig. 3.2 for the case of two overlapping shadow cones. The Taverner approach has been supplanted by more direct numerical integration of solid angles in current computer programs such as Solid-G.[22]
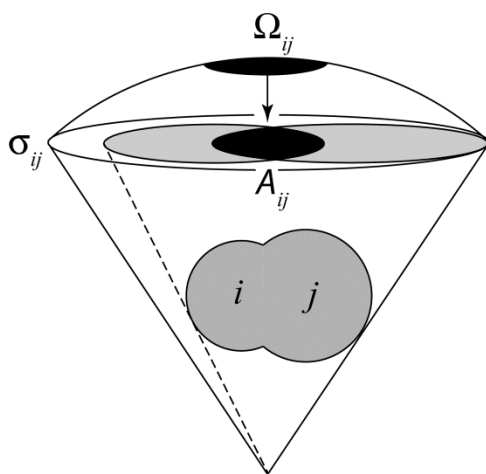
Figure 3.2. An earlier scheme[23] to account for overlap in ligand solid angle computations. The overlap region (black, above) of the shadow cones of two ligand atoms i and j (gray) on the encompassing sphere subtends a solid angle Ω_{ij}. Projection onto an underlying plane σ_{ij} estimates Ω_{ij} as the overlap area A_{ij} (black, below) common to intersecting ellipses (gray).

Assorted other methods to quantify the steric encumbrance of a ligand have been advanced,[19] but none are as widespread as the Tolman and solid angle approaches. Our recent paper on exact cone angles[17] succinctly reviews currently available steric descriptors and some of their applications. Some rely on computed repulsive energies[24,25] and interaction energies[26] between ligand atoms and selectively placed artificial fragments, whereas others are purely geometrical constructs.[27,28] While many descriptors describe the behavior of individual ligands, few have sought to describe multiple ligand coordination simultaneously.[22,29-31]

Herein, we present a complete analytic solution to the ligand solid angle integration problem that avoids the surface integral approach and instead uses a line integral around the multi-segmented perimeter of the ligand shadow. In this manner exact ligand solid angles ($\Omega°$) can be evaluated from compact formulas for any ligand of any shape in any environment, with no approximations whatsoever and no need to quantify problematic overlap regions as in Eq. (1). The designation "exact" in this context refers to the mathematical solution for a given molecular structure, not to the accuracy of the input atomic coordinates. To demonstrate the effectiveness of our method, $\Omega°$ and parameters derived from it were computed for over 275 organometallic structures optimized using B3LYP density functional theory with effective core potentials for the transition metals. The applications include a wide array of monodentate phosphine and amine ligands bound to Pd, Ni, and Pt, about twenty multidentate ligands bound to Pd, and miscellaneous multidentate complexes of Cr, Ti, Ni, Cu, Mo, and Fe. Accompanying this report is a computer program to determine the exact solid angle from the Cartesian coordinates of the molecule and any choice of atomic radii, such as traditional Bondi values or more recent alternatives.[22]

Mathematical Formulation

The solid angle of an arbitrary closed loop on a sphere can be determined from a line integral around the boundary. To derive an exact formula, the loop is first discretized into an N-sided polygon, and then the limit as N goes to infinity is taken. The solid angle subtended by a geodesic polygon of N sides lying on a unit sphere is given by the known formula:

$$\Omega_N = \sum_j^N \psi_j - (N-2)\pi , \tag{2}$$

where ψ_j denotes the interior angles at the vertices. This equation arises from decomposition of the polygon into geodesic triangles and application of Girard's Theorem.[32] Any kinks in the loop where the tangent vectors are discontinuous should be separated from the other vertices before the limit of large N is taken. Thus,

$$\Omega_{\text{loop}} = \lim_{N\to\infty} \Omega_N = \sum_j^n \beta_j - (n-2)\pi - \lim_{N\to\infty} \sum_j^{N-n}(\pi - \psi_j) , \tag{3}$$

where β_j denotes one of the fixed interior angles of the n kinks.

To compute the vanishingly small $\pi - \psi_j$ angle at a point $\boldsymbol{u}(t)$ on the curve, consider the adjacent points $\boldsymbol{v} = \boldsymbol{u}(t+\Delta t)$ and $\boldsymbol{w} = \boldsymbol{u}(t-\Delta t)$. By application of the Spherical Law of Cosines[32] to the triangle formed by $\boldsymbol{u}$, $\boldsymbol{v}$, and $\boldsymbol{w}$,

$$\cos\psi = \csc a \csc b (\cos c - \cos a \cos b) \tag{4}$$

where

$$(\cos a, \cos b, \cos c) = (\boldsymbol{u} \cdot \boldsymbol{v}, \boldsymbol{u} \cdot \boldsymbol{w}, \boldsymbol{v} \cdot \boldsymbol{w}) . \tag{5}$$

Using Eq. (4) to solve for $\sin\psi$, we find

$$\sin\psi = \pm\sqrt{1 - \frac{[\boldsymbol{v}\cdot\boldsymbol{w} - (\boldsymbol{u}\cdot\boldsymbol{w})(\boldsymbol{u}\cdot\boldsymbol{v})]^2}{[1-(\boldsymbol{u}\cdot\boldsymbol{v})^2][1-(\boldsymbol{u}\cdot\boldsymbol{w})^2]}} . \tag{6}$$

The quantities in the radicand of Eq. (6) can be expanded in powers of Δt; the expansion coefficients are given explicitly in Table 3.1. Because the tangent vectors $\dot{\boldsymbol{u}}$ are perpendicular to

the surface normal vectors of the sphere, $u\cdot\dot{u}=0$ for all points on the curve. Taking successive derivatives of this orthogonality condition yields $\dot{u}\cdot\dot{u}+u\cdot\ddot{u}=0$, $3\dot{u}\cdot\ddot{u}+u\cdot\dddot{u}=0$, and $3\ddot{u}\cdot\ddot{u}+4\dot{u}\cdot\dddot{u}+u\cdot\ddddot{u}=0$. These formulas have been used in Table 3.1 to eliminate the highest derivatives in each term.

Table 3.1. Coefficients in the Expansion of Sinψ Along the Curve $u(t)$

Quantity	Powers of Δt				
	0	1	2	3	4
$u\cdot v$	1	0	$-\frac{1}{2}\dot{u}\cdot\dot{u}$	$-\frac{1}{2}\dot{u}\cdot\ddot{u}$	$-\frac{1}{8}\ddot{u}\cdot\ddot{u}-\frac{1}{6}\dot{u}\cdot\dddot{u}$
$u\cdot w$	1	0	$-\frac{1}{2}\dot{u}\cdot\dot{u}$	$\frac{1}{2}\dot{u}\cdot\ddot{u}$	$-\frac{1}{8}\ddot{u}\cdot\ddot{u}-\frac{1}{6}\dot{u}\cdot\dddot{u}$
$v\cdot w$	1	0	$-2\dot{u}\cdot\dot{u}$	0	$-\frac{2}{3}\dot{u}\cdot\dddot{u}$
$(u\cdot v)(u\cdot w)$	1	0	$-\dot{u}\cdot\dot{u}$	0	$\frac{1}{4}(\dot{u}\cdot\dot{u})^2-\frac{1}{4}\ddot{u}\cdot\ddot{u}-\frac{1}{3}\dot{u}\cdot\dddot{u}$
$(v\cdot w)-(u\cdot v)(u\cdot w)$	0	0	$-\dot{u}\cdot\dot{u}$	0	$\frac{1}{4}\ddot{u}\cdot\ddot{u}-\frac{1}{3}\dot{u}\cdot\dddot{u}-\frac{1}{4}(\dot{u}\cdot\dot{u})^2$
$[(v\cdot w)-(u\cdot v)(u\cdot w)]^2\,(\Delta t)^{-2}$	0	0	$(\dot{u}\cdot\dot{u})^2$	0	$(\dot{u}\cdot\dot{u})\left[\frac{1}{2}(\dot{u}\cdot\dot{u})^2-\frac{1}{2}\ddot{u}\cdot\ddot{u}+\frac{2}{3}\dot{u}\cdot\dddot{u}\right]$
$1-(u\cdot v)^2$	0	0	$\dot{u}\cdot\dot{u}$	$\dot{u}\cdot\ddot{u}$	$\frac{1}{4}\ddot{u}\cdot\ddot{u}+\frac{1}{3}\dot{u}\cdot\dddot{u}-\frac{1}{4}(\dot{u}\cdot\dot{u})^2$
$1-(u\cdot w)^2$	0	0	$\dot{u}\cdot\dot{u}$	$-\dot{u}\cdot\ddot{u}$	$\frac{1}{4}\ddot{u}\cdot\ddot{u}+\frac{1}{3}\dot{u}\cdot\dddot{u}-\frac{1}{4}(\dot{u}\cdot\dot{u})^2$
$\left[1-(u\cdot v)^2\right]\left[1-(u\cdot w)^2\right](\Delta t)^{-2}$	0	0	$(\dot{u}\cdot\dot{u})^2$	0	$(\dot{u}\cdot\dot{u})\left[\frac{1}{2}\ddot{u}\cdot\ddot{u}+\frac{2}{3}\dot{u}\cdot\dddot{u}-\frac{1}{2}(\dot{u}\cdot\dot{u})^2\right]-(\dot{u}\cdot\ddot{u})^2$

Placing these results into Eq. (6) and invoking the usual expansion $(1+\delta)^{-1}=1-\delta+\delta^2-$ … for small δ, we obtain

$$\sin\psi = \pm\Delta t(\dot{u}\cdot\dot{u})^{-1}\sqrt{(\dot{u}\cdot\dot{u})(\ddot{u}\cdot\ddot{u})-(\dot{u}\cdot\dot{u})^3-(\dot{u}\cdot\ddot{u})^2}+O[(\Delta t)^2]\ . \quad (7)$$

Therefore, in the limit of infinitesimal Δt,

$$d(\pi-\psi) = \pm dt(\dot{u}\cdot\dot{u})^{-1}\sqrt{(\dot{u}\cdot\dot{u})(\ddot{u}\cdot\ddot{u})-(\dot{u}\cdot\dot{u})^3-(\dot{u}\cdot\ddot{u})^2}\ . \quad (8)$$

As N goes to infinity, Eq. (3) becomes

$$\Omega_{\text{loop}} = \sum_j^n \beta_j - (n-2)\pi - \oint dt\, p(t)(\dot{u}\cdot\dot{u})^{-1}\sqrt{(\dot{u}\cdot\dot{u})(\ddot{u}\cdot\ddot{u})-(\dot{u}\cdot\dot{u})^3-(\dot{u}\cdot\ddot{u})^2}, \quad (9)$$

where $[p(t)=1, p(t)=-1]$ if the curvature vector is directed (toward, away from) the interior of the loop. Assuming that the line integral is performed in a counterclockwise direction around the

loop, we can assign

$$p(t) = \text{sgn}[\boldsymbol{u} \cdot (\dot{\boldsymbol{u}} \times \ddot{\boldsymbol{u}})] \ . \tag{10}$$

The interior angle at the kinks can also be replaced by the (unsigned) turn angle τ_k defined by

$$\beta_k = \pi - p_k \tau_k \ , \tag{11}$$

where ($p_k = 1$, $p_k = -1$) for a turn corresponding to interior angles ($<180°$, $>180°$), respectively. The general equation for the solid angle subtended by an arbitrary loop is thus

$$\Omega_{\text{loop}} = 2\pi - \sum_k^n p_k \tau_k - \oint dt \, \text{sgn}[\boldsymbol{u} \cdot (\dot{\boldsymbol{u}} \times \ddot{\boldsymbol{u}})](\dot{\boldsymbol{u}} \cdot \dot{\boldsymbol{u}})^{-1}$$

$$\times \sqrt{(\dot{\boldsymbol{u}} \cdot \dot{\boldsymbol{u}})(\ddot{\boldsymbol{u}} \cdot \ddot{\boldsymbol{u}}) - (\dot{\boldsymbol{u}} \cdot \dot{\boldsymbol{u}})^3 - (\dot{\boldsymbol{u}} \cdot \ddot{\boldsymbol{u}})^2} \ . \tag{12}$$

Any curve on the unit sphere can be represented using polar and azimuthal angles (θ, ϕ) that depend on some parameter t. For this purpose it is convenient to define the orthogonal unit vectors

$$\boldsymbol{e}_1 = \left(\sin\theta\cos\phi, \sin\theta\sin\phi, \cos\theta\right) \ , \tag{13}$$

$$\boldsymbol{e}_2 = \left(\cos\theta\cos\phi, \cos\theta\sin\phi, -\sin\theta\right), \tag{14}$$

and

$$\boldsymbol{e}_3 = \left(-\sin\phi, \cos\phi, 0\right) \ , \tag{15}$$

which obey $\boldsymbol{e}_1 \times \boldsymbol{e}_2 = \boldsymbol{e}_3$, $\boldsymbol{e}_2 \times \boldsymbol{e}_3 = \boldsymbol{e}_1$, and $\boldsymbol{e}_3 \times \boldsymbol{e}_1 = \boldsymbol{e}_2$. The first derivatives of these vectors with respect to the parameter t are

$$\dot{\boldsymbol{e}}_1 = \boldsymbol{e}_2 \dot{\theta} + \dot{\phi}\sin\theta\boldsymbol{e}_3, \tag{16}$$

$$\dot{\boldsymbol{e}}_2 = -\dot{\theta}\boldsymbol{e}_1 + \dot{\phi}\cos\theta\boldsymbol{e}_3, \tag{17}$$

and

$$\dot{\boldsymbol{e}}_3 = -\dot{\phi}\sin\theta\boldsymbol{e}_1 - \dot{\phi}\cos\theta\boldsymbol{e}_2. \tag{18}$$

The vectors required in Eq. (12) can then be represented as

$$u = e_1,$$ (19)

$$\dot{u} = \dot{\theta} e_2 + \dot{\phi} \sin\theta e_3 ,$$ (20)

$$\ddot{u} = -\left(\dot{\phi}^2 \sin^2\theta + \dot{\theta}^2\right) e_1 + \left(\ddot{\theta} - \dot{\phi}^2 \sin\theta\cos\theta\right) e_2 + (\ddot{\phi}\sin\theta + 2\dot{\phi}\dot{\theta}\cos\theta) e_3,$$ (21)

and

$$\dot{u} \times \ddot{u} = \left[\dot{\theta}(\ddot{\phi}\sin\theta + 2\dot{\phi}\dot{\theta}\cos\theta) - \dot{\phi}\sin\theta\left(\ddot{\theta} - \dot{\phi}^2 \sin\theta\cos\theta\right)\right] e_1$$

$$- \dot{\phi}\sin\theta\left(\dot{\phi}^2 \sin^2\theta + \dot{\theta}^2\right) e_2 + \dot{\theta}\left(\dot{\phi}^2 \sin^2\theta + \dot{\theta}^2\right) e_3.$$ (22)

Therefore,

$$\dot{u} \cdot \dot{u} = g_1(t) = \dot{\theta}^2 + \dot{\phi}^2 \sin^2\theta,$$ (23)

$$\ddot{u} \cdot \dot{u} = g_2(t) = \dot{\theta}\left(\ddot{\theta} - \dot{\phi}^2 \sin\theta\cos\theta\right) + \dot{\phi}\sin\theta(\ddot{\phi}\sin\theta + 2\dot{\phi}\dot{\theta}\cos\theta),$$ (24)

$$\ddot{u} \cdot \ddot{u} = g_3(t) = \left(\dot{\phi}^2 \sin^2\theta + \dot{\theta}^2\right)^2 + \left(\ddot{\phi}\sin\theta + 2\dot{\phi}\dot{\theta}\cos\theta\right)^2$$

$$+ \left(\ddot{\theta} - \dot{\phi}^2 \sin\theta\cos\theta\right)^2,$$ (25)

and

$$p(t) = \mathrm{sgn}\left[\dot{\theta}(\ddot{\phi}\sin\theta + 2\dot{\phi}\dot{\theta}\cos\theta) - \dot{\phi}\sin\theta\left(\ddot{\theta} - \dot{\phi}^2 \sin\theta\cos\theta\right)\right].$$ (26)

The resulting scalar form of Eq. (12) is

$$\Omega_{\mathrm{loop}} = 2\pi - \sum_k^n p_k \tau_k - \oint dt \frac{p(t)}{g_1(t)} \sqrt{g_1(t)g_3(t) - [g_1(t)]^3 - [g_2(t)]^2} ,$$ (27)

which is valid for general loops. In applying Eq. (27), the line integral should be broken up into the intervals between the kinks, as well as regions with the same value of $p(t)$.

As an application of Eq. (27), consider the solid angle subtended by a partial cone

bounded by closed Loop 0 comprising Paths $A + B + C$ in Figure 3.3. Let α_k be the apex angle of the acute cone k, while $\Delta\phi_k$ denotes the change in the local azimuthal angle for the corresponding circular arc on the unit sphere. The vertices ($\boldsymbol{a}$, $\boldsymbol{b}$, $\boldsymbol{c}$) have turn angles (τ_a, τ_b, τ_c) = ($\frac{1}{2}\pi$, $\Delta\phi_1 - \pi$, $\frac{1}{2}\pi$) and curvature signs (p_a, p_b, p_c) = (1, −1, 1), in order. Table 3.2 specifies the quantities needed to perform the line integrals $L = L_A + L_B + L_C$ in Eq. (27); remarkably, all functions in the integrand are constant, making the integration trivial. Note that the line integrals L_B and L_C are zero, reflecting the fact that arcs along geodesics make no contribution to the solid angle. Inserting the components into Eq. (27),

$$\Omega_{\text{loop0}} = 2\pi - \tau_a + \tau_b - \tau_c - L_A - L_B - L_C = \Delta\phi_1(1 - \cos\alpha) . \qquad (28)$$

If $\Delta\phi_1 = 2\pi$, the cone would be complete, and $\Omega_{\text{loop}} = 2\pi(1 - \cos\alpha_1)$, reproducing the standard formula for the solid angle of a cone.

Table 3.2. Components of the Total Line Integral $L = L_A + L_B + L_C$ of Loop 0

Path	$t \in$	$\phi(t)$	$\theta(t)$	$\dot{\phi}$	$\ddot{\phi}$	$\dot{\theta}$	$\ddot{\theta}$	$g_1(t)$	$g_2(t)$	$g_3(t)$	$p(t)$	L_{path}
A	$(0, \phi_1)$	t	α_1	1	0	0	0	$\sin^2\alpha_1$	0	$\sin^2\alpha_1$	1	$\Delta\phi_1 \cos\alpha_1$
B	$(^\pi/_2, 0)$	ϕ_1	t	0	0	1	0	1	0	1	0	0
C	$(0, {}^\pi/_2)$	0	t	0	0	1	0	1	0	1	0	0

When ligand solid angles are being computed, the arcs on the surface of the unit sphere are formed by intersections with shadow cones; hence, each arc contributes $\Delta\phi_k\cos\alpha_k$ to the line integral, in accord with the exercise above. Figure 3.3 illustrates the geometric considerations of this application. Two types of loops are encountered, designated here as convex and concave. Traversing the convex perimeter Loop 1 counterclockwise corresponds to positive azimuthal-angle changes $\Delta\phi_k$, and all turn angles have $p_k = -1$ because each interior angle is greater than 180°. In contrast, traversing concave interior Loop 2 counterclockwise involves negative changes

in the local azimuthal angles, and all turn angles have $p_k = 1$. However, the solid angle Ω_2 subtended by Loop 2 is already counted in the solid angle Ω_1 computed for Loop 1. Thus, when summing over all loops to obtain the total ligand solid angle $(\Omega°)$, the Ω_2 term should be given a negative sign to subtract out the hole in the ligand shadow traced by Loop 2. This type of accounting for all loops leads to an elegant and exact equation for the total ligand solid angle,

$$\Omega° = \sum_l^{\text{loops}}\left(2\pi + \sum_k^n \tau_{k,l} - \sum_k^{\text{arcs}}\left|\Delta\phi_{k,l}\cos\alpha_{k,l}\right|\right) - 4\pi N_{\text{concave}} , \qquad (29)$$

where N_{concave} is the number of loops (type 2) whose concave domain is fully contained in the convex domain of some other loop.
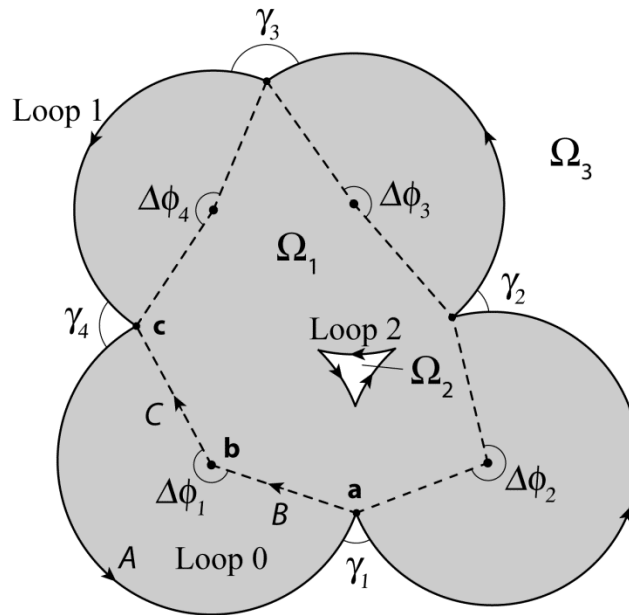
Figure 3.3. Three possible loops defined by the collective ligand shadow on the surface of the encompassing sphere. Loop 0 comprises Paths A + B + C subtending a partial cone; Loop 1 is a convex loop of four arcs and vertices formed by the entire perimeter; and Loop 2 is an interior concave loop with three arcs and vertices bounding a hole in the ligand shadow. The supplement of each turn angle is labeled as $\gamma_k = \pi - \tau_k$.

To ascertain N_{concave}, we recognize that the curvature vector for every arc of each loop points toward the convex domain and that the union of the convex and concave domains for any

loop is the entire surface of the unit sphere. In Fig. 3.3, (Ω_1, Ω_2) measures the (convex, concave) domain of (Loop 1, Loop 2). The region with solid angle $\Omega_3 = 4\pi - \Omega_1$ is in the concave domain of Loop 1 but the convex domain of Loop 2. According to the mathematical definitions of topology, the convex domains discussed here are actually star-convex sets, and the concave domains are technically non-star-convex sets.

The procedure to determine an exact ligand solid angle via Eq. (29) is as follows:

(1) From the molecular geometry and an adopted set of atomic radii, determine the axis and apex angle of the shadow cone of each ligand atom.[17]

(2) Find all intersection points between the circles on the unit sphere bounding the shadow cones of individual atoms; a list of local azimuthal angles $\phi_{k,j}$ is needed to specify and order the points on cone k where an intersection occurs with cone j.

(3) Identify the boundary arcs that form encompassing loops on the unit sphere; non-boundary arcs can be excluded by showing that their midpoints lie inside the shadow cone of another atom.

(4) Within each boundary loop, compute the $\Delta\phi_k$ local azimuthal angles subtended by each arc on the basis of the $\phi_{k,j}$ list from Step (2).

(5) For each vertex point within each loop, compute the turn angle τ_k.

(6) Assemble the components of Eq. (29) for each loop and compute the total solid angle $\Omega°$. In practice, no procedure is needed to find $N_{concave}$, because this quantity must equal the unique integer that places $\Omega°$ in the proper interval of $[0, 4\pi]$ steradians.

Attention must now be focused on finding working equations for $\phi_{k,j}$ in Step (2) and τ_k in Step (5), upon which the solid angle procedure is contingent.

The conditions that determine a point $\boldsymbol{u}$ on the unit sphere at which the two cones j and k intersect are $\boldsymbol{u} \cdot \boldsymbol{n}_j = \cos \alpha_j$, $\boldsymbol{u} \cdot \boldsymbol{n}_k = \cos \alpha_k$, and $\boldsymbol{u} \cdot \boldsymbol{u} = 1$, where unit vectors $\boldsymbol{n}_j$ and $\boldsymbol{n}_k$ specify the cone axes. We can restrict ourselves to apex angles $\alpha_k \leq {}^\pi/_2$, because only one branch of the cone equation corresponds to a shadow cast by a ligand atom on the unit sphere. Three coefficients a_{kj}, b_{kj}, and c_{kj} can be used to represent $\boldsymbol{u}$ as

$$\boldsymbol{u} = a_{kj}\boldsymbol{n}_j + b_{kj}\boldsymbol{n}_k + c_{kj}(\boldsymbol{n}_j \times \boldsymbol{n}_k) \,. \tag{30}$$

Applying the three conditions on $\boldsymbol{u}$ to Eq. (30) provides

$$\cos \alpha_j = a_{kj} + b_{kj} \cos \alpha_{jk}, \tag{31}$$

$$\cos \alpha_k = a_{kj} \cos \alpha_{jk} + b_{kj}, \tag{32}$$

and

$$1 = a_{kj}^2 + b_{kj}^2 + 2a_{kj}b_{kj} \cos \alpha_{jk} + c_{kj}^2 \sin^2 \alpha_{jk} \,, \tag{33}$$

with α_{jk} being the angle between the two cone axes,

$$\alpha_{jk} = \cos^{-1}(\boldsymbol{n}_j \cdot \boldsymbol{n}_k) \,. \tag{34}$$

Solving Eqs. (31) and (32) gives the coefficients

$$(a_{kj}, b_{kj}) = (a_{kj}, a_{jk}) = \csc^2 \alpha_{jk} (C_{kj}, C_{jk}), \tag{35}$$

after adopting the definition

$$C_{kj} = \cos \alpha_j - \cos \alpha_k \cos \alpha_{jk}. \tag{36}$$

Therefore,

$$\boldsymbol{u} = \boldsymbol{w}_{kj} + c_{kj}(\boldsymbol{n}_j \times \boldsymbol{n}_k), \tag{37}$$

where

$$\boldsymbol{w}_{kj} = \csc^2 \alpha_{jk}(C_{kj}\boldsymbol{n}_j + C_{jk}\boldsymbol{n}_k) \,. \tag{38}$$

The normalization condition on $\boldsymbol{u}$ provides

$$c_{kj} = \pm \csc \alpha_{jk} \sqrt{1 - \boldsymbol{w}_{kj} \cdot \boldsymbol{w}_{kj}} \,, \tag{39}$$

and after algebraic reduction of the quantity $\boldsymbol{w}_{kj} \cdot \boldsymbol{w}_{kj}$, we obtain

$$\boldsymbol{u} = \csc^2 \alpha_{jk} \left[C_{kj} \boldsymbol{n}_j + C_{jk} \boldsymbol{n}_k \pm D_{jk} (\boldsymbol{n}_j \times \boldsymbol{n}_k) \right]. \tag{40}$$

In Eq. (40)

$$D_{jk} = D_{kj} = \sqrt{1 - \cos^2 \alpha_{jk} - \cos^2 \alpha_j - \cos^2 \alpha_k + 2 \cos \alpha_j \cos \alpha_k \cos \alpha_{jk}} \tag{41}$$

is the volume of the parallelepiped formed by the vectors $\boldsymbol{n}_j$, $\boldsymbol{n}_k$, and $\boldsymbol{u}$. If $\left| \boldsymbol{w}_{kj} \right| > 1$ then no

solution exists for $\boldsymbol{u}$. If $\left| \boldsymbol{w}_{kj} \right| = 1$ then the arcs just touch on the unit sphere and intersect at a

single point $\boldsymbol{w}_{kj}$. Otherwise, two intersection points occur.

From the points of intersection, we need to compute the azimuthal angles $\Delta \phi_k$ for each

cone, as depicted in Fig. 3.3. For a cone with angle α_k directed along the z axis, the parametric

equation for the circle of intersection with the unit sphere is

$$\tilde{\boldsymbol{u}}(\phi) = (\sin \alpha_k \cos \phi \,, \sin \alpha_k \sin \phi \,, \cos \alpha_k) = \mathbf{D}(\alpha_k) \boldsymbol{q}(\phi), \tag{42}$$

where $\boldsymbol{q}(\phi) = (\cos \phi, \ \sin \phi, \ 1)$ and $\mathbf{D}(\alpha_k)$ is a diagonal matrix with elements $(\sin \alpha_k, \ \sin \alpha_k,$

$\cos \alpha_k)$. For a general axis $\boldsymbol{n}_k$, whose polar and azimuthal angles are (θ_k, λ_k), the coordinates of

Eq. (42) can be rotated using the customary direction cosine matrix $\boldsymbol{\Phi}$.[33] In particular,

$$\boldsymbol{u}(\phi) = \boldsymbol{\Phi}^{\mathrm{T}}\!\left(\theta_k, \lambda_k, 0\right) \mathbf{D}\!\left(\alpha_k\right) \boldsymbol{q}(\phi) \,, \tag{43}$$

where the third Euler angle for the rotation has been set to 0 for convenience. The $\boldsymbol{\Phi}^{\mathrm{T}}$ matrix in

Eq. (43) has columns composed of the unit vectors in Eqs. (13)–(15),

$$\boldsymbol{\Phi}^{\mathrm{T}}\!\left(\theta_k, \lambda_k, 0\right) = \left[\ \boldsymbol{e}_2\!\left(\theta_k, \lambda_k\right)\ \ \boldsymbol{e}_3\!\left(\lambda_k\right)\ \ \boldsymbol{e}_1\!\left(\theta_k, \lambda_k\right)\ \right]. \tag{44}$$

The reference axis for measuring the local azimuthal angle ϕ lies in the plane formed by the cone axis $\boldsymbol{n}_k$ and the z axis of the Cartesian coordinate system. By inverting Eq. (43) we obtain

$$q(\phi) = \mathbf{D}^{-1}(\alpha_k)\boldsymbol{\Phi}(\theta_k,\lambda_k,0)u(\phi) , \tag{45}$$

which yields

$$\cos\phi = \csc\alpha_k\,\boldsymbol{u}\cdot\boldsymbol{e}_2(\theta_k,\lambda_k) , \tag{46}$$

and

$$\sin\phi = \csc\alpha_k\,\boldsymbol{u}\cdot\boldsymbol{e}_3(\lambda_k) . \tag{47}$$

To evaluate the dot products on the right side of Eqs. (46) and (47) by means of Eq. (40), first recognize that $\boldsymbol{n}_j = \boldsymbol{e}_1(\theta_j,\lambda_j)$ and $\boldsymbol{n}_k = \boldsymbol{e}_1(\theta_k,\lambda_k)$, and then determine that

$$\boldsymbol{n}_j \times \boldsymbol{n}_k = \sin\theta_j\sin(\lambda_j-\lambda_k)\,\boldsymbol{e}_2(\theta_k,\lambda_k)$$
$$+\left[\sin\theta_k\cos\theta_j - \sin\theta_j\cos\theta_k\cos(\lambda_j-\lambda_k)\right]\boldsymbol{e}_3(\lambda_k) . \tag{48}$$

With the aid of Table 3.3, Eqs. (40), (46), and (47) provide the key results

$$\sin\phi_{k,j} = \csc\alpha_k\csc^2\alpha_{jk}\left\{\begin{array}{c}C_{kj}\sin\theta_j\sin(\lambda_j-\lambda_k)\\ \pm D_{kj}\left[\sin\theta_k\cos\theta_j - \sin\theta_j\cos\theta_k\cos(\lambda_j-\lambda_k)\right]\end{array}\right\} \tag{49}$$

and

$$\cos\phi_{k,j} = \csc\alpha_k\csc^2\alpha_{jk}\left\{\begin{array}{c}C_{kj}\left[\sin\theta_j\cos\theta_k\cos(\lambda_j-\lambda_k) - \cos\theta_j\sin\theta_k\right]\\ \pm D_{kj}\sin\theta_j\sin(\lambda_j-\lambda_k)\end{array}\right\}, \tag{50}$$

where $\phi_{k,j}$ denotes the local azimuthal angle on cone k for an intersection point with cone j.

Table 3.3. Matrix Elements of $\mathbf{F} = \Phi\left(\theta_j, \lambda_j\right)\Phi^{\mathrm{T}}\left(\theta_k, \lambda_k\right) = \Phi_j\Phi_k^{\mathrm{T}}$

$F_{IJ}(\theta_j, \theta_k, \lambda_j - \lambda_k) = e_I(\theta_j, \lambda_j) \cdot e_J(\theta_k, \lambda_k)$	$F_{JI}(\theta_j, \theta_k, \lambda_j - \lambda_k) = F_{IJ}(\theta_k, \theta_j, \lambda_k - \lambda_j)$
$F_{11} = \sin\theta_j \sin\theta_k \cos(\lambda_j - \lambda_k) + \cos\theta_j \cos\theta_k$	$F_{21} = \sin\theta_k \sin\theta_j \cos(\lambda_j - \lambda_k) - \sin\theta_j \cos\theta_k$
$F_{22} = \sin\theta_j \sin\theta_k + \cos\theta_j \cos\theta_k \cos(\lambda_j - \lambda_k)$	$F_{31} = -\sin\theta_k \sin(\lambda_j - \lambda_k)$
$F_{33} = \cos(\lambda_j - \lambda_k)$	$F_{32} = -\cos\theta_k \sin(\lambda_j - \lambda_k)$

In general, Eqs. (49) and (50) must be applied at all intersection points for each cone to determine the azimuthal intervals defining the candidate boundary arcs for the solid angle computation. Among the ligands reported here, the number of arcs for a single cone ranges as high as 34 [d(*t*-Bu)pp and xantphos].

To ascertain the turn angle $\tau_{k,j}$ occurring when an arc on cone k intersects with an arc on cone j, Eq. (43) can be differentiated to give the required tangent vector formula

$$v(\phi) = u'(\phi) = \Phi_k^{\mathrm{T}} \mathbf{D}_k e_3(\phi) \,, \tag{51}$$

which employs the shorthand notation $\Phi_k = \Phi\left(\theta_k, \lambda_k\right)$ and $\mathbf{D}_k = \mathbf{D}(\alpha_k)$. Because $\mathbf{D}_k\Phi_k\Phi_k^{\mathrm{T}}\mathbf{D}_k = \mathbf{D}_k^2$ due to the unitarity of Φ_k, the norm of the tangent vector v_k for cone k must be $\sin\alpha_k$. The cosine of the turn angle is equal to the dot product of the normalized tangent vectors for cones k and j. Accordingly, Eq. (51) yields

$$\cos\tau_{k,j} = \frac{v_k \cdot v_j}{|v_k||v_j|} = \csc\alpha_j \csc\alpha_k e_{3,j}^{\mathrm{T}} \mathbf{D}_j\Phi_j\Phi_k^{\mathrm{T}}\mathbf{D}_k e_{3,k} \,. \tag{52}$$

Defining the matrix elements $F_{IJ}(\theta_j, \theta_k, \lambda_j - \lambda_k)$ as in Table 3.3, Eq. (52) simplifies to

$$\cos\tau_{k,j} = \begin{pmatrix} -\sin\phi_{j,k} & \cos\phi_{j,k} & 0 \end{pmatrix}\begin{pmatrix} F_{22} & F_{23} & F_{21} \\ F_{32} & F_{33} & F_{31} \\ F_{12} & F_{13} & F_{11} \end{pmatrix}\begin{pmatrix} -\sin\phi_{k,j} \\ \cos\phi_{k,j} \\ 0 \end{pmatrix}, \tag{53}$$

or

$$\cos \tau_{k,j} = F_{33} \cos \phi_{j,k} \cos \phi_{k,j} + F_{22} \sin \phi_{j,k} \sin \phi_{k,j}$$

$$-F_{32} \cos \phi_{j,k} \sin \phi_{k,j} - F_{23} \sin \phi_{j,k} \cos \phi_{k,j} . \qquad (54)$$

The trigonometric functions of $\phi_{j,k}$ and $\phi_{k,j}$ appearing in Eq. (54) can be written in shorthand

versions of Eqs. (49) and (50) as

$$\sin \phi_{j,k} = \csc \alpha_j \csc^2 \alpha_{jk} \left(F_{31} C_{jk} \pm F_{21} D_{jk} \right)$$

$$\sin \phi_{k,j} = \csc \alpha_j \csc^2 \alpha_{jk} \left(F_{13} C_{kj} \mp F_{21} D_{kj} \right)$$

$$\cos \phi_{j,k} = \csc \alpha_j \csc^2 \alpha_{jk} \left(F_{21} C_{jk} \mp F_{31} D_{jk} \right)$$

$$\cos \phi_{k,j} = \csc \alpha_j \csc^2 \alpha_{jk} \left(F_{12} C_{kj} - F_{13} D_{kj} \right). \qquad (55)$$

Equation (55) reflects the need to switch the choice of signs for the roots when interchanging j, k

in order to match intersection points on the two cones.

Placing Eqs. (55) into Eq. (54), followed by a tedious collection of terms, provides

$$\sin \alpha_j \sin \alpha_k \sin^4 \alpha_{jk} \cos \tau_{k,j} = C_{jk} C_{kj} \left[F_{21} \left(\boldsymbol{F}^{(1)} \times \boldsymbol{F}^{(3)} \right)_1 + F_{31} \left(\boldsymbol{F}^{(2)} \times \boldsymbol{F}^{(1)} \right)_1 \right]$$
$$\mp C_{jk} D_{kj} \left[F_{31} \left(\boldsymbol{F}^{(2)} \cdot \boldsymbol{F}^{(1)} \right) - F_{21} \left(\boldsymbol{F}^{(3)} \cdot \boldsymbol{F}^{(1)} \right) \right] \mp D_{jk} D_{kj} \left[F_{12} \left(\boldsymbol{F}_{(3)} \cdot \boldsymbol{F}_{(1)} \right) - F_{13} \left(\boldsymbol{F}_{(2)} \cdot \boldsymbol{F}_{(1)} \right) \right] \qquad (56)$$
$$- D_{jk} D_{kj} \left[F_{21} \left(\boldsymbol{F}^{(2)} \cdot \boldsymbol{F}^{(1)} \right) + F_{31} \left(\boldsymbol{F}^{(3)} \cdot \boldsymbol{F}^{(1)} \right) - F_{11} \left(F_{21}^2 + F_{31}^2 \right) \right]$$
.

In Eq. (56), $\boldsymbol{F}^{(J)} = (F_{J1}, F_{J2}, F_{J3})$ and $\boldsymbol{F}_{(J)} = (F_{1J}, F_{2J}, F_{3J})$ signify the Jth row and column of the

F_{IJ} matrix, respectively, and the subscript 1 outside the parentheses in the first term denotes the

first element of the cross product vector. Because the F_{IJ} matrix results from a product of unitary

matrices $\boldsymbol{\Phi}_j$ and $\boldsymbol{\Phi}_k^{\mathrm{T}}$, it also is unitary, having rows and columns that are mutually orthogonal.

Therefore, Eq. (56) simplifies considerably, a manifestation of the independence of each turn

angle to collective rotations of the cone axes. Specifically,

$$\sin \alpha_j \sin \alpha_k \sin^4 \alpha_{jk} \cos \tau_{k,j} = \left(F_{21}^2 + F_{31}^2 \right) \left(D_{jk} D_{kj} F_{11} - C_{jk} C_{kj} \right). \qquad (57)$$

From the definitions in Table 3.3, $F_{11} = \cos\alpha_{jk}$, and thus $F_{21}^2 + F_{31}^2 = 1 - F_{11}^2 = \sin^2\alpha_{jk}$, yielding a penultimate equation for the turn angle

$$\cos\tau_{k,j} = \csc\alpha_j \csc\alpha_k \csc^2\alpha_{jk} \left(D_{jk}D_{kj}\cos\alpha_{jk} - C_{jk}C_{kj}\right). \qquad (58)$$

Insertion of Eqs. (36) and (41) into Eq. (58) with algebraic reduction produces a remarkably simple and completely general formula for the turn angles,

$$\cos\tau_{k,j} = \csc\alpha_j \csc\alpha_k \left(\csc\alpha_{jk} - \csc\alpha_j \csc\alpha_k\right). \qquad (59)$$

If Eq. (59) is used to eliminate $\cos\alpha_{jk}$ from Eq. (41), another useful relationship is found,

$$\sin\tau_{k,j} = \csc\alpha_j \csc\alpha_k D_{kj}. \qquad (60)$$

In summary, elegant analytic formulas [Eqs. (49), (50), (59), and (60)] have been derived for all quantities required to compute exact solid angles of ligands by means of our line integral formalism [Eq. (29)].

Computational Methods

Equilibrium geometric structures for all complexes were optimized using the B3LYP[34,35] density functional with a radial, angular (75, 302) grid by means of the QChem3.2 package.[36] All electronic structure computations employed the Pople basis set 6-31G* for first-row[37] and second-row[38] atoms, and a basis set with the Los Alamos effective core potential, LANL2DZ, for transition metals and halogens.[39] Vibrational frequencies were computed at the same level of theory to confirm that all complexes were in fact minima on the potential energy surface. To test geometric variances with respect to theoretical method, a comparison is presented in Table 3.4 of solid cone angles for a set of ten monodentate Pd-bound ligands and two bidentate ligands optimized by the B3LYP-D3, M06, B97, M05-2X, and PBE functionals. The mean absolute difference of the $\Theta°$ values of the monodentate ligands for these five functionals compared to the

B3LYP value is 0.6°, 0.9°, 0.3°, 1.4°, and 1.7°, respectively. For the two bidentate ligands, dmpe and bpy, the same mean absolute deviation for all five alternative functionals was 1.4° with a standard deviation of 1.9°. These small differences indicate that dependence of the solid angle on the density functional is insignificant in the applications reported here.

Table 3.4. Effect of Density Functional on the Exact Solid Cone Angle ($\Theta°$, deg)

Ligand	B3LYP	B3LYP −D3	δ	M06	δ	B97	δ	M05 −2X	δ	PBE	δ
PMe_3	114.3	114.5	+0.2	113.3	−1.0	114.5	+0.2	112.9	−1.4	113.3	−1.0
PEt_3 (min)	119.0	118.7	−0.3	118.2	−0.8	119.2	+0.2	118.3	−0.7	118.3	−0.7
PEt_3 (max)	133.6	134.0	+0.4	133.2	−0.4	133.6	+0.0	134.5	+0.9	131.9	−1.7
$P(n-Bu)_3$ (min)	119.1	119.2	+0.1	118.1	−1.0	119.3	+0.2	117.4	−1.7	118.4	−0.7
$P(n-Bu)_3$ (max)	134.6	135.9	+1.3	135.0	+0.4	135.2	+0.6	136.6	+2.0	133.4	−1.2
$P(i-Bu)_3$	174.5	176.5	+2.0	176.6	+2.1	175.1	+0.6	178.0	+3.5	169.1	−5.4
$P(i-Pr)_3$ (min)	138.7	139.2	+0.5	138.0	−0.7	139.2	+0.5	137.8	−0.9	138.0	−0.7
$P(i-Pr)_3$ (max)	150.4	150.9	+0.5	150.2	−0.2	150.7	+0.3	151.0	+0.6	148.6	−1.8
$P(t-Bu)_3$	160.8	160.4	−0.4	160.2	−0.6	161.3	+0.5	160.3	−0.5	159.1	−1.7
PPh_3	135.7	135.9	+0.2	133.6	−2.1	135.7	+0.0	133.9	−1.8	133.9	−1.8
dmpe	156.1	156.1	+0.0	155.8	−0.3	156.8	+0.7	156.5	+0.4	152.9	−3.2
bpy	133.8	133.7	−0.1	131.9	−1.9	134.4	+0.6	128.7	−5.1	131.8	−2.0

A *Mathematica*[40] package FindSolidAngle was written to compute $\Omega°$ and $\Theta°$ parameters and visualize the solutions, with minimal computational time required for any given input structure. The program is freely available at http://www.ccqc.uga.edu/references/software.php. Sticking with convention, here we report solid angles derived from the van der Waals atomic radii of Bondi, r = (1.80, 1.20, 1.70, 1.55, 1.52, 1.47, 1.80, 1.75, 2.00) Å for (P, H, C, N, O, F, S, Cl, Fe), respectively.[41] Previous reports have criticized the use of such van der Waals radii to quantify steric demands and have proposed zero energy point radii (r_Z) as alternatives.[22] While this issue warrants further study, the focus of this paper is to demonstrate our analytic $\Omega°$ method and not to argue for a particular choice of atomic radii or promote a canonical set of steric

parameters. With a database of optimized Cartesian structures, our FindSolidAngle program can be used to quickly generate results with any set of the atomic radii chosen in future work. The ligand solid angle is highly dependent on the choice of atomic radii; however, our analytic procedure applied with r_Z atomic radii, instead of the Bondi radii, yields solid angles in close agreement with the corresponding numerical values we computed with the Solid-G program.[22]

More exhaustive checks of our analytic formulas for solid angle integration were executed by means of independent numerical integrations of the surface area of ligand shadows. A 5810-point Lebedev grid was utilized for this purpose.[42] Each point in the Lebedev grid was tested to ascertain whether it lay inside the shadow of any ligand atom.[17] The fraction of such occluded points multiplied by 4π then gives an estimate of the solid angle of the entire ligand shadow. While inefficient, this Lebedev integration scheme provides a simple, direct check of the analytic equations. For all complexes investigated in this study, the accuracy of the analytic formulas was confirmed to within the numerical error of the Lebedev integration (≈ 0.01 str).

Results and Discussion

An extensive collection of data for monodentate phosphine and amine ligands bound to group 10 metals (Ni, Pd, and Pt) is presented in Table 3.5. Although zerovalent group 10 metals rarely have a single ligand, our complexes were computationally optimized as such to provide reference data devoid of steric effects from neighboring ligands. Ligands with multiple conformations exhibit a range of steric values.[17] The minimum (min) and maximum (max) $\Theta°$ values for the various conformers are given in separate columns. The Pd(PBz$_3$) and Ni(PBz$_3$) cases demonstrate that the min and max $\Theta°$ values can differ by 36° or more. In crowded environments the min conformation is usually more applicable; however, in uncrowded systems the max conformation is preferred, because the corresponding conformation is of lower energy in

almost all cases studied.[17] However, conformations where one arm is min while another is max are certainly possible, but not explored here. The dependence of $\Theta°$ on conformation and the possibility of meshing among ligands show that universal values of steric parameters are inadequate and that solid angles should be computed for specific environments.

The steric encumbrance of a given ligand follows the general trend Ni > Pt > Pd as the central metal atom is varied, consistent with the increasing radius of the metal center (the further away the ligand, the less shielding). Solid cone angles do not always increase in proportion to substituent size, as a consequence of overlapping shadow cones. For example, the $PdPMe_3$, $PdPEt_3$, and $PdP(n\text{-}Bu)_3$ complexes exhibit $\Theta° = 114.3°$, $119.0°$, and $119.1°$, respectively, as the length of the substituent alkyl chain increases.

Crowded environments introduce intramolecular interactions between adjacent ligands that frustrate rotation,[43] in which case visualization of individual solid angles is helpful in assessing meshing ability. Pseudo-C_3 symmetry is generally evident in the indentations of the ligand shadows, though this may change with the addition of adjacent ligands. Two cases showing particularly pronounced indentations and meshing possibilities are the $P(i\text{-}Bu)_3$ and NBz_3 ligands.

Compiled in Table 3.6 are computed $\Theta°$ for a variety of platinum-bound bidentate ligands whose structures and abbreviations are shown in Chart 3.1. These structures are quite rigid, as rotation about either bond is prevented by the high denticity. The computed $\Theta°$ are close to the crystallographic values for Pt complexes,[21] with a MAD of 7.2° and standard deviation of 7.0°. Computing $\Theta°$ for specific complexes rather than assigning a universal value creates a flexible description of steric properties for direct study of solid angle dependence on ligand environment.

Table 3.5. Computed Exact Solid Cone Angles ($\Theta°$) vs. Average Crystallographic Values (Θ)[19] for Monodentate Ligands

Ligand	Θ	$\Theta°$(Pd)		$\Theta°$(Ni)		$\Theta°$(Pt)	
		Min	Max	Min	Max	Min	Max
PMe$_3$	124	114.3	–	124.3	–	119.2	–
PEt$_3$	143	119.0	133.6	128.1	142.0	123.6	136.7
P(n-Bu)$_3$	148	119.1	134.6	127.9	143.0	123.5	138.2
P(i-Bu)$_3$	173	a	174.5	a	184.5	a	176.9
P(i-Pr)$_3$	163	138.7	150.4	146.2	156.7	142.9	154.2
P(t-Bu)$_3$	182	160.8	–	168.3	–	164.7	–
PMe$_2$Et	133	115.7	120.7	125.1	129.7	120.4	125.3
PMe$_2$(i-Pr)	140	122.9	–	131.5	–	127.0	–
PMe$_2$(t-Bu)	144	129.0	–	136.9	–	133.0	–
PMeEt$_2$	138	117.3	126.8	126.4	135.5	122.0	130.7
PEt$_2$(i-Pr)	150	125.5	140.6	134.0	148.8	130.0	144.6
PEt$_2$(t-Bu)	156	133.2	143.8	141.3	148.9	137.4	145.0
PMe(i-Pr)$_2$	151	134.2	137.8	142.8	145.3	134.2	141.6
PEt(i-Pr)$_2$	156	137.5	145.7	146.5	153.2	141.5	149.9
P(i-Pr)$_2$(t-Bu)	170	152.0	153.2	160.3	160.3	151.2	157.0
PMe(t-Bu)$_2$	163	144.7	–	152.2	–	148.8	–
PEt(t-Bu)$_2$	161	147.8	150.5	155.2	157.5	151.7	154.3
P(i-Pr)(t-Bu)$_2$	178	154.3	156.1	161.8	163.3	158.3	160.1
PPh$_3$	129	135.7	–	146.0	–	140.6	–
P(p-ClPh)$_3$	129	135.8	–	146.2	–	140.7	–
P(m-MePh)$_3$	140	135.7	138.8	145.8	148.1	139.7	142.7
P(m-ClPh)$_3$	136	135.6	137.3	146.2	147.3	140.5	141.7
P(p-MePh)$_3$	135	135.9	–	146.0	–	140.4	–
P(p-OMePh)$_3$	139	135.8	136.1	145.9	146.2	140.2	140.7
P(p-FPh)$_3$	129	136.0	–	146.3	–	140.7	–
P(m-(t-Bu)Ph)$_3$	159	135.4	154.2	145.3	162.8	140.0	157.7
P(o-MePh)$_3$	142	141.9	159.9	151.7	169.8	146.4	162.0
PPh$_2$H	112	125.3	–	137.3	–	126.1	–
PPh$_2$Me	124	128.7	–	139.1	–	133.4	–
PPh$_2$Et	140	127.4	135.8	135.5	145.4	131.5	140.2
PPh$_2$(n-Bu)	140	127.3	136.7	135.5	146.0	131.6	140.5
PPh$_2$(i-Bu)	148	129.3	150.8	137.3	160.8	133.4	154.7
PPh$_2$(i-Pr)	139	135.4	142.2	143.3	151.2	139.0	146.8
PPh$_2$Bz	139	129.9	145.8	138.4	155.3	134.6	148.5
PPh$_2$(t-Bu)	149	141.4	–	148.6	–	145.2	–
PPh$_2$Cl	117	129.2	–	141.1	–	133.5	–
PPhMe$_2$	126	123.1	–	132.7	–	127.9	–
PPhEt$_2$	137	127.7	135.3	136.5	144.0	132.2	139.1
PPh(n-Bu)$_2$	154	121.9	136.0	130.3	144.2	126.0	140.2
PPh(t-Bu)$_2$	168	155.2	–	163.2	–	159.3	–
PBz$_3$	163	123.0	159.3	131.5	167.7	127.5	158.9
NH$_3$	87	93.8	–	112.0	–	101.9	–
NMe$_3$	124	120.5	–	131.8	–	126.4	–
NEt$_3$	142	125.9	148.3	138.6	154.3	132.3	148.0
N(i-Pr)$_3$	161	152.1	166.1	165.6	176.4	157.7	168.5
NBz$_3$	173	129.9	156.1	143.2	181.2	137.2	170.6

[a]Structure is not a minimum on the potential energy surface. For Cartesian coordinates of all complexes see ref 17.

Chart 3.1. Structures and Abbreviations of Bidentate Ligands and Multidentate Complexes
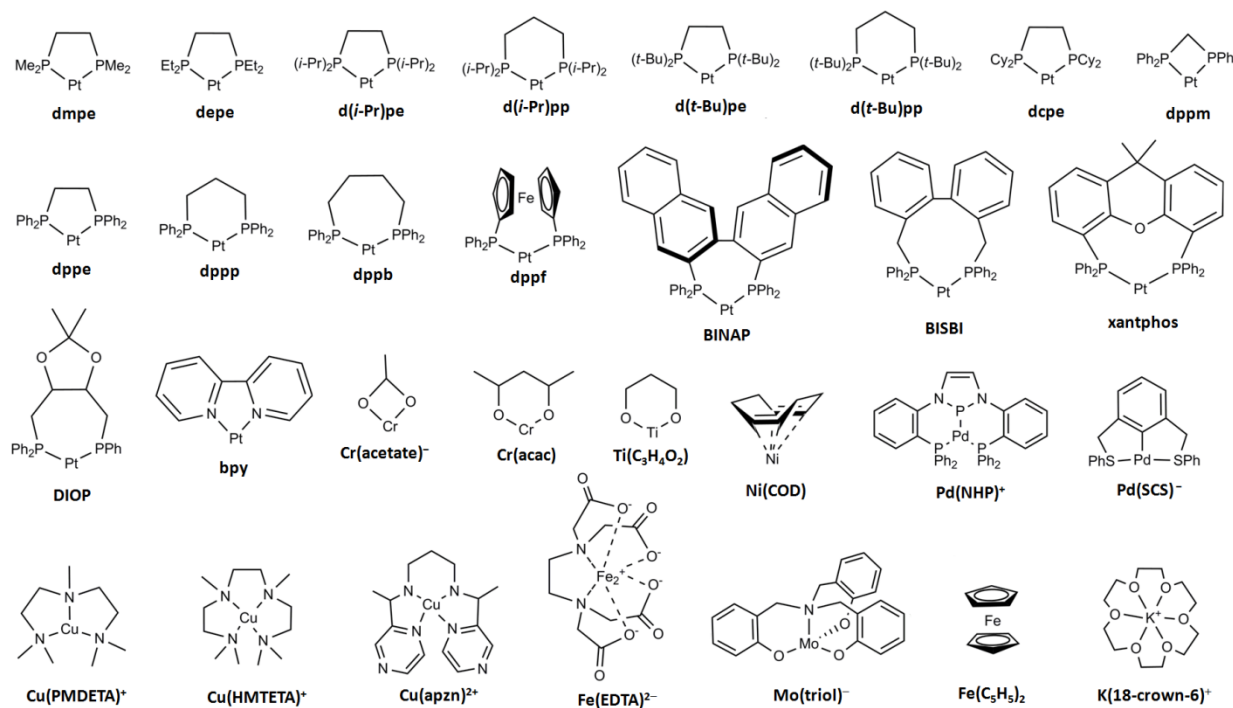
Guzei and Wendt[22] have advocated use of an easily interpretable G-parameter that describes ligand shielding as a simple percentage of the maximum solid angle of 4π steradians, specifically, $G = 100\frac{\Omega}{4\pi}$. This percentage indicates the remaining open area of a complex where an incoming reagent could bind. Values of G^T computed from our optimized theoretical (T) structures of platinum complexes are also listed in Table 3.6.

The $\Omega°$ parameters in Table 3.6 show that the commonly used bite angle ($\angle$ D–M–D) is not an adequate descriptor of ligand sterics. Although a set of phosphine ligands may have the same backbone, the total steric encumbrance from phosphorus side groups can vary dramatically. For instance, methyl side groups (dmpe) provide $\Omega° = 5.27$ str ($G^T = 41.9\%$), which increases to 6.32 str ($G^T = 50.3\%$) when replaced by phenyl rings (dppe). In stark contrast, dppe has a 0.5° *smaller* bite angle than dmpe.

Table 3.6. Steric Parameters of Bidentate Ligands Bound to Platinum[a]

Ligand	∠D–M–D (°)	$\Theta(°)$[b]	$\Omega°$(str)	$\Theta°(°)$	G^T(%)
dmpe	100.8	156	5.27	161.4	41.9
depe	100.9	176	5.66	168.6	45.0
d(*i*-Pr)pe	102.0	188	6.96	192.3	55.4
d(*i*-Pr)pp	117.6	193	7.42	200.9	59.0
d(*t*-Bu)pe	103.2	202	7.63	204.7	60.7
d(*t*-Bu)pp	119.8	210	8.22	215.9	65.4
dcpe	101.7	191	7.03	193.6	55.9
dppm	81.8	168	5.60	167.4	44.6
dppe	100.3	178	6.32	180.7	50.3
dppp	113.3	183	6.85	190.4	54.5
dppb	138.6	188	7.47	201.8	59.4
dppf	133.3	192	7.63	204.8	60.7
BINAP	123.1	−	7.36	199.7	58.6
BISBI	155.7	−	8.25	216.4	65.7
xantphos	146.2	192	8.04	212.5	64.0
DIOP	137.4	−	7.30	198.6	59.1
bpy	80.2	−	4.09	139.1	32.5

[a] Calculated from B3LYP structures using the Bondi atomic radii.
[b] Solid cone angles compiled from crystal structures of platinum complexes.[21]

Table 3.7 gives the computed exact solid angles and theoretical G-parameters for a set of multidentate complexes in Chart 3.1. As an example of how readily our $\Omega°$ formulation handles a highly crowded complex, $Fe(EDTA)^{2-}$ was considered. The EDTA ligand, which has a denticity of six, has $\Omega° = 10.34$, occluding 82.3% of the total unit sphere. The multitude of overlap regions, shown in Figure 3.4, would be difficult to account for using direct solid-angle integration and subtraction schemes. However, the perimeter of the ligand shadow is defined solely by four carbonyl oxygen atoms, and only four arcs are needed to evaluate the line integral for $\Omega°$. The corresponding azimuthal angle intervals are $\Delta\phi = (98.0°, 154.5°, 98.0°, 154.6°)$ and the vertex turn angles are $\tau = (140.1°, 134.0°, 140.2°, 134.0°)$.

Table 3.7. Solid Angles and G-parameters for Multidentate Ligands Corresponding to Chart 3.1

Complex	$\Omega°$(str)	G^T(%)	Complex	$\Omega°$(str)	G^T(%)
Cr(acetate)$^-$	4.32	34.4	Cu(PMDETA)$^+$	8.27	65.8
Cr(acac)	5.61	44.6	Cu(apzn)$^{2+}$	8.45	67.2
Ti(C$_3$H$_4$O$_2$)	5.72	45.5	Pd(NHP)+	8.78	69.9
K(18-crown-6)$^+$	7.22	57.5	Mo(triol)$^-$	9.64	76.7
Ni(COD)	7.53	59.9	Cu(HMTETA)$^+$	10.22	81.3
Pd(SCS)$^-$	7.82	62.2	Fe(EDTA)$^{2-}$	10.34	82.3
Fe(C$_5$H$_5$)$_2$	12.08	96.1			
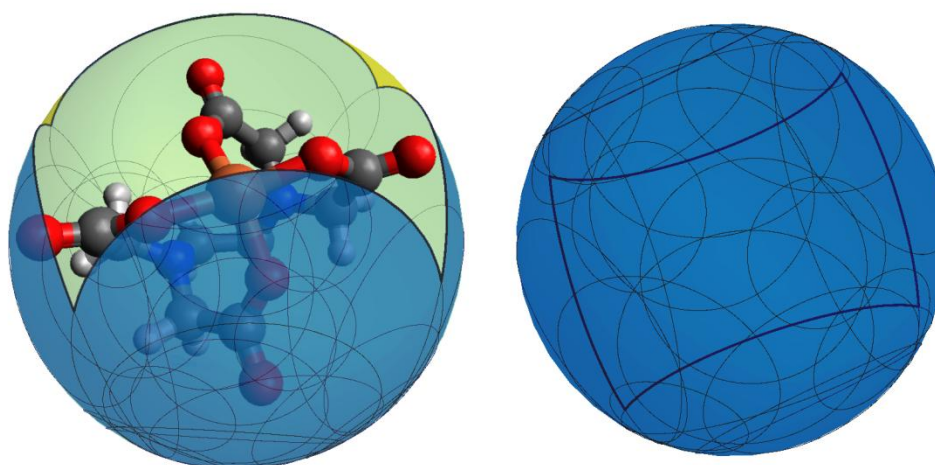
Figure 3.4. The solid angle (blue) of Fe(EDTA)$^{2-}$ showing the encapsulated ligand (left) and overlap areas (right).

Ligand shadow plots on the unit sphere show gaps in steric coverage that are not accounted for by the Tolman cone angle. For a freely rotating ligand, these gaps may not be relevant, but in a rigid system these gaps can facilitate ligand meshing and should be considered by the steric descriptor. As an example, most of the steric coverage in Pt[1,2-bis (diethylylphosphino)ethane] (depe) comes from the phenyl groups on the phosphorus donors, and not from the ligand backbone. Consequently, there are deep indentations in the shadow of the depe ligand (Figure 3.5), whose overall solid angle is 5.66 str, covering 45.0% of the metal

center. Because such gaps may not be chemically relevant if they are small. our FindSolidAngle program allows the user to "plug the gap" manually by placing a dummy atom between two arcs that delineate the gap. As an example, plugging one of the gaps in the Pt(depe) complex gives a solid angle of 6.60 str (G^T = 52.5%), showing that this gap comprises roughly 7.5% of the sphere encompassing the Pd atom.

For the depe ligand, the Tolman bidentate approximation gives a cone angle $\theta = 115°$,[6] much smaller than either $\Theta°$ (168.6°) or $\theta°$ (221.8°).[17] The Tolman scheme of surrounding the bidentate ligand with two smaller cones centered around each donor atom is thus strikingly deficient for depe. In many cases, the Tolman semi-cone angles are determined by physical space-filling models,[6] which do not reflect distortions from the idealized geometry about the phosphorous atoms. Additionally, ligands with considerably different semi-cone angles are not well described by the averaging scheme, and the largest substituent spills outside the cone of inclusion.
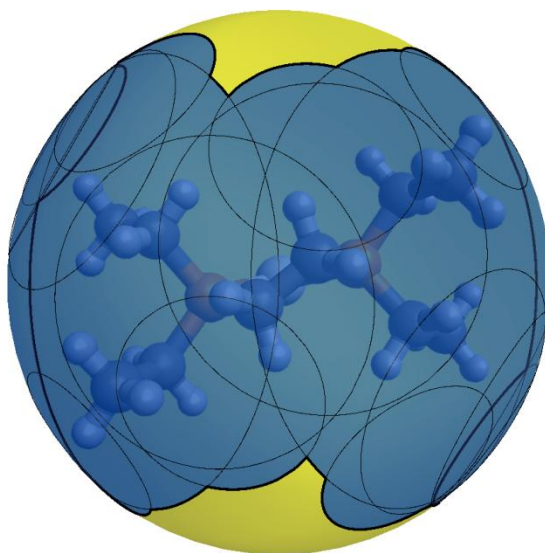
Figure 3.5. The solid angle (blue) of Pt[1,2-bis(diethylphosphino)ethane] (depe).

An interesting situation arises when instead of gaps, there are holes in the ligand shadow, as shown in Figure 3.6 (left panel) for Pt(xantphos). Our exact solid angle method handles this situation without difficulty. The outer perimeter of the Pt(xantphos) profile encloses $\Omega° = 8.06$ str, while the separately reported irregular inner hole comprises $\Omega° = 0.22$ str. Subtracting the latter from the former yields the net solid angle of 7.84 str. However, in this case it is more chemically relevant to include the hole region in the reported solid angle since it is unlikely that any reagent would interact with the metal through such a small area.

Holes can also appear when two separate ligands have overlapping shadows. Ferrocene, a typical metallocene with two η^5-bound cyclopentadienyl ligands bound to an iron center, displays almost complete enclosure of the metal center with a total G^T value of 96.1%. The boundaries of the shadows of the two cyclopentadienyl rings intersect multiple times, producing five small holes in the overall profile of around 0.1 str each. The meshing of the two ferrocenyl units is handled easily by our mathematical formalism without double-counting the overlap area.

When a large gap is present in the ligand shadow, the hole may have chemical consequences. For complexes of crown ethers such as K^+(18-crown-6) depicted in Figure 3.6 (right panel), the ligand forms a belt around the central atom, and two large holes appear in the top and bottom of the solid angle profile, each with exact solid angles of 2.67 str (G^T = 21.4%). Because smaller ligands could potentially access the central potassium atom through either hole, knowing the size of the hole, as well as the size of the incoming ligand, becomes important.
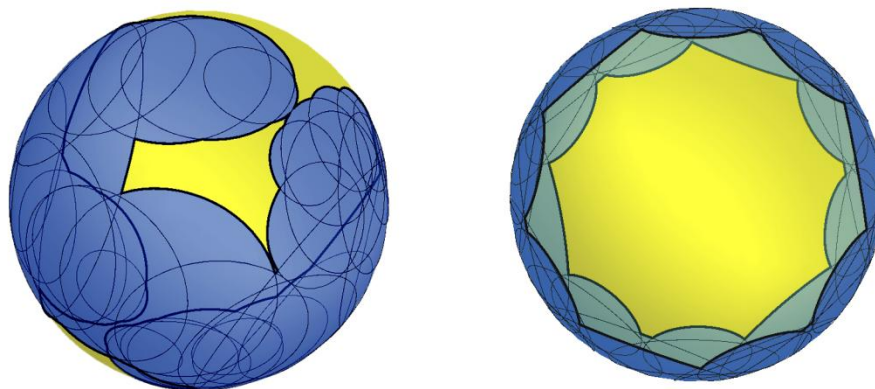
Figure 3.6. A hole in the solid angle (blue) of Pd(xantphos) (left) and K[+](18-crown-6) (right).

The ligand encumbrance, and thus the solid angle, depends on steric environment.[44] For example, chromium can have a maximum of three acetylacetonate (acac) ligands to give a $\Omega°$ of 12.32 str (G^T = 98.0%). Looking at a single acac unit in the $Cr(acac)_3$ structure gives a $\Omega°$ of 4.49 str (G^T = 35.7%) per acac. Thus, in the $Cr(acac)_3$ structure there is about a 9% overlap of the separate units. To study the amount of ligand compression, we computationally optimized chromium with a single acac unit and found a $\Omega°$ of 5.61 str (G^T = 44.6%), which amounts to an 8.9% ligand compression in the full $Cr(acac)_3$ complex. This case highlights the importance of calculating the solid angle for specific complexes rather than using a universal value for each ligand regardless of the environment.

Conclusions

An exact, analytic solution to the ligand solid angle integration problem has been derived and implemented for practical computations. The formulation relies on a line integral around the perimeter of the ligand shadow cast on an encompassing sphere, thus eliminating the need for complicated subtraction schemes to avoid over-counting of overlap regions. The exact solid angle ($\Omega°$) method is a general solution for all geometrical arrangements and is applicable to

entire complexes as well as individual ligands. A freely available program has been developed to calculate exact solid angles from the Cartesian coordinates of a complex, as given by quantum chemical computations, X-ray crystallography, or any other method.

The exact solid angle method was applied comprehensively by using density functional theory to optimize over 275 structures of organometallic compounds involving diverse mono- and multidentate ligands. As a steric descriptor, $\Omega°$ is particularly useful for complexes with frustrated rotation about metal-donor bonds. The $\Omega°$ parameter accounts for gaps in the ligand solid angle profile that can facilitate meshing with adjacent ligands. Such gaps are common in bidentate ligands with alkyl backbones, where donor substituents provide the majority of the steric encumbrance. The $\Omega°$ solid angle approach along with our recently advanced exact cone angle $\theta°$ formalism[17] provides new tools for understanding and predicting steric effects in organometallic chemistry.

References

(1) Kranenburg, M.; van der Burgt, Y. E. M.; Kamer, P. C. J.; van Leeuwen, P. W. N. M.; Goubitz, K.; Fraanje, J. *Organometallics* **1995**, 14, 3081.

(2) Freixa, Z.; van Leeuwen, P. W. N. M. *Dalton Trans.* **2003**, 1890.

(3) Breit, B. *Angew. Chem. Int. Ed.* **2005**, 44, 6816.

(4) Lanni, E. L.; Locke, J. R.; Gleave, C. M.; McNeil, A. J. *Macromolecules* **2011**, 44, 5136.

(5) Schwarzenbach, G. *Helv. Chim. Acta.* **1952**, 35, 2344.

(6) Tolman, C. A. *Chem. Rev.* **1977**, 77, 313.

(7) Immirzi, A.; Musco, A. *Inorg. Chim. Acta* **1977**, 25, L41.

(8) Dierkes, P.; W. N. M. van Leeuwen, P. *J. Chem. Soc., Dalton Trans.* **1999**, 1519.

(9) Culkin, D. A.; Hartwig, J. F. *Organometallics* **2004**, 23, 3398.

(10) van Haaren, R. J.; Goubitz, K.; Fraanje, J.; van Strijdonck, G. P. F.; Oevering, H.; Coussens, B.; Reek, J. N. H.; Kamer, P. C. J.; van Leeuwen, P. W. N. M. *Inorg. Chem.* **2001**, 40, 3363.

(11) Bessel, C. A.; Margarucci, J. A.; Acquaye, J. H.; Rubino, R. S.; Crandall, J.; Jircitano, A. J.; Takeuchi, K. J. *Inorg. Chem.* **1993**, 32, 5779.

(12) Aguila, D.; Escribano, E.; Speed, S.; Talancon, D.; Yerman, L.; Alvarez, S. *Dalton Trans.* **2009**, 6610.

(13) Cordero, B.; Gomez, V.; Platero-Prats, A. E.; Reves, M.; Echeverria, J.; Cremades, E.; Barragan, F.; Alvarez, S. *Dalton Trans.* **2008**, 2832.

(14) Immirzi, A.; Musco, A.; Mann, B. E. *Inorg. Chim. Acta* **1977**, 21, L37.

(15) Tolman, C. A.; Seidel, W. C.; Gosser, L. W. *J. Am. Chem. Soc.* **1974**, 96, 53.

(16) Hudson, R. H. E.; Poee, A. J. *Organometallics* **1995**, 14, 3238.

(17) Bilbrey, J. A.; Kazez, A. H.; Locklin, J.; Allen, W. D. *J. Comp. Chem.* **2013**, 34, 1189.

(18) White, D. P.; Anthony, J. C.; Oyefeso, A. O. *J. Org. Chem.* **1999**, 64, 7707.

(19) Brown, T. L.; Lee, K. J. *Coord. Chem. Rev.* **1993**, 128, 89.

(20) White, D.; Taverner, B. C.; Leach, P. G. L.; Coville, N. J. *J. Comp. Chem.* **1993**, 14, 1042.

(21) Niksch, T.; Görls, H.; Weigand, W. *Eur. J. Inorg. Chem.* **2010**, 2010, 95.

(22) Guzei, I. A.; Wendt, M. *Dalton Trans.* **2006**, 0, 3991.

(23) Taverner, B. C. *J. Comp. Chem.* **1996**, 17, 1612.

(24) Caffery, M. L.; Brown, T. L. *Inorg. Chem.* **1991**, 30, 3907.

(25) Brown, T. L. *Inorg. Chem.* **1992**, 31, 1286.

(26) Fey, N.; Harvey, J. N.; Lloyd-Jones, G. C.; Murray, P.; Orpen, A. G.; Osborne, R.; Purdie, M. *Organometallics* **2008**, 27, 1372.

(27) Hillier, A. C.; Sommer, W. J.; Yong, B. S.; Petersen, J. L.; Cavallo, L.; Nolan, S. P. *Organometallics* **2003**, 22, 4322.

(28) Clavier, H.; Nolan, S. P. *Chem. Commun.* **2010**, 46, 841.

(29) Fischer, R. D.; Li, X.-F. *J. Less-Common Met.* **1985**, 112, 303.

(30) Smith, J. M.; Coville, N. J.; Cook, L. M.; Boeyens, J. C. A. *Organometallics* **2000**, 19, 5273.

(31) Smith, J. M.; Coville, N. J. *Organometallics* **2001**, 20, 1210.

(32) Murray, D. A. *Spherical Trigonometry, for Colleges and Secondary Schools*; Longmans, Green and Co., 1908.

(33) Zare, R. N. *Angular Momentum: Understanding Spatial Aspects in Chemistry and Physics*; Wiley-Interscience, 1988.

(34) Lee, C.; Yang, W.; Parr, R. G. *Phys. Rev. B* **1988**, 37, 785.

(35) Becke, A. D. *J. Chem. Phys.* **1993**, 98, 5648.

(36) Shao, Y.; Fusti-Molnar, L.; Jung, Y.; Kussmann, J.; Ochsenfeld, C.; Brown, S. T.; Gilbert, A. T. B.; Slipchenko, L. V.; Levchenko, S. V.; O'Neill, D. P.; Distasio Jr, R. A.; Lochan, R. C.; Wang, T.; Beran, G. J. O.; Besley, N. A.; Herbert, J. M.; Yeh Lin, C.; Van Voorhis, T.; Hung Chien, S.; Sodt, A.; Steele, R. P.; Rassolov, V. A.; Maslen, P. E.; Korambath, P. P.; Adamson, R. D.; Austin, B.; Baker, J.; Byrd, E. F. C.; Dachsel, H.; Doerksen, R. J.; Dreuw, A.; Dunietz, B. D.; Dutoi, A. D.; Furlani, T. R.; Gwaltney, S. R.; Heyden, A.; Hirata, S.; Hsu, C.-P.; Kedziora, G.; Khalliulin, R. Z.; Klunzinger, P.; Lee, A. M.; Lee, M. S.; Liang, W.; Lotan, I.; Nair, N.; Peters, B.; Proynov, E. I.; Pieniazek, P. A.; Min Rhee, Y.; Ritchie, J.; Rosta, E.; David Sherrill, C.; Simmonett, A. C.; Subotnik, J. E.; Lee Woodcock III, H.; Zhang, W.; Bell, A. T.; Chakraborty, A. K.; Chipman, D. M.; Keil, F. J.; Warshel, A.; Hehre, W. J.; Schaefer III, H. F.; Kong, J.; Krylov, A. I.; Gill, P. M. W.; Head-Gordon, M. *Phys. Chem. Chem. Phys.* **2006**, 8, 3172.

(37) Dill, J. D.; Pople, J. A. *J. Chem. Phys.* **1975**, 62, 2921.

(38) Francl, M. M.; Pietro, W. J.; Hehre, W. J.; Binkley, J. S.; Gordon, M. S.; DeFrees, D. J.; Pople, J. A. *J. Chem. Phys.* **1982**, 77, 3654.

(39) Hay, P. J.; Wadt, W. R. *J. Chem. Phys.* **1985**, 82, 299.

(40) Wolfram Research, Inc., *Mathematica*, Version 8.0, Champaign, IL **2010**.

(41) Bondi, A. *J. Phys. Chem.* **1964**, 68, 441.

(42) Lebedev, V.; Laikov, D. *Dokl. Math.* **1999**, 59, 477.

(43) Fanizzi, F. P.; Lanfranchi, M.; Natile, G.; Tiripicchio, A. *Inorg. Chem.* **1994**, 33, 3331.

(44) White, D.; Coville, N. J. *Adv. Organomet. Chem.* **1994**, 36, 95.

CHAPTER 4

ON THE ROLE OF DISPROPORTIONATION ENERGY IN KUMADA CATALYST-TRANSFER POLYCONDENSATION
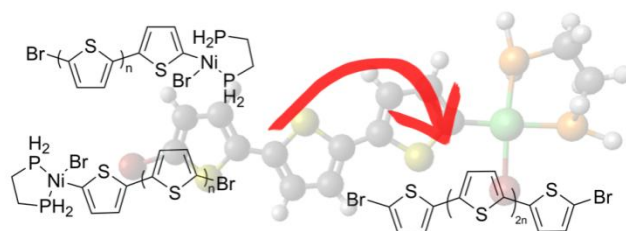
Bilbrey, J. A.; Sontag, S. K.; Huddleston, N. E.; Allen, W. D.; Locklin, J. 2012. *ACS Macro Lett*. 1: 995–1000. Reprinted here with permission of the American Chemical Society.

Abstract

Kumada catalyst-transfer polycondensation (KCTP) is an effective method for the controlled polymerization of conjugated polymers. Nevertheless, side reactions leading to early termination and unwanted chain coupling cause deviations from the target molecular weight, along with increasing dispersity and end group variation. Departure from the KCTP cycle stems from a disproportionation reaction which leads to experimentally observed side products. The disproportionation energies for a series of nickel-based initiators containing bidentate phosphino ancillary ligands were computed using density functional theory at the B3LYP/DZP level. Initiator ligated by 1,3-bis(diphenylphosphino)propane (dppp) was found to be less favorable towards disproportionation than 1,2-bis(diphenylphosphino)ethane (dppe) by 0.5 kcal mol^{-1}. Trends in disproportionation energy with a variety of bidentate phosphine ligands match experimental observations of decreased polymerization control. This value can be used to predict the presence of disproportionation in cross-coupling reactions and, therefore, aid in catalyst design.

Introduction

Kumada catalyst-transfer polycondensation (KCTP) has been shown to undergo a chain-growth polymerization mechanism affording polymers with controlled molecular weight, narrow dispersity (Đ), and uniform chain-ends.[1-3] KCTP, which employs a nickel-based initiating complex, deviates from living polymerization due to premature termination, as evidenced by both high and low molecular weight components in the reaction mixture displaying non-uniform chain-ends.[4, 5] A major contributor to the loss of living character stems from a disproportionation reaction in which two (aryl)Ni(II)-Br complexes exchange ligands, forming an (aryl)$_2$Ni(II) intermediate along with Ni(II)Br$_2$ (Scheme 4.1a). After subsequent reductive elimination and carbon-carbon coupling of the activated complex (**1a**), the nickel(0) remains η-bound to the biaryl product (**2a**) before undergoing intramolecular insertion into the carbon-halogen bond (**2b**) (Scheme 4.1b).[6]

Scheme 4.1. Disproportionation reaction of Ni(dhpe)ThBr.
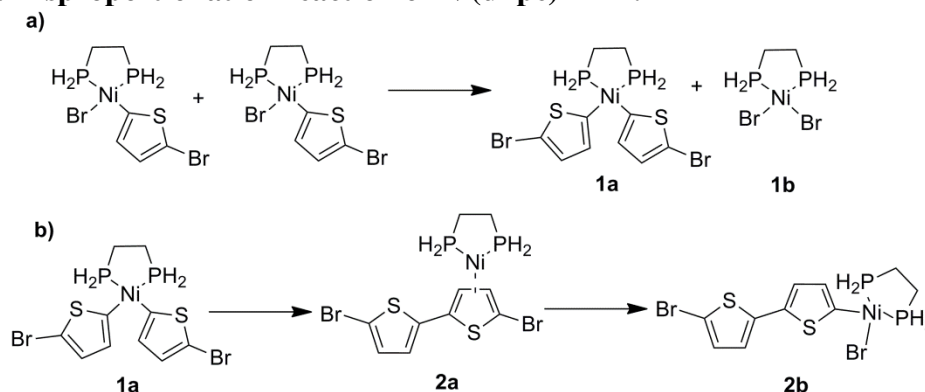
In KCTP, the desired polymerization route involves a Grignard AB-type monomer, which undergoes a repeated cycle of transmetalation (TM), reductive elimination (RE), and oxidative addition (OA) (Scheme 4.2). After the polymerization is quenched by aqueous acid,

resulting chains are of uniform length and contain H/Br end groups. In addition to the ideal cycle, disproportionation can occur whenever an (aryl)Ni(II)Br is present (*i.e.* prior to initiation and transmetalation). During the initiation phase, two initiator complexes can exchange ligands through disproportionation, which releases free $Ni(II)Br_2$ into solution. The $Ni(II)Br_2$ is reactivated by a double transmetalation reaction with excess monomer and taken through a separate KCTP cycle, which results in an increased dispersity due to varying chain lengths. Disproportionation can also occur prior to transmetalation yielding polymers of double molecular weight as well as $Ni(II)Br_2$. The $Ni(II)Br_2$ is released into solution, reactivated, and undergoes another KCTP cycle to further increase dispersity.

The tendency for an initiating complex to disproportionate can be quantified by the disproportionation energy (E_{disp}), which is calculated as the difference between the computed energy of the products and that of the reactants. A positive value represents lower energy in the reactants resulting in a decreased likelihood of disproportionation. Conversely, negative energies correspond to an increased likelihood of disproportionation.

As polymerization characteristics are known to differ according to the choice of ancillary ligand, we have examined a series of commonly employed bidentate phosphino ligands differing in either carbon spacer or phosphorous substituent (Figure 4.1), which influence the bite angle and cone angle of the catalysts.[4,5] In this report, we have observed that the polymerization character is highly influenced by the ability of the initiator to undergo disproportionation, and not trends in either bite angle or cone angle. Deviations in polymerization control can be inferred by the dispersity index (Đ) and resultant end groups. Herein, we match trends in computed disproportionation energies to Đs from several literature reports[4,5] and conclude that loss of polymerization control follows the trend of increased disproportionation.

Scheme 4.2. General scheme for KCTP. Disproportionation is the cause of increased dispersity, resulting in chains with H/Br end groups and coupled-chains with Br/Br end groups. TM = transmetalation, RE = reductive elimination, and OA = oxidative addition.
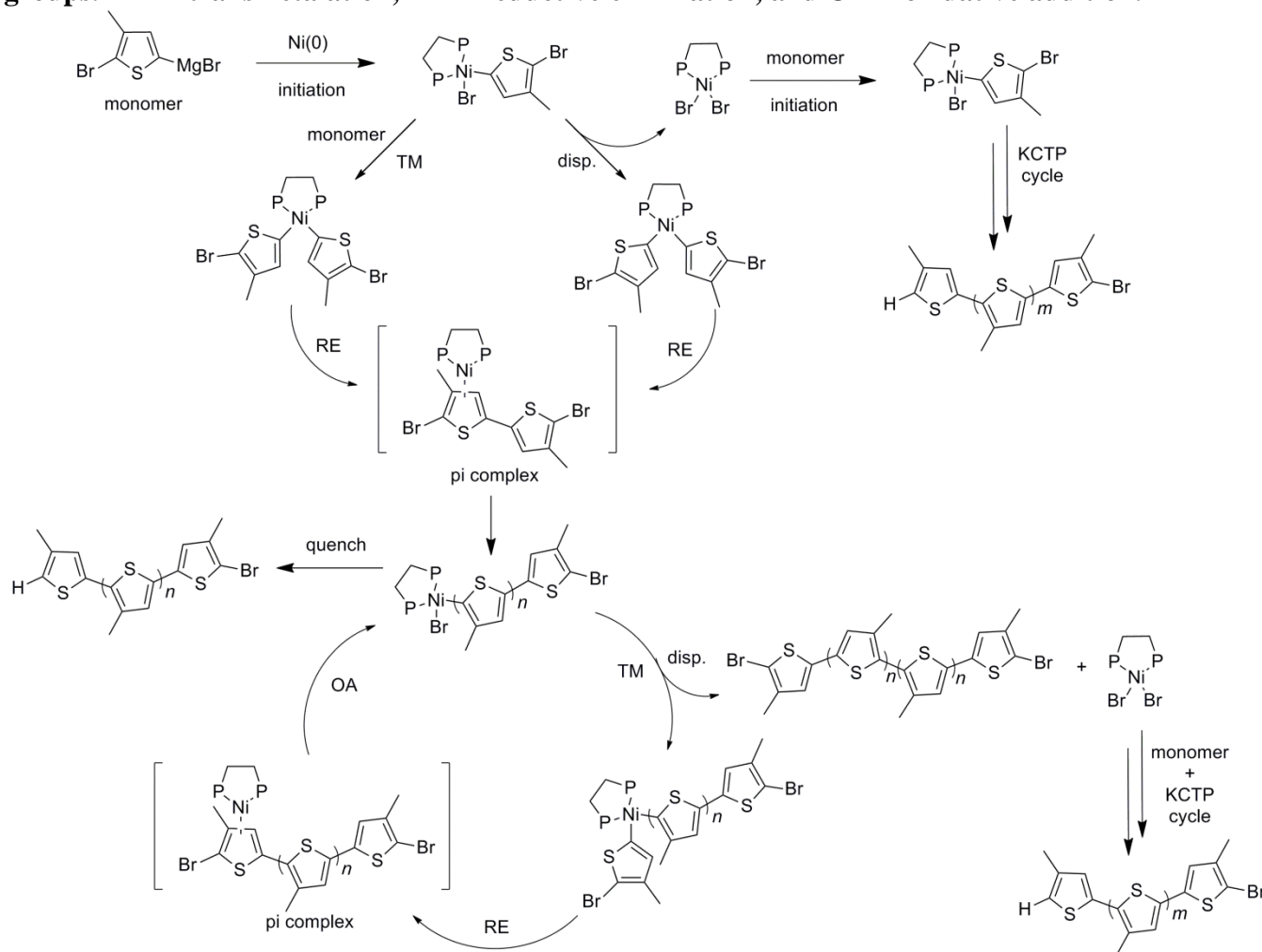
Comparison of Bite Angle

The bite angle of the ancillary ligand (P-Ni-P angle) has been speculated to strongly influence polymerization control.[4,7] Adding additional units to the carbon spacer of the ligand has the effect of increasing the bite angle about the nickel center. Once the spacer exceeds three carbons, polymerization becomes less controlled and undergoes intermolecular catalyst transfer resulting in increased dispersity and varying end groups.[4]
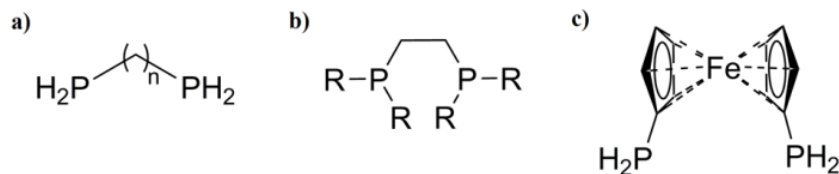
Figure 4.1. Ligands used in this report are abbreviated as follows: (a) n = 1: dhpe, n = 2: dhpp, n = 3: dhpb, (b) R = H: dhpe, R = methyl: dmpe, R = ethyl: depe, R = phenyl: dppe, (c) dhpf.

In order appropriately model the nickel complexes, hydrogen atoms were substituted for phenyl groups on the phosphino ligands to improve computational efficiency. This is a common simplification shown to be valid in previous literature reports.[8,9] Although phenyl and hydrogen substituents have different electronic properties, substituents and, thus, electronic environments are held constant in all calculations and only bite angle is varied. The order of experimentally averaged bite angles (obtained by averaging over a large number of X-ray crystallographic structures from the Cambridge Structural Database) is consistent with calculated structures in this report: ethyl < propyl < ferrocenyl < butyl.[10]

Table 4.1. Comparison of Ni(II) Initiators Differing in Ancillary Ligand Bite Angle

Ancillary Ligand	E_{disp}[a]	Averaged Bite Angle[b]	Computed Bite Angle	Đ[c] P3HT	Đ[d] PPP
dhpe	0.0	85.03	88.3	1.50	2.66
dhpp	6.2	91.08	97.4	1.12	1.74
dhpf	1.0	95.60	101.5	1.83	2.40
dhpb	–4.3	97.70	104.4	2.40	--

[a]Values given in kcal mol^{-1}. [b]Averaged crystallographic bite angles for an array of phenyl substituted species.[10] Reported dispersitites of [c]poly(3-hexylthiophene) and [d]poly(2,5-dihexyloxyphenylene) synthesized from catalysts with phenyl substituents on the phosphorous atoms.[4]

To examine the role of bite angle, disproportionation energies were calculated for a series of initiating species differing only in backbone of the ancillary ligand (Table 4.1). Thiophene (Th) units were used as the aryl species. Reported energies are in reference to Ni(dhpe)BrTh. It

is important to note the computed energies are not absolute values, but can only be viewed relative to one another.

We have calculated the energy exchange involved in disproportionation reactions and found values relative to dhpe of 6.2 kcal mol^{-1} for dhpp, –4.3 kcal mol^{-1} for dhpb, and 1.0 kcal mol^{-1} for dhpf. Our predicted trend in polymerization control is dhpb < dhpe < dhpf < dhpp. This is in sharp contrast to the order of bite angle: dhpe < dhpp < dhpf < dhpb. Comparing previous reports by Miyakoshi *et al.* where Đ decreases in the order of dhpb < dhpf < dhpe < dhpp, it is clear that the experimental trend is matched by our predicted trend based on disproportionation energies.[4]

A discrepancy exists between the reduced control in the polymerization of poly(3-hexylthiophene) (P3HT) with the ferrocenyl ligand and positive disproportionation energy. The primary distinction of dhpf is the differing electronic properties associated with the ferrocenyl backbone compared to a simple alkyl spacer. Using this ligand, Miyakoshi *et al.* synthesized low molecular weight polymer with high dispersity and diverse end groups. This result is in contrast to what is expected based on our disproportionation energy computations. When LiCl was added to the polymerization in an effort to increase the rate of transmetalation to bypass side reactions such as disproportionation, a polymer with higher molecular weight and smaller Đ was achieved when dppe or dppp was the ancillary ligand. This addition did not increase polymerization control when dppf was the ancillary ligand; a polymer of low molecular weight, high Đ (2.78), and varying end groups resulted. This indicates that an alternative reaction which does not compete with transmetalation is the cause of lessened control. The reaction rate of oxidative addition has been shown to be slow for dppf.[11, 12] Slow oxidative addition may allow for dissociation of Ni(0) from the growing chain, resulting in uncontrolled polymerization.

Disproportionation energies were also computed for complexes with 3-methylthiophene as the aryl group. The same trend is followed with values of 0.4 kcal mol^{-1} for dhpe, 6.4 kcal mol^{-1} for dhpp, –4.6 kcal mol^{-1} for dhpb, and 1.5 kcal mol^{-1} for dhpf. All values are in reference to complexes ligated by dhpe with thiophene as the aryl group. The addition of an ortho-substituent works to lessen disproportionation reactions as disproportionation energies are slightly raides for dhpe, dhpp, and dhpf. For dhpb, however, a greater about of disproportionation is expected.

Interestingly, the polymerization of poly(2,5-dihexyloxybenzene) (PPP)[4] followed the trend of higher Đ with decreasing E$_{disp}$ of that calculated from initiating complexes with thiophene as the aryl group. Therefore, the trend for disproportionation seems to be based on ancillary ligand characteristics more so than the electron donating/withdrawing abilities of the monomer itself.

Comparison of Cone Angle

Another geometric feature of the initiating complex is steric crowding of the nickel center which can be approximated by the cone angle.[13] Following Lanni *et al.*, we have studied a set of ligands with similar bite angles ranging from 87.3º to 92.2º and widely varying cone angles (Table 4.2).[5] All reported energies are in reference to Ni(dppe)BrTh.

Similar to the study of bite angle, trends in polymerization characteristics do not follow that of increasing or decreasing exact cone angle, which were computed as 199.4º, 217.0º, 218.6º, and 221.6º for dmpe, depe, dppe, and dppp, respectively. Computed angles match the ordering found by a survey of crystallographic structures from the Cambridge Structural Database.[13] Disproportionation energies show depe to have the highest tendency towards

disproportionation with a value of -5.6 kcal mol^{-1}. The dppp ligand, with a value of 0.5 kcal mol^{-1} is slightly less likely than dppe to undergo disproportionation. Surprisingly, dmpe has a relatively high disproportionation energy of 1.2 kcal mol^{-1} and as such should not undergo disproportionation as readily. This forms the predicted trend in polymerization control of depe < dppe < dppp < dmpe.

Table 4.2. Comparison of Ni(II) Initiators Differing in Ancillary Ligand Cone Angle

Ancillary Ligand	E_{disp}[a]	Bite Angle[b]	Exact Cone Angle[b]	Đ[c] PPP	Đ[d] P3HT	Đ[e] P3HT
dmpe	1.2	88.3	199.4	1.51	--	--
depe	-5.6	87.4	217.0	2.12	2.26	--
dppe	0.0	87.3	218.6	2.42[f]	2.29[f]	1.50
dppp	0.5	92.2	221.6	3.59[f]	1.77[f]	1.12

[a]Values given in kcal mol^{-1}. [b]Calculated from optimized geometries (see Chapter 2). Reported dispersities of [c]poly(2,5-dihexyloxyphenylene)[5], [d]poly(3-hexylthiophene)[5], and [e]poly(3-hexylthiophene).[4] [f]Polymerization conditions were not optimized.

Although correlations from disproportionation energy anticipate dmpe to minimize disproportionation, it is kinetically unstable, decomposes in solution, and, therefore, is not amenable to KCTP.[5] In the polymerization of P3HT, Lanni *et al.* observed a broad dispersity (2.12) due to slow initiation when depe was the ancillary ligand. Slowing of this key step (initiation) allows disproportionation to become competitive. Disproportionation at the initiation stage only increases dispersity and does not change the nature of resultant chain ends (Scheme 4.2). Analysis of end groups in the study confirmed only H/tolyl terminated polymers were present, which indicates chain-growth polymerization.

Following the trend in disproportionation energy, polymerization with depe as the ancillary ligand should exhibit less control than polymerization with dppe or dppp. In the aforementioned study, however, Lanni *et al.* state that depe "outperforms" dppe and dppp under

the specified reaction conditions.[5] The dispersities are higher than expected for a controlled chain-growth polymerization, which the authors attributed to unoptimized polymerization conditions for reactions containing dppe and dppp. Without proper optimization of polymerization conditions, no comparison can be made between the resultant Đs. Under optimized reaction conditions, Miyakoshi *et al.* observed a low Đ in the polymerization of P3HT for both dppe (1.50) and dppp (1.12), consistent with the trend in disproportionation energies.[4] Additional studies by Wu *et al.* observed no discernible changes after a resting period of 1 hr in the polymerization of P3HT with Ni(dppp)Cl$_2$ as the initiating species.[14] As such, dppp is shown to minimize disproportionation, but the reaction is not completely suppressed. Smeets *et al.* observed 10% of P3HT synthesized with initiator ligated by dppp to contain various, unexpected end groups (Br/Br, H/H, etc) which shows disproportionation still occurs.[15]

Excluding dmpe due to lack of stability, experiment has shown dppp to be the best performing ligand for KCTP followed by dppe, with depe providing very little control. This matches our predicted trend in disproportionation energy of depe < dppe < dppp. Although depe and dppe have similar cone angles (~156º), dppe has been shown to have greater polymerization control and a decreased tendency towards disproportionation.

Alternative Side Reaction Pathways

An alternative factor that potentially causes loss of polymerization control is Ni(0) diffusion after the reductive elimination step, which results in early termination as well as unwanted reinitiation. While the exact mechanism is still unclear, Kiriy *et al.* have convincingly argued that a single nickel complex polymerizes one chain.[16] The two main mechanistic schemes come from the McCullough group and the Yokozawa group. McCullough *et al.* state that the

nickel complex and growing chain generate an associated pair in which Ni(0) does not diffuse away.[17] In an equally compelling argument, Yokozawa *et al.* suggest intramolecular transfer of the nickel complex into the terminal C–Br bond of the polymer.[18] This was shown by examination of the initiator (aryl)Ni(II)Br formed *in situ* during the polymerization process.[4] Two thiophene units were coupled together in order to analyze end groups of the newly formed bithiophene. If H/Br end groups form intramolecular transfer occurs, while Br/Br end groups indicate Ni(0) diffusion. Even at extremely high concentrations of catalyst (50 mol %) only bithiophene with Br/H end groups were observed, meaning nickel diffusion does not occur.

Additionally, experimental and computational work has shown that Ni(0) can remain η-bound with a conjugated ring and "walk" along the π-framework until insertion into a C-Br bond is possible.[19] Komber *et al.* have recently observed that decreased ring-walking ability due to electron-deficient aromatic monomer units leads to disproportionated products.[20] These arguments strongly suggest that nickel diffusion after the reductive elimination step is unlikely. Therefore, disproportionation must be a major termination pathway that accounts for large molecular weight deviations and end group discrepancy.

A lone report by Achord *et al.* argues in favor of nickel diffusion, but with a high rate of reassociation.[21] A key argument in their case was the observation of Br/Br end groups, which do not result from the proposed KCTP chain-growth mechanism, which the authors claim is due to diffusion of free Ni(0). The authors did not consider other possible modes of termination or reinitiation, such as disproportionation, which can form polymer with Br/Br end groups (Scheme 4.2). Additionally, the authors observed that an increase in reaction time at high conversion leads to an increase in the percentage of undesired, double molecular weight Br/Br terminated polymer. We argue that the extended time period allowed for disproportionation as the monomer

concentration decreased and nickel complexes had an increased probability of reacting with one another to undergo disproportionation.

In addition to Ni(0) dissociation, magnesium halogen exchange can increase dispersity.[15,22] In this reaction a bromine atom at the terminal end of the polymer chain exchanges with the magnesium chloride group of the monomer. This places the Grignard reagent at the end of the chain which can transmetalate with another (aryl)Ni(II)Br causing further polymerization from both ends. Quenching results in H/H end groups which are distinctive from disproportionation and Ni(0) dissociation since both reactions only form polymer with H/Br and Br/Br end groups. Both McCullough and Koeckelberghs observed P3HT with H/H end groups and attributed this to a combination of magnesium-halogen exchange reactions and impure monomer.[15, 22]

Conclusions

This report has illustrated that loss of polymerization control in nickel-catalyzed cross-coupling reactions is not solely the effect of ligand geometry, but stems from a competing termination reaction: disproportionation. This process explains the decrease in control observed by some initiating species and is accomplished without nickel diffusion from the polymer chain after the reductive elimination step. The dispersity can be directly compared to the amount of unwanted side reactions by the appearance of a shoulder of double molecular weight in the gel permeation chromatogram, which indicates disproportionated products.[4,5] Đ as well as analysis of end groups can be compared to theoretically computed disproportionation energies to provide trends arising from different ligands.

Scheme 4.2 shows the two stages during the polymerization cycle where disproportionation is a competing reaction: initiation and transmetalation. Disproportionation at

the initiation stage releases free $Ni(II)Br_2$ into solution, which is reactivated by a double transmetalation reaction with two equivalents of monomer to start a separate polymerization cycle resulting in chains of differing length. Likewise, disproportionation *in lieu* of the transmetalation step results in chain-coupling to form chains of roughly double molecular weight with Br/Br end groups and free $Ni(II)Br_2$ which is once again reactivated to undergo further KCTP cycles, increasing dispersity.

Numerous experiments have confirmed improved control of KCTP by use of lithium chloride which speeds both initiation and transmetalation steps.[5, 23, 24] Recently noted in a report by the McNeil group, as the rate of precatalyst initiation is increased subsequent competing reaction pathways are outpaced resulting in polymers of highly uniform molecular weight.[25] These results suggest avoidance of the disproportionation pathway by accelerating the initiation step. Similarly, the rate of transmetalation is increased by forming a highly active "turbo-Grignard".[26] Reactions with turbo-Grignard allow transmetalation to proceed at a faster rate than disproportionation removing the bimodal molecular weight distribution.

Miyakoshi *et al.* observed a narrowing of molecular weight distribution and the disappearance of a high molecular weight shoulder at reduced reaction temperatures.[4] Decreasing temperature slows the rate of disproportionation such that the reaction is no longer competitive with intramolecular catalyst-transfer. This result, in conjunction with our calculated trends, shows that polymerization control is strongly influenced by disproportionation energy more so than ligand geometry. This value can be used to predict the presence of disproportionation in cross-coupling reactions and, therefore, aid in catalyst design. Further computational studies are currently underway to investigate additional details of other transition metal mediated cross-coupling polymerizations.

Theoretical Methods

Energetics of all species were computed with zero-point vibrational energy (ZPE) corrections using density functional theory with the QChem3.2 package.[27] Reported values were computed with the B3LYP functional, which has been shown to properly model organometallic transition metal complexes.[28-30] Two other functionals, M06 and PBE, were also shown to give matching trends.[31, 32] For all atoms aside from halogens and transition metals, the Dunning standard double-ζ contraction of Huzinaga primitive sets was used in accordance with previous reports.[33, 34] Halogens were treated using effective core potentials of the Stuttgart-Bonn type with complementary basis sets.[35] Following Schaefer *et al.*, nickel and iron employed the Wachters' primitive sets in a loosely contracted DZP fashion, augmented with two sets of p and one set of d functions designated (14s11p6d/10s8p3d).[36, 37] All complexes were confirmed to be geometrically minimized by the absence of imaginary vibrational frequencies. A radial, angular (75, 302) grid was accurate enough to ensure a geometric minimum for most complexes; when a small imaginary frequency presented itself a (99, 590) grid was enough to eliminate it. Several stable geometric orientations are possible for the phenyl moieties; we have used the lowest energy conformation described in previous reports.[38]

References

1. Sheina, E. E.; Liu, J.; Iovu, M. C.; Laird, D. W.; McCullough, R. D. *Macromolecules* **2004,** 37, (10), 3526-3528.

2. Yokoyama, A.; Miyakoshi, R.; Yokozawa, T. *Macromolecules* **2004,** 37, (4), 1169–1171.

3. Beryozkina, T.; Senkovskyy, V.; Kaul, E.; Kiriy, A. *Macromolecules* **2008,** 41, (21), 7817-7823.

4. Miyakoshi, R.; Yokoyama, A.; Yokozawa, T. J. *Polym. Sci., Part A: Polym. Chem.* **2008,** 46, (3), 753-765.

5. Lanni, E. L.; Locke, J. R.; Gleave, C. M.; McNeil, A. J. *Macromolecules* **2011,** 44, (13), 5136-5145.

6. Zenkina, O. V.; Karton, A.; Freeman, D.; Shimon, L. J. W.; Martin, J. M. L.; van der Boom, M. E. *Inorg. Chem.* **2008,** 47, (12), 5114-5121.

7. Doubina, N.; Stoddard, M.; Bronstein, H. A.; Jen, A. K. Y.; Luscombe, C. K. *Macromol. Chem. Phys.* **2009,** 210, (22), 1966–1972.

8. Ghosh, R.; Emge, T. J.; Krogh-Jespersen, K.; Goldman, A. S. *J. Am. Chem. Soc.* **2008,** 130, (34), 11317–11327.

9. Braga, A. A. C.; Ujaque, G.; Maseras, F. *Organometallics* **2006,** 25, (15), 3647-3658.

10. Dierkes, P.; W. N. M. van Leeuwen, P. *J. Chem. Soc., Dalton Trans.* **1999**, (10), 1519–1530.

11. Amatore, C.; Broeker, G.; Jutand, A.; Khalil, F. *J. Am. Chem. Soc.* **1997,** 119, (22), 5176-5185.

12. Serra-Muns, A.; Jutand, A.; Moreno-Mañas, M.; Pleixats, R. *Organometallics* **2008,** 27, (11), 2421-2427.

13. Niksch, T.; Görls, H.; Weigand, W. *Eur. J. Inorg. Chem.* **2010,** 2010, (1), 95–105.

14. Wu, S.; Huang, L.; Tian, H.; Geng, Y.; Wang, F. *Macromolecules* **2011,** 44, (19), 7558-7567.

15. Smeets, A.; Van den Bergh, K.; De Winter, J.; Gerbaux, P.; Verbiest, T.; Koeckelberghs, G. *Macromolecules* **2009,** 42, (20), 7638-7641.

16. Kiriy, A.; Senkovskyy, V.; Sommer, M. *Macromol. Rapid Commun.* **2011,** 32, (19), 1503–1517.

17. Iovu, M. C.; Sheina, E. E.; Gil, R. R.; McCullough, R. D. *Macromolecules* **2005,** 38, (21), 8649-8656.

18. Miyakoshi, R.; Yokoyama, A.; Yokozawa, T. *J. Am. Chem. Soc.* **2005,** 127, (49), 17542–17547.

19. Yoshikai, N.; Matsuda, H.; Nakamura, E. *J. Am. Chem. Soc.* **2008,** 130, (46), 15258–15259.

20. Komber, H.; Senkovskyy, V.; Tkachov, R.; Johnson, K.; Kiriy, A.; Huck, W. T. S.; Sommer, M. *Macromolecules* **2011**.

21. Achord, B. C.; Rawlins, J. W. *Macromolecules* **2009,** 42, (22), 8634-8639.

22. Liu, J.; Loewe, R. S.; McCullough, R. D. *Macromolecules* **1999,** 32, (18), 5777-5785.

23. Miyakoshi, R.; Shimono, K.; Yokoyama, A.; Yokozawa, T. *J. Am. Chem. Soc.* **2006,** 128, (50), 16012–16013.

24. Marshall, N.; Sontag, S. K.; Locklin, J. *Macromolecules* **2010,** 43, (5), 2137-2144.

25. Lee, S. R.; Bryan, Z. J.; Wagner, A. M.; McNeil, A. J. *Chem. Sci.* **2012**.

26. Krasovskiy, A.; Knochel, P. *Angew. Chem. Int. Ed.* **2004,** 43, (25), 3333-3336.

27. Shao, Y.; Molnar, L. F.; Jung, Y.; Kussmann, J.; Ochsenfeld, C.; Brown, S. T.; Gilbert, A. T. B.; Slipchenko, L. V.; Levchenko, S. V.; O'Neill, D. P.; DiStasio Jr, R. A.; Lochan, R. C.; Wang, T.; Beran, G. J. O.; Besley, N. A.; Herbert, J. M.; Yeh Lin, C.; Van Voorhis, T.; Hung Chien, S.; Sodt, A.; Steele, R. P.; Rassolov, V. A.; Maslen, P. E.; Korambath, P. P.; Adamson,

R. D.; Austin, B.; Baker, J.; Byrd, E. F. C.; Dachsel, H.; Doerksen, R. J.; Dreuw, A.; Dunietz, B. D.; Dutoi, A. D.; Furlani, T. R.; Gwaltney, S. R.; Heyden, A.; Hirata, S.; Hsu, C.-P.; Kedziora, G.; Khalliulin, R. Z.; Klunzinger, P.; Lee, A. M.; Lee, M. S.; Liang, W.; Lotan, I.; Nair, N.; Peters, B.; Proynov, E. I.; Pieniazek, P. A.; Min Rhee, Y.; Ritchie, J.; Rosta, E.; David Sherrill, C.; Simmonett, A. C.; Subotnik, J. E.; Lee Woodcock Iii, H.; Zhang, W.; Bell, A. T.; Chakraborty, A. K.; Chipman, D. M.; Keil, F. J.; Warshel, A.; Hehre, W. J.; Schaefer Iii, H. F.; Kong, J.; Krylov, A. I.; Gill, P. M. W.; Head-Gordon, M. *Phys. Chem. Chem. Phys.* **2006,** 8, (27), 3172-3191.

28. Lee, C.; Yang, W.; Parr, R. G. *Phys. Rev. B* **1988,** 37, (2), 785-789.

29. Becke, A. D. *J. Chem. Phys.* **1993,** 98, (7), 5648-5652.

30. Xu, Z.-F.; Xie, Y.; Feng, W.-L.; Schaefer, H. F. *J. Phys. Chem. A* **2003,** 107, (15), 2716-2729.

31. Zhao, Y.; Truhlar, D. *Theor. Chem. Acta.* **2008,** 120, (1), 215-241.

32. Adamo, C. B., V. *J. Chem. Phys.* **1998,** 110, (13), 6158-6170.

33. Dunning, T. H. *J. Chem. Phys.* **1970,** 53, (7), 2823-2834.

34. Huzinaga, S. *J. Chem. Phys.* **1965,** 42, (4), 1293–1303.

35. Bergner, A. D., M; Kuchle, W.; Stoll, H.; Preuss, H. *Mol. Phys.* **1993,** 80, (6), 1431–1441.

36. Hood, D. M. P., R. M.; Schaefer, H. F. *J. Chem. Phys.* **1979,** 71, (2), 705-713.

37. Wachters, A. J. H. *J. Chem. Phys.* **1970,** 52, (3), 1033–1037.

38. Korenaga, T.; Abe, K.; Ko, A.; Maenishi, R.; Sakai, T. *Organometallics* **2010,** 29, (18), 4025-4035.

CHAPTER 5

Π-COMPLEXATION IN NICKEL-CATALYZED CROSS-COUPLING REACTIONS
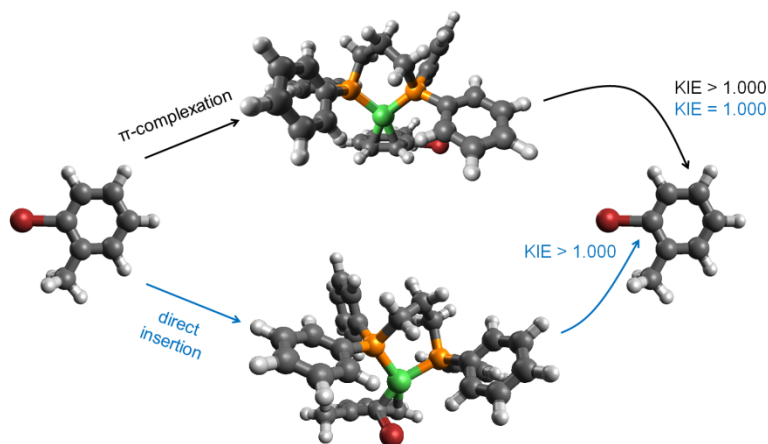
Abstract

The kinetic isotope effect (KIE) is used to experimentally elucidate the first irreversible step in oxidative addition reactions of a zerovalent nickel catalyst to a set of haloarene substrates. Halogenated *o*-methylbenzene, dimethoxybenzene, and thiophene derivatives undergo intramolecular oxidative addition through irreversible π-complexation. Density functional theory computations at the B3LYP-D3/TZ2P-LANL2TZ(f)-LANL08d level predict η^2-bound π-complexes are generally stable relative to solvated catalyst plus free substrate and that ring-walking of the Ni(0) catalyst and intramolecular oxidative addition are facile in these intermediates.

Introduction

The Kumada-Tamao-Corriu (KTC) reaction is commonly used for carbon-carbon cross-coupling in small molecule synthesis.[1-4] In such reactions, a zerovalent nickel catalyst undergoes a fundamental catalytic cycle involving oxidative addition (OA) to a reactive substrate, transmetallation with a Grignard reagent, and reductive elimination to form a carbon-carbon bond. The OA reaction, which initiates the catalytic cycle by conversion of starting materials to reactive intermediates, is known to be a two-step process with the transition metal catalyst first undergoing initial complexation with the substrate followed by nickel insertion.[5-7] The resulting intermediate is generally stable, and proceeds as the substrate for transmetallation in organometallic reactions. Some computational work has examined the role of oxidative addition for zerovalent group 10 metals in various cross-coupling reactions, mostly focusing on the nickel insertion step with limited substrates.[8-11]

In the KTC system, a π-complex is formed between the Ni(0) d-orbitals and the antibonding π-orbitals of the aryl substrate prior to halogen bond cleavage.[12] For an aryl bromide substrate initial π-complexation drives preferential bond activation even in the presence of a more reactive aryl iodide substrate.[13] This selectivity suggests that the Ni(0) species does not dissociate from the π-complex and must move along the conjugated framework (ring-walk) toward the active carbon-halogen site. Recently, small molecule competition reactions by the McNeil group have shown that intramolecular oxidative addition occurs.[14]

The nickel-mediated cross-coupling reaction is often used in the synthesis of near monodisperse, conjugated polymers.[15, 16] The π-complexation of zerovalent nickel with aromatic substrates plays a critical role in polymerization control, and weak association leads to uncontrolled polymerization.[17] The Ni(0) catalyst "chain-walks" along the aromatic polymer

backbone, and the nature of the aromatic system can alter this chain-walking phenomenon. A recent review by the McNeil group discusses our limited knowledge of the binding and whether the substrate is in η^2-, η^4-, or η^6-coordination with Ni(0).[18] An experimental and theoretical understanding of the interaction of Ni(0) catalysts with aromatic substrates promises to provide more efficient, selective catalysts for polymerization.

Though the formation of π-complexes plays an important role in many cross-coupling reactions, isolation or direct observation is often not possible due to the short lifetimes of these metastable species.[19, 20] However, the kinetic isotope effect (KIE) can provide information on the atoms involved in the first irreversible step (FIS) when a catalyst is involved.[7, 8, 21] In reactions such as OA involving bond rearrangements, substitution of heavier isotopes tends to enhance activation barriers and reduce reaction rates.[22] When probing carbon isotope effects, substrates containing the lighter ^{12}C atom will preferentially react, leaving ^{13}C enrichment at the active site in recovered starting material. An increased KIE (>1.000 relative to an internal standard) at an atomic position indicates involvement of this site in the FIS. Carbon-specific KIEs can be quantified by ^{13}C-NMR through comparison of ^{13}C ratios in the substrate before and after reaction.[23] In this case, deliberate isotopic labeling is unnecessary because the natural abundance of ^{13}C is sufficient for high-field NMR methods.

In this report, we perform KIE experiments on various haloarene derivatives to elucidate the OA mechanism. Aryl halides are coupled with alkyl or aryl magnesium halides using dppp-ligated nickel catalysts. Several thiophene derivatives are also investigated to understand Ni(0) interactions with aromatic rings containing a heteroatom. Additionally, reaction pathways were computed using B3LYP-D3/TZ2P-LANL2TZ(f)-LANL08d density functional theory. Initial π-complexation thermodynamically stabilizes the benzene and thiophene derivatives by up to 17

and 33 kcal mol^{-1}, respectively, relative to the solvated catalyst and free substrate, and all cross-couplings are exothermic with low barriers to OA. Theoretical KIEs for Ni(0) insertion were calculated using transition state theory[22] and found to differ from the observed KIEs, providing further evidence that the initial step for all studied substrates is not direct oxidative addition.

Computational Methods

Modeling the intramolecular OA of a zerovalent nickel with haloarene substrates was done with density functional theory (DFT) using the B3LYP functional,[24, 25] which yields accurate molecular geometries for transition-metal complexes.[26, 27] All geometry optimizations and frequency computations used the 6-31G* basis set for H, C, O, P, and S,[28,29] and the LANL2DZ basis set and effective core potential (ECP) for halogens and nickel.[30] Final energetics were computed with the B3LYP-D3 functional, which appends the Grimme dispersion correction[31] to B3LYP, along with a TZ2P basis set[32] contracted as (5s2p/3s2p) for H, (10s6p2d/5s3p2d) for C and O, and (14s10p2d/7s5p2d) for P and S, as well as the LANL2TZ(f) basis set and ECP for nickel and the LANL08d basis set and ECP for halogens.[33] This scheme is denoted as B3LYP-D3/TZ2P-LANL2TZ(f)-LANL08d. Electronic energies were corrected for zero-point vibrations. All computations employed a radial, angular (75, 302) grid with the QChem 4.0 package.[34] To validate our method, rigorous coupled-cluster computations were done for the complexation of Ni(dhpe) + ethene. CCSD/TZ2P-LANL2TZ(f) gives a binding energy of 45.6 kcal mol^{-1}, similar to the 43.4 kcal mol^{-1} found by B3LYP-D3/TZ2P-LANL2TZ(f). Transition state theory (TST) was used to determine theoretical KIEs for nickel insertion.[22] Theoretical KIEs were benchmarked against experimental KIEs for the Diels-Alder reaction of *s-trans*-isoprene and maleic anhydride.[35]

Results and Discussion

To examine substrate influence on the OA reaction, KIEs were measured for a set of haloarenes varying in halogen type (benzene derivatives), added electron-withdrawing groups, and substituent position (thiophene derivatives). Increased KIEs only in the immediate vicinity of the halogenated carbon would indicate that Ni(0) insertion is the first irreversible step and that π-complexation is reversible. Conversely, increased ratios distributed over the aryl ring would imply mechanistic involvement of carbons away from the OA reaction site, suggesting that π-complexation is the first irreversible step (FIS), and once the catalyst coordinates to the substrate then intramolecular OA occurs without dissociation of Ni(0). Our measured KIE values are reported in the figures below in a succinct notation. Differences are given with respect to the methyl internal standard, set at 1.000, and are reported as multiples of 0.001. For example, a KIE of +8 corresponds to 1.008 in the standard notation.

The stability of π-complexation varying by halogen type was first investigated for substituted *o*-halotoluenes (Figure 5.1). The experimental ^{13}C KIE values for the brominated substrate are (+5, +4, +6, +6, +8, +2), while the corresponding KIEs for the chlorinated substrate are (+17, +13, +2, +6, +17, +10). The enlargement in positions away from the site of oxidative addition indicates that π-complexation is the FIS. Intramolecular OA is expected for both species. This matches literature reports confirming chain-growth character in the KTC polymerization.[36]

Modeling the full OA reaction of Ni(dppp) with *o*-bromotoluene reveals that Ni(0) favorably complexes in an η^2 fashion with neighboring sp^2 carbons followed by ring-walking and nickel insertion, as shown in Scheme 5.1. In the KIE experiments, a free Ni(0) would initially be complexed to the THF solvent.[37] The THF is replaced by the aryl halide substrate at the start of the reaction sequence. This process cannot be described as a single step through a well-defined

transition state on the potential energy surface. While theoretical investigation of complicated exchange mechanisms among Ni(0) π-complexes is beyond the scope of this report, the associated thermodynamic effects are accounted for by computing relative energies based on the reaction THF-Ni(dppp) + substrate → substrate-Ni(dppp) + THF.

Scheme 5.1. Ring-Walking and Forward Nickel Insertion of Ni(dppp) with *o*-Bromotoluene[*a*]
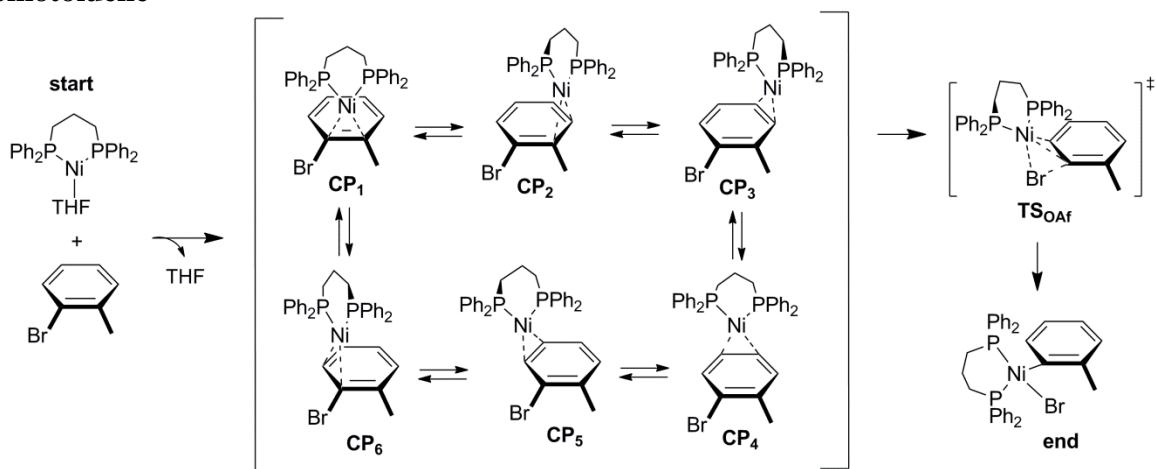
[*a*]Initial binding can occur at any position (CP$_x$).

Figure 5.1 displays the computed reaction profile for intramolecular OA of Ni(dppp) with the brominated (solid red trace) and chlorinated (dashed blue trace) derivatives. Initial π-complexation with the substrate provides 14–17 kcal mol^{-1} of thermodynamic stabilization depending on the binding position. All ring-walking steps have low energetic barriers of 3–7 kcal mol^{-1}. Ni(dppp) can migrate around the ring to the active site in either a forward direction away from the methyl substituent or in a reverse direction passing over the methyl moiety. OA occurs via a three-coordinate transition state (TS$_{OA}$) involving either C1–C6 or C1–C2 for forward and reverse ring-walking, respectively.

The main difference between the bromo- and chlorotoluene substrates is the nickel insertion barrier, which is somewhat higher for the chloro derivative. The insertion barriers in the forward direction are 4.6 and 9.0 kcal mol^{-1} for the bromo and chloro derivatives, while those in the reverse direction are 8.0 and 11.2 kcal mol^{-1}. In the forward ring-walking reaction with the brominated substrate, the barrier for insertion is lower in energy than that of ring-walking, which suggests extremely facile intramolecular oxidative addition. The reaction profiles of Figure 5.1, especially in the *o*-chlorotoluene case, suggest fast pre-equilibrium between the intermediates. allowing application of the Curtin-Hammett principle[38] or the energetic span model.[39] In particular, the apparent activation energy for nickel insertion in the reverse direction is predicted to be 12.5 kcal mol^{-1}, the difference between the energy of TS$_{OAr}$ and the lowest-energy intermediate CP$_6$. The thermodynamic driving force for OA after π-complexation exceeds 45 kcal mol^{-1}.
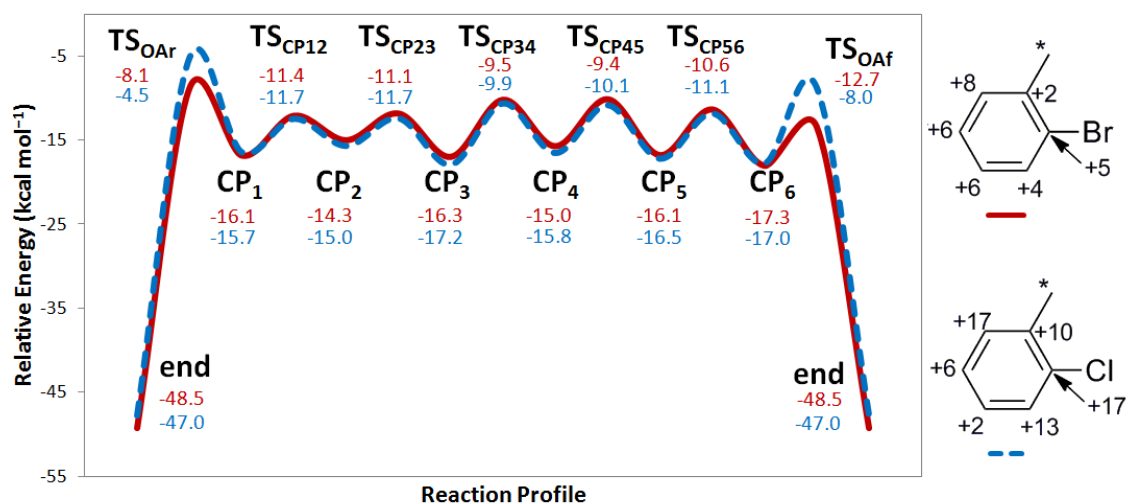
Figure 5.1. Computed reaction profile for intramolecular oxidative addition of Ni(dppp) with *o*-bromotoluene (solid red) and *o*-chlorotoluene (dashed blue). Energies relative to THF-Ni(dppp) + free substrate are listed for each step. Experimental KIEs are given using the shorthand notation defined in the text with an asterisk denoting the internal standard.

The experimental KIEs for the brominated derivative exhibited sizable enlargement on every aryl carbon, making π-complexation the apparent FIS. In contrast, for the nickel insertion step, our theoretical KIEs for C1 through C6 are (+4, +5, +2, +0, +0, +2) and (+5, +2, +0, +1, +3, +5) for the forward and reverse directions, respectively. The clear disparity between these theoretical values and the observed KIEs supports the conclusion that nickel insertion is not the FIS. For the chlorinated substrate, our theoretical KIEs for nickel insertion in the forward and reverse direction are (+6, +5, +1, −1, +0, +2) and (+8, +1, −1, −1, +2, +4). Again, substantial enlargement is only present on the active carbon and its neighbors, which does not match experiment, indicating nickel insertion is not the FIS.
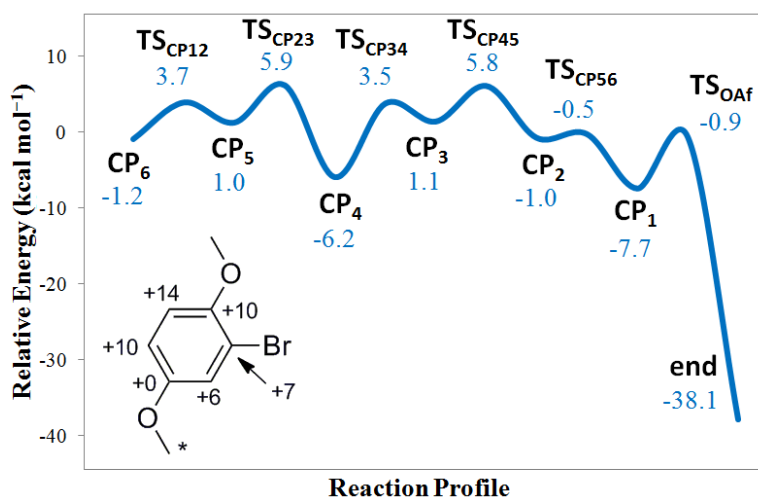
Figure 5.2. Computed reaction profile for intramolecular oxidative addition of Ni(dppp) with 1-bromo-2,5-dimethoxybenzene. The energies listed for each step are relative to THF-Ni(dppp) + free substrate. Experimental KIEs are inset.

The addition of methoxy substituents alters the relative energies of the various π-complexes (Fig. 5.2). Instead of all binding positions being of comparable energy, as for the halotoluene derivatives, the unsubstituted site C4 is favored by 6.2 kcal mol^{-1}. While the barriers to ring-walking out of the deepest CP$_4$ and CP$_1$ minima are 7–12 kcal mol^{-1}, the others are only

2–5 kcal mol^{-1}. The barrier nickel insertion from the unhindered side is only slightly higher at 6.8 kcal mol^{-1}. No transition state was located for nickel insertion from the hindered side

The experimental KIEs (+7, +10, +14, +10, +0, +6) for 1-bromo-2,5-dimethoxybenzene are elevated around the ring. In contrast, the theoretical KIEs for nickel insertion (+3, +2, +1, −1, +0, +0) exhibit noticeably increased values only at the two carbons involved in the three-coordinate OA transition state (C1 and C2). The theoretical KIEs for nickel insertion do not reflect trends in the experimental KIEs, implying π-complexation is the apparent FIS.

Scheme 5.2. Intramolecular Oxidative Addition of Ni(dppp) with 2-Bromo-3-methylthiophene.
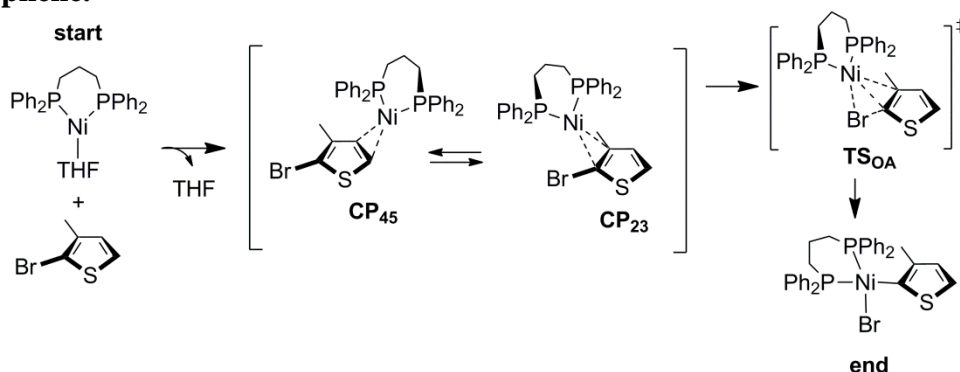
Thiophene compounds were investigated to study heteroatom effects on the OA mechanism, which are of relevance in small molecule cross-couplings and conjugated polymers.[16, 40, 41] A key difference between the toluene and thiophene derivatives is the mode of ring-walking. Nickel can complex with toluene derivatives at any adjacent pair of aryl carbons, but thiophene π-complexation only occurs at the C2–C3 and C4–C5 positions, as outlined in Scheme 5.2. No stationary points were found on the potential energy surface for Ni(dppp) complexed with the sulfur atom of thiophene.

Figure 5.3 shows the computed reaction profiles and experimental KIEs for bromothiophene derivatives. The substrate 2-bromo-3-methylthiophene has increased KIEs at C4 and C5 of +22 and +12. The lack of an increased KIE at C3 and the much smaller increase at C2 indicates that nickel insertion is not the FIS. When the methyl substituent is in the 5-position, experimental KIEs are spread throughout the ring at (+17, +4, +6, +16). The theoretical KIEs for nickel insertion are (+4, +5, +3, +0) for 2-bromo-3-methylthiophene and (+3, +6, +4, +1) for 2-bromo-5-methylthiophene. This disparity suggests π-complexation is the FIS.

In the 3-methyl and 5-methyl thiophene derivatives, the barriers to forward ring-walking are 14.5 and 13.5 kcal mol^{-1}, respectively, much larger than found in the halogenated toluene derivatives. The corresponding barriers to nickel insertion in the forward direction are 9.8 and 8.0 kcal mol^{-1}, comparable to the bromotoluene values.
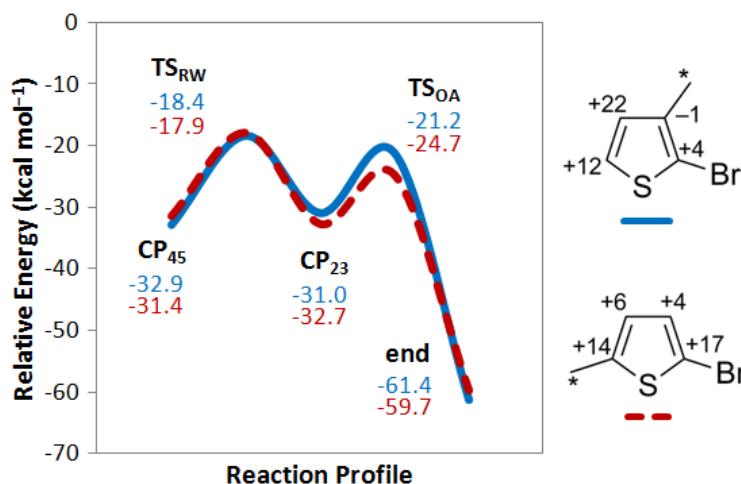
Figure 5.3. Computed reaction profiles and experimental KIEs for 2-bromo-3-methylthiophene (solid blue trace) and 2-bromo-5-methylthiophene (dashed red trace). Energies are listed for each step relative to THF-Ni(dppp) + free substrate.

Conclusions

In summary, Kumada coupling reactions were carried out here on a collection of halogenated arene derivatives. Experimental and computational methods were combined to elucidate the reactions of zerovalent nickel with aromatic substrates. Kinetic isotope effects (KIEs) were obtained from ^{13}C-NMR integrations of starting material before and after cross-coupling. Inverse-gated decoupling allowed for accurate peak integration, and the relaxation agent Cr(acac)$_3$ significantly decreased NMR acquisition time. Our joint experimental and theoretical analysis indicates that the first irreversible step (FIS) in the oxidative addition of Ni(0) with haloarenes is π-complexation, followed by intramolecular nickel insertion. The observed characteristics of π-complexation are of mechanistic importance in the Kumada catalyst-transfer polymerization of these substrates, as dissociation of the Ni(0) catalyst between the reductive elimination and subsequent oxidative addition step results in a loss of chain-growth behavior. Initial π-complexation is a contributing factor to obtaining a chain-growth polymerization with low dispersity and controlled end groups.

References

1. Tamao, K.; Sumitani, K.; Kumada, M. *J. Am. Chem. Soc.* **1972,** 94, (12), 4374-4376.

2. Jana, R.; Pathak, T. P.; Sigman, M. S. *Chem. Rev.* **2011,** 111, (3), 1417-1492.

3. Corriu, R. J. P.; Masse, J. P. *J. Chem. Soc., Chem. Commun.* **1972**, (3), 144.

4. Yamamoto, T.; Wakabayashi, S.; Osakada, K. *J. Organomet. Chem.* **1992,** 428, (1–2), 223-237.

5. Churchill, D. G.; Janak, K. E.; Wittenberg, J. S.; Parkin, G. *J. Am. Chem. Soc.* **2003,** 125, (5), 1403-1420.

6. Jones, W. D. *Acc. Chem. Res.* **2002,** 36, (2), 140-146.

7. Gómez-Gallego, M.; Sierra, M. A. *Chem. Rev.* **2011,** 111, (8), 4857-4963.

8. Yoshikai, N.; Matsuda, H.; Nakamura, E. *J. Am. Chem. Soc.* **2008,** 130, (46), 15258-15259.

9. Li, Z.; Jiang, Y.-Y.; Fu, Y. *Chem. Eur. J.* **2012,** 18, (14), 4345-4357.

10. Gøgsig, T. M.; Kleimark, J.; Nilsson Lill, S. O.; Korsager, S.; Lindhardt, A. T.; Norrby, P.-O.; Skrydstrup, T. *J. Am. Chem. Soc.* **2011,** 134, (1), 443-452.

11. McMullin, C. L.; Jover, J.; Harvey, J. N.; Fey, N. *Dalton Trans.* **2010,** 39, (45), 10833-10836.

12. Massera, C.; Frenking, G. *Organometallics* **2003,** 22, (13), 2758-2765.

13. Zenkina, O. V.; Karton, A.; Freeman, D.; Shimon, L. J. W.; Martin, J. M. L.; van der Boom, M. E. *Inorg. Chem.* **2008,** 47, (12), 5114-5121.

14. Bryan, Z. J.; McNeil, A. J. *Chem. Sci.* **2013,** 4, (4), 1620-1624.

15. Sheina, E. E.; Liu, J.; Iovu, M. C.; Laird, D. W.; McCullough, R. D. *Macromolecules* **2004,** 37, (10), 3526-3528.

16. Miyakoshi, R.; Yokoyama, A.; Yokozawa, T. *J. Am. Chem. Soc.* **2005,** 127, (49), 17542-17547.

17. Bridges, C. R.; McCormick, T. M.; Gibson, G. L.; Hollinger, J.; Seferos, D. S. *J. Am. Chem. Soc.* **2013**.

18. Bryan, Z. J.; McNeil, A. J. *Macromolecules* **2013**.

19. Zenkina, O. V.; Karton, A.; Freeman, D.; Shimon, L. J. W.; Martin, J. M. L.; van der Boom, M. E. *Inorg. Chem.* **2008,** 47, (12), 5114-5121.

20. Lanni, E. L.; Locke, J. R.; Gleave, C. M.; McNeil, A. J. *Macromolecules* **2011,** 44, (13), 5136-5145.

21. Vo, L. K.; Singleton, D. A. *Org. Lett.* **2004,** 6, (14), 2469-2472.

22. Smith, I. W. M., *Kinetics and dynamics of elementary gas reactions.* Butterworth & Co Publishers Ltd: Wobrun, Ma, 1980.

23. Singleton, D. A.; Thomas, A. A. *J. Am. Chem. Soc.* **1995,** 117, (36), 9357-9358.

24. Lee, C.; Yang, W.; Parr, R. G. *Phys. Rev. B* **1988,** 37, (2), 785-789.

25. Becke, A. D. *J. Chem. Phys.* **1993,** 98, (7), 5648-5652.

26. Niu, S.; Hall, M. B. *Chem. Rev.* **2000,** 100, (2), 353-406.

27. Xu, Z.-F.; Xie, Y.; Feng, W.-L.; Schaefer, H. F. *J. Phys. Chem. A* **2003,** 107, (15), 2716-2729.

28. Dill, J. D.; Pople, J. A. *J. Chem. Phys.* **1975,** 62, (7), 2921-2923.

29. Francl, M. M.; Pietro, W. J.; Hehre, W. J.; Binkley, J. S.; Gordon, M. S.; DeFrees, D. J.; Pople, J. A. *J. Chem. Phys.* **1982,** 77, (7), 3654-3665.

30. Hay, P. J.; Wadt, W. R. *J. Chem. Phys.* **1985,** 82, (1), 299-310.

31. Grimme, S.; Antony, J.; Ehrlich, S.; Krieg, H. *J. Chem. Phys.* **2010,** 132, (15), 154104.

32. Thomas, J. R.; DeLeeuw, B. J.; Vacek, G.; Crawford, T. D.; Yamaguchi, Y.; Schaefer, H. F. *J. Chem. Phys.* **1993,** 99, (1), 403-416.

33. Roy, L. E.; Hay, P. J.; Martin, R. L. *J. Chem. Theory Comput.* **2008,** 4, (7), 1029-1031.

34. Shao, Y.; Fusti-Molnar, L.; Jung, Y.; Kussmann, J.; Ochsenfeld, C.; Brown, S. T.; Gilbert, A. T. B.; Slipchenko, L. V.; Levchenko, S. V.; O'Neill, D. P.; Distasio Jr, R. A.; Lochan, R. C.; Wang, T.; Beran, G. J. O.; Besley, N. A.; Herbert, J. M.; Yeh Lin, C.; Van Voorhis, T.; Hung Chien, S.; Sodt, A.; Steele, R. P.; Rassolov, V. A.; Maslen, P. E.; Korambath, P. P.; Adamson, R. D.; Austin, B.; Baker, J.; Byrd, E. F. C.; Dachsel, H.; Doerksen, R. J.; Dreuw, A.; Dunietz, B. D.; Dutoi, A. D.; Furlani, T. R.; Gwaltney, S. R.; Heyden, A.; Hirata, S.; Hsu, C.-P.; Kedziora, G.; Khalliulin, R. Z.; Klunzinger, P.; Lee, A. M.; Lee, M. S.; Liang, W.; Lotan, I.; Nair, N.; Peters, B.; Proynov, E. I.; Pieniazek, P. A.; Min Rhee, Y.; Ritchie, J.; Rosta, E.; David Sherrill, C.; Simmonett, A. C.; Subotnik, J. E.; Lee Woodcock III, H.; Zhang, W.; Bell, A. T.; Chakraborty, A. K.; Chipman, D. M.; Keil, F. J.; Warshel, A.; Hehre, W. J.; Schaefer III, H. F.; Kong, J.; Krylov, A. I.; Gill, P. M. W.; Head-Gordon, M. *Phys. Chem. Chem. Phys.* **2006,** 8, (27), 3172-3191.

35. Beno, B. R.; Houk, K. N.; Singleton, D. A. *J. Am. Chem. Soc.* **1996,** 118, (41), 9984-9985.

36. Marshall, N.; Sontag, S. K.; Locklin, J. *Macromolecules* **2010,** 43, (5), 2137-2144.

37. Helm, L.; Merbach, A. E. *Chem. Rev.* **2005,** 105, (6), 1923-1960.

38. Seeman, J. I. *Chem. Rev.* **1983,** 83, (2), 83-134.

39. Kozuch, S.; Shaik, S. *Acc. Chem. Res.* **2010,** 44, (2), 101-110.

40. Vechorkin, O.; Proust, V. r.; Hu, X. *J. Am. Chem. Soc.* **2009,** 131, (28), 9756-9766.

41. Beryozkina, T.; Senkovskyy, V.; Kaul, E.; Kiriy, A. *Macromolecules* **2008,** 41, (21), 7817-7823.

CHAPTER 6

RING-WALKING OF ZEROVALENT NICKEL ON ARYL HALIDES
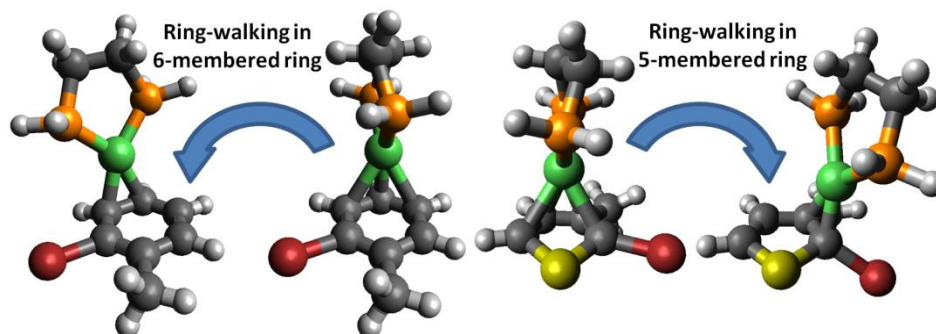
Bilbrey, J. A.; Locklin, J.; Allen, W. D. To be submitted to the *Journal of Chemical Theory and Computation*.

Abstract

While ring-walking is an important intermediate step in transition metal catalyzed cross-coupling reactions, the metastable intermediates are often difficult to isolate. In this work, theoretical structures and energetics of intramolecular addition of zerovalent nickel with 1-bromo-2-methylbenzene, 2-bromopyridine, 2-bromo-3-methylthiophene, and 2-bromopyrrole were computed at the B3LYP-D3/TZ2P-LANL2TZ(f)-LANL08d level. Mechanisms for the six-membered and five-membered rings are inherently unique—the catalyst moves along the edge of the six-membered rings and traverses the center of the five-membered rings. The importance of including a dispersion correction is also discussed.

Introduction

Group 10 transition metals are widely used to catalyze carbon-carbon cross-coupling in a variety of reactions.[1-3] In Kumada coupling, a zerovalent nickel complex undergoes a fundamental cycle of oxidative addition, transmetallation, and finally reductive elimination to form a new carbon–carbon bond.[4-6] The initial step for oxidative addition of the catalyst into an aryl substrate involves coordination of the metal to the substrate, known as π-complexation.[7-10] In reactions where more than one coupling is desired, as in polymerizations, this complexation allows the transition metal catalyst to remain loosely bound to the aryl substrate after reductive elimination through interaction of the Ni(0) d-orbitals and aryl antibonding π-orbitals.[9] The nickel catalyst moves along the conjugated system of the substrate until a carbon–halogen bond is reached to afford intramolecular oxidative addition.[11] This movement, called ring-walking, is a key intermediate to numerous transition metal catalyzed cross-coupling reactions.[12-18] Although thermodynamically stable, these complexes are often difficult to isolate because of the fast kinetics of ring-walking and oxidative addition.[7,13] Thus, theoretical computations to determine the structure of intermediates are useful for understanding the underlying mechanism. Several computational studies have reported theoretical reaction profiles for cross-coupling reactions,[11-13] yet few have discussed structural details of the ring-walking process itself.[19] Even then, only benzene derivatives were considered.

In this report, we detail the reaction profile of intramolecular oxidative addition as well as computed structures of all pertinent intermediates and transition states. Benzene, pyridine, thiophene, and pyrrole derivatives were studied as these monomers are commonly used in Kumada catalyst-transfer polycondensation (KCTP), which relies heavily on the stability of resulting π-complexes.[11,20,21] In accordance with previous reports, we find that the active

zerovalent nickel catalyst interacts through η^2 coordination with the aryl ring. Mechanisms for ring-walking were found to be unique depending on the size of the ring—the nickel moves around the outside of the 6-member rings and traverses across the center of the 5-member rings. All substrates then undergo 3-coordinate transition states for nickel insertion to complete the intramolecular oxidative addition step.

Computational Details

The ability for a zerovalent nickel complex to ring-walk across two different aryl substrates was examined through use of the B3LYP functional[22,23] on a radial, angular (75, 302) grid, which has been shown to accurately compute molecular geometries involving transition metal complexes.[24,25] Structures of all complexes in this report have been computed at the B3LYP/6-31G* level of theory[26,27] with Los Alamos effective core potentials (LANL2DZ)[28] for nickel and bromine atoms with the QChem 3.2 and 4.0 packages.[29] Energetics were computed with the B3LYP functional and Grimme's –D3 dispersion correction[30] with a TZ2P basis set contracted as ($5s2p/3s2p$) for H, ($10s6p2d/5s3p2d$) for C and N, and ($14s10p2d/7s5p2d$) for P and S,[31] along with the LANL2DZ ECPs for nickel and bromine with accompanying LANL2TZ(f) and LANL08d ECP basis sets.[32] This scheme is denoted as B3LYP-D3/TZ2P-LANL2TZ(f)-LANL08d in accordance with our previous work using the same computational scheme.[10] Intrinsic reaction coordinate computations were carried out with Ni(dhpe) complexes at the B3LYP/6-31G* level to assure transition states lead to the expected minima.

While the inclusion of Grimme's dispersion correction has little effect on the computed geometries of the aryl substrates and π-complexed species, shown in Chapter 1, dispersion plays a significant role in the energetics of π-complexed species. A benchmark calculation using couple

cluster singles and doubles (CCSD) with the TZ2P-LANL2TZ(f) basis set was carried out for the complexation of Ni(dhpe) to benzene, where dhpe stands for 1,2-bis(dihydrophosphino)ethane. The binding energy at this level is -30.8 kcal mol^{-1}. The B3LYP result gives a higher energy of -23.3 kcal mol^{-1}. If the $-$D3 correction is added, the binding energy decreases by 6.5 kcal mol^{-1}, which lowers the binding energy to only 1.0 kcal mol^{-1} higher than the CCSD result. This shows that a dispersion correction is necessary for obtaining approximate energetics of a π-complexed system. Several other functionals were tested and B3LYP-D, B97-D, and M06-L were found to be within 1 kcal mol^{-1} of the CCSD result.

Large contributions from dispersion forces are not unusual in transition metal complexes that contain short distances between the substrate and metal.[33,34] Conjugation in the substrate allows for facile displacement of π-electrons which affords unusually strong long-range forces.[35] The π-electrons of the conjugated system become polarized toward the metal complex allowing open d-orbitals on the zerovalent nickel to interact through π-backbonding.[36] Confirming this, theoretical studies by Granatier *et al.* on the interaction of benzene with a bare platinum atom found that at short distances the d$-\pi$ interaction preferentially stabilizes the singlet ground state, and a partial covalent bond is formed.[37,38] It should be noted that this study found the addition of a dispersion correction to be repulsive, opposite of what we find for the Ni(dppp)$-$benzene interaction, and noted that accurate benchmarking is imperative. In their study, the platinum was in η^6-coordination with benzene and contained no organic ligands—a much different system than the one studied here. In the organometallic complexes in this study, we did not find a π-complex where Ni(dhpe) or Ni(dppp) was in η^6- or η^5-coordination with 6-membered or 5-membered substituted aromatic rings.

Results and Discussion

Ring-walking of a zerovalent nickel on a benzene derivative has been previously reported in the literature, but the structure of intermediates and transition states were not fully discussed.[18] Here, we present a detailed mechanism along with the geometric changes associated with the ring-walking of a transition metal complex around a halogenated benzene derivative.

Free benzene has uniform carbon-carbon bond lengths of 1.40 Å throughout the ring, where changes on the order of 0.005 Å can result in decreased aromaticity.[39,40] Upon complexation Ni(0) binds to two adjacent aryl carbons in η^2-coordination at a Ni–C distance of 2.04–2.08 Å. Carbon-carbon bond lengths are distorted around the entirety of the ring with adjacent C–C bonds being elongated to 1.42–1.45 Å and β C–C bonds compressed to 1.37–1.38 Å (Table 6.1). Changes in bonding represent localization of π-electron density caused by π-backbonding with Ni(0), which causes the ring to become more electron rich.[41] The carbon-carbon bond distortions have the same pattern of elongation and compression as Ni(0) moves around the ring, binding in an η^2-manner with each C–C bond, which indicates continual backbonding with the mobile π-electrons. When Ni(0) moves to a position of π-complexation at a site adjacent to nickel insertion, either CP_1 or CP_6, binding is no longer symmetrical.

Table 6.1. Carbon-carbon Bond Lengths for Ni(dppp) Coordinated to 1-Bromo-2-methylbenzene

Complex	Bond Lengths (Å)					
	C1-C2	C2-C3	C3-C4	C4-C5	C5-C6	C6-C1
CP_1	1.44*	1.43	1.37	1.42	1.38	1.44
CP_2	1.43	1.44*	1.43	1.37	1.44	1.38
CP_3	1.37	1.43	1.44*	1.43	1.38	1.43
CP_4	1.42	1.37	1.43	1.44*	1.44	1.37
CP_5	1.37	1.43	1.37	1.43	1.45*	1.44
CP_6	1.43	1.38	1.42	1.37	1.44	1.45*

*Position of binding to Ni(dppp).

In CP$_1$ Ni–C1 is shortened to 1.96 Å, while Ni–C2 remains at 2.04 Å. Similarly, in CP$_6$ the Ni–C1 bond is shortened to 1.93 Å, while Ni–C6 stays at 2.08 Å. In both cases the C1–Br bond is extended to 2.07 Å for CP$_1$ and 2.09 Å for CP$_6$ from 1.99 Å as in the other π-complex conformers.

During the ring-walking process, the Ni(0) complex weaves in and out of the ring (Fig. 6.1a). Transition states occur in a pseudo-η^3 fashion with nickel almost directly over the central carbon. For example, when Ni(dppp) crosses from CP$_4$ to CP$_5$, denoted as TS$_{CP45}$, bond lengths of Ni with C4, C5, and C6 are 2.39 Å, 2.02 Å, and 2.40 Å, respectively (Fig. 6.1b). Overall barriers for ring-walking are 3–7 kcal mol^{-1}. Thus, walking is kinetically, as well as thermodynamically, accessible at normal reaction conditions.
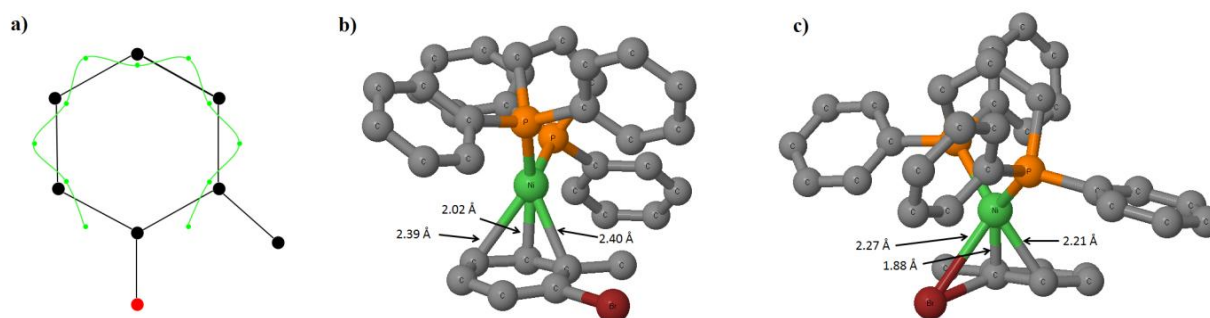
Figure 6.1. a) Representative path for Ni(dppp) ring-walking on *o*-bromotoluene and geometries of the transition state to b) ring-walking (TSCP$_{45}$) and c) nickel insertion in the forward direction (TS$_{OAf}$). Hydrogens have been omitted for clarity.

Nickel insertion occurs in a tri-coordinate transition state from either the unhindered side, ring-walking in the forward direction (TS$_{OAf}$), or the hindered side, reverse ring-walking (TS$_{OAr}$). In both cases the active site is C1, only the β carbon is different. The hindered transition state involves C6 coordination and is sterically hindered by the presence of a methyl substituent. This

causes a larger energetic barrier of 8.0 kcal mol^{-1}, compared with 4.6 kcal mol^{-1} on the unhindered side (Fig. 6.2). For TS$_{OAf}$, the Ni–C1 bond length is 1.88 Å, while the Ni–C2 length is 2.21 Å (Fig. 6.1c). For TS$_{OAr}$, the Ni–C1 bond length is 1.87 Å, while the Ni–C2 length is 2.32 Å. In both cases, the C1–Br bond elongates to 2.27 and 2.24 Å as the bond is broken.

There has been some criticism on truncating ancillary ligands, especially when phenyl groups are involved.[42] Pendant phenyl groups may have long-range interactions with the aryl substrate, changing the geometry and/or energetics of the complex. To test this hypothesis, we computed the ring-walking profile for 1-bromo-2-methylbenzene with Ni(dhpe), which replaces the phenyl groups on dppp with hydrogens and also shortens the ligand backbone from propyl to ethyl, and Ni(dhpp) which maintains the propyl backbone but truncates the phenyl groups to hydrogens. Mechanistically, the ring-walking process is the same for complexes with all three ligands—nickel is η^2-bound and moves around the ring in a three-coordinate transition state. For π-complexes, nickel–carbon bond lengths fall in the same range for Ni(dhpe) and Ni(dhpp) as with Ni(dppp). For non-active carbons (C2–C6) Ni–C bond distances range from 2.04–2.08 Å, while the active carbon (C1) has Ni–C bond lengths between 1.95–1.98 Å. Transition states to ring-walking also have similar geometries with middle Ni–C bonds ranging from 2.00–2.03 Å and side Ni–C bonds from 2.29–2.42 Å.

The difference between Ni(dhpe), Ni(dhpp), and Ni(dppp) in intramolecular oxidative addition is reflected in the reaction energetics. Figure 6.2 shows the reaction profiles for the complexation of *o*-bromotoluene with all three Ni(0) complexes computed with and without the inclusion of Grimme's −D3 dispersion correction. All reaction profiles are relative to the separated catalyst and aryl substrate.
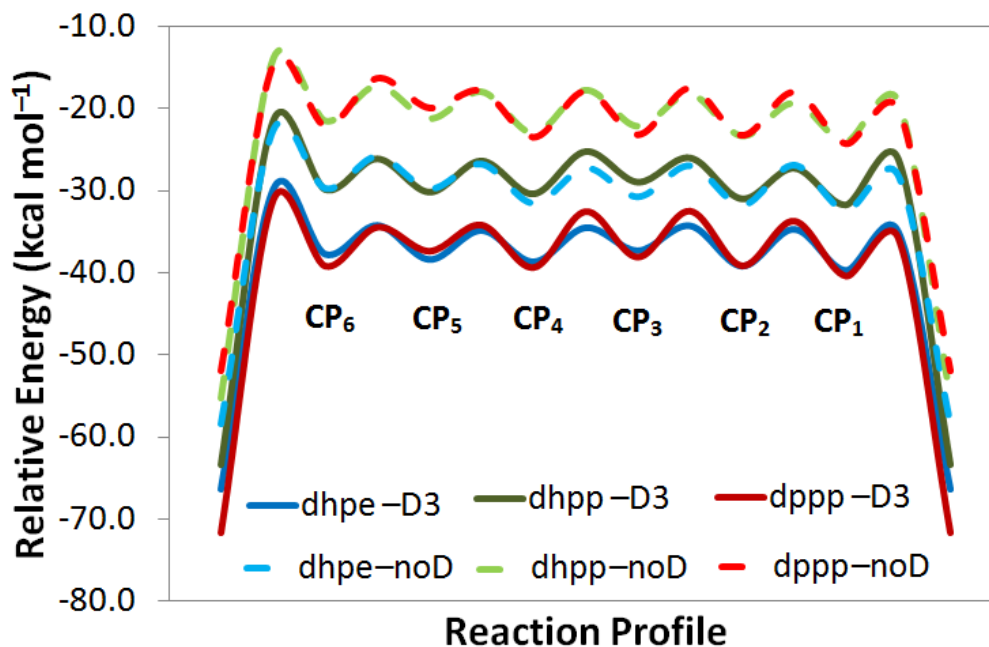
Figure 6.2. Reaction profile for the full oxidative addition reaction for *o*-bromotoluene with Ni(dhpe) (blue traces), Ni(dhpp) (green traces), and Ni(dppp) (red traces) with (solid traces) and without (dotted traces) Grimme's –D3 correction.

Not including the –D3 correction effectively removes energetic effects due to long-range van der Waals forces. For complexes with truncated ligands, Ni(dhpe) and Ni(dhpp), inclusion of –D3 lowers energetics by ~10 kcal mol^{-1}. With Ni(dppp), –D3 lowers energetics by ~20 kcal mol^{-1}. The reaction profile of Ni(dppp) with –D3 has similar energetics to that of Ni(dhpe) with –D3. The barriers to ring walking are slightly higher for Ni(dppp), but only by ~1.4 kcal mol^{-1}. The barriers to nickel insertion are lowered by less than 0.5 kcal mol^{-1}. Thus, the reaction profile of Ni(dppp) with the –D3 dispersion correction is best approximated by Ni(dhpe) with –D3. Interestingly, Ni(dhpp) with –D3 lies ~10 kcal mol^{-1} higher, which coincides with the reaction profile of Ni(dhpe) without –D3. The profile of Ni(dppp) without –D3 is best approximated by Ni(dhpp) without –D3.

From these studies, we conclude that it is important to include a correction for dispersion effects in computing the energetics of such π-complexed species. Though, if the goal of the computation is to find relative energetic effects then truncating the ligand to reduce computational cost and limit the range of conformers will provide similar results in terms of mechanistic steps, molecular geometries, and reaction barriers.

We then turned our attention to ring-walking of Ni(dppp) with an aromatic species containing a heteroatom. We find ring-walking of Ni(dppp) on 2-bromopyridine to be similar to that of 1-bromo-2-methylbenzene, even when nitrogen is involved in complexation. Nickel moves around the ring in an η^2-manner until intramolecular oxidative addition is possible. A key difference is the slight asymmetry involved in the nickel–carbon or nickel–nitrogen bond lengths. For example, at position CP_3, which does not involve the nitrogen atom or the brominated carbon, the Ni–C3 bond length is 2.01 Å while the Ni–C4 bond length is 2.05 Å. In general, Ni–C bond lengths for complexation, for non-active carbons (C2–C5), range from 2.00 Å to 2.05 Å, while the bond distances for Ni–C1 are 1.93 and 1.89 Å in CP_1 and CP_6, respectively. Nickel–nitrogen bond lengths are shorter than the non-active carbon–nickel bond lengths at 1.96 Å in CP_5 and 1.94 Å in CP_6. Again, walking occurs through tri-coordinate transition states. The transition state to nickel insertion is also tri-coordinate with bond distances for Ni–C1 and Ni–C2 at 1.86 Å and 2.20 Å for the forward reaction, and bond distances for Ni–C1 and Ni–N at 1.86 Å and 2.05 Å for the reverse reaction. The C1–Br bond lengthens to 2.27 Å and 2.40 Å in the forward and reverse transition states.

Figure 6.3 shows the reaction profile for ring-walking of Ni(dppp) on 2-bromopyridine. Binding energies for each π-complex are not as homogeneous as with *o*-bromotoluene and range from –40.6 to –44.3 kcal mol^{-1}. The increased binding stability may be a result of the increased

propensity for metalation by the pyridine ring.[43] Ring-walking barriers range from 3.6 to 10.7 kcal mol^{-1}, which are larger than with *o*-bromotoluene, but still favorable in normal reaction conditions. The barrier for forward nickel insertion is 4.1 kcal mol^{-1}, while the reverse barrier is 2.8 kcal mol^{-1}. The reaction is exoergic by 71.9 kcal mol^{-1}.
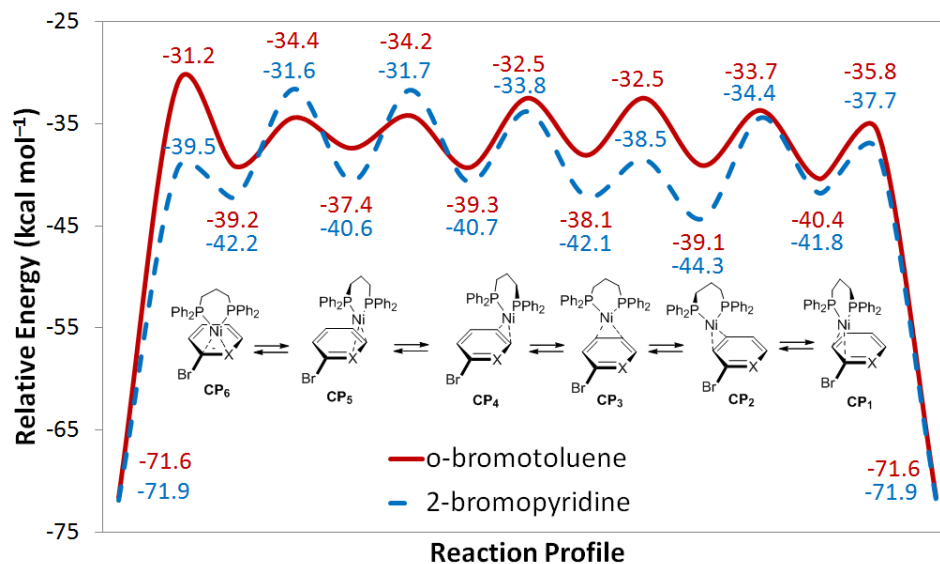
Figure 6.3. Reaction profile for intramolecular oxidative addition of Ni(dppp) into *o*-bromotoluene (solid red) and 2-bromopyridine (dashed blue), where X is either CCH_3 or N. Energies in reference to separated catalyst and substrate and are listed by each step in kcal mol^{-1}.
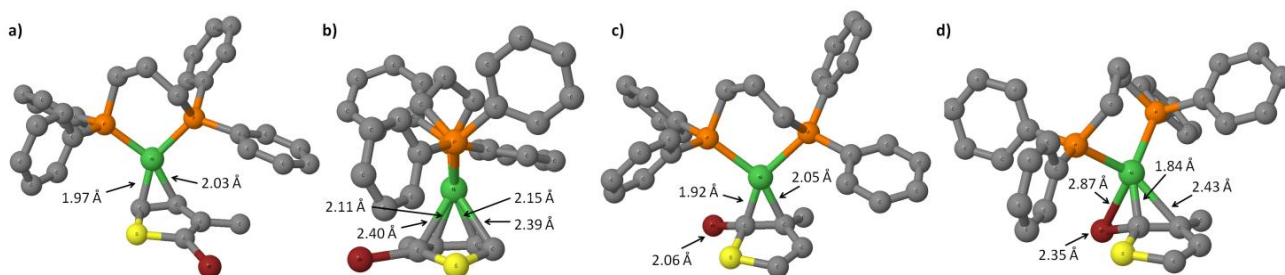

Figure 6.4. Geometries for ring-walking of Ni(dppp) on 2-bromo-3-methylthiophene of a) the bound state CP_{45}, b) the transition state to ring walking TS_{RW}, and c) the bound state CP_{23}, and d) transition state to nickel insertion TS_{OA}. Hydrogens have been omitted for clarity.

I next turned my attention to a thiophene derivative, as π-complexation is assumed to be a key intermediate step in the controlled polymerization of polythiophenes.[44] In previous reports, structures for metal binding to thiophene have been noted without discussing the specific motion around the ring.[36,45] We have identified the mechanistic scheme for ring-walking and nickel insertion of Ni(dppp) with 2-bromo-3-methylthiophene. The nickel complex initially forms an η^2-complex with the π-system of the carbon-carbon bonds adjacent to the sulfur atom, as shown in Figure 6.4. Complexation can occur on either side of the ring at CP_{45} or CP_{23} to provide 30.2 kcal mol^{-1} and 28.3 kcal mol^{-1} of stabilization, respectively (Figure 6.5). The Ni(0) traverses the ring in a pseudo-η^4 transition state and complexes in an η^2-manner with the π-system on the opposite side of the ring with a barrier of 14.5 kcal mol^{-1} in the forward direction (CP_{45} to CP_{23}) and 12.6 kcal mol^{-1} in the reverse direction. Nickel insertion into the C1–Br bond occurs through a tri-coordinate transition state with a 9.8 kcal mol^{-1} barrier. The complete oxidative addition reaction is exoergic by 58.7 kcal mol^{-1}.

Figure 6.4 depicts the geometry of π-complexes and transition states for Ni(dppp) with 2-bromo-3-methylthiophene. In CP_{45}, the nickel species is 1.97 Å from C5 and 2.03 Å from C4. The bond distance between C4 and C5 increases from 1.36 Å in the bare substrate to 1.44 Å, causing the double bond to lengthen to that of a single bond, as the carbon π-orbitals donate electron density to the nickel complex.

In the transition state for ring-walking, the nickel complex moves across the thiophene in a pseudo-η^4 fashion. Nickel is closer to C3 and C4 at 2.15 Å and 2.11 Å than carbons C2 and C5 at 2.40 Å and 2.39 Å, as a result of metal-sulfur antibonding interactions.[34] However, the bond lengths between C2 and C3 (1.40 Å) and C4 and C5 (1.39 Å) are closer to that of single bonds, which indicates minor donation of electrons from the metal to the carbon π-orbitals. The bond

length between C3 and C4 remains largely unchanged (from 1.46 Å to 1.44 Å). The overall C–C bond length pattern of short-long-short, as found in the bare substrate, remains in π-complexed intermediates. This is in contrast to observed stable η^4 complexes with thiophene where the pattern becomes long-short-long.[46] Interestingly, during ring-walking the sulfur atom is bent 16.4° out of plane whereas previously the ring was planar.
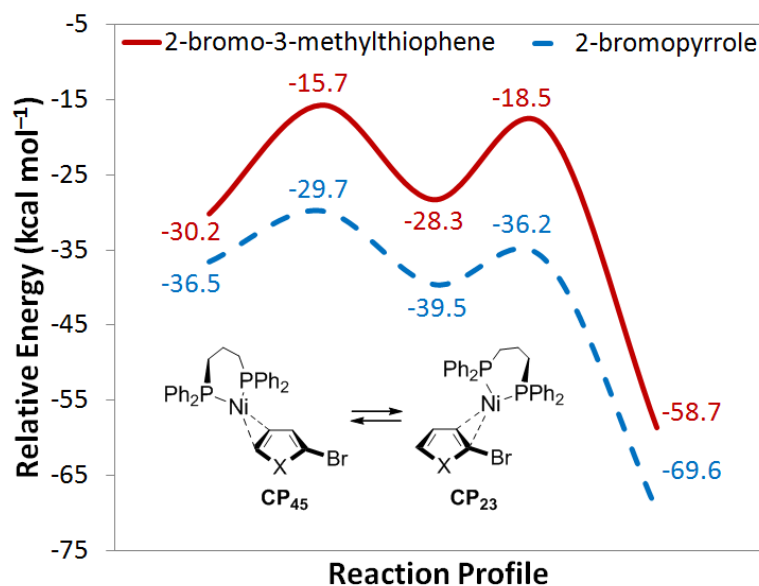
Figure 6.5. Reaction profile for intramolecular oxidative addition of Ni(dppp) into 2-bromo-3-methylthiophene (solid red) and 2-bromopyrrole (dashed blue), where X is either S or N. Energies in reference to separated catalyst and substrate and are listed by each step in kcal mol^{-1}.

After traversing the ring to form CP$_{23}$, nickel is bound to C2 and C3 at a distance of 1.92 Å and 2.05 Å. The methyl group is bent out of plane 26.5° to reduce steric crowding of the nickel complex. The C2–Br bond lengthens by 0.10 Å, and the bromine atom is bent out of plane by 44.1°. The C4–C5 bond length returns to 1.35 Å as the double bond is reformed, while the C2-C3 bond length increases to 1.44 Å to accommodate π-bonding to the metal complex.

The transition state to nickel insertion is tri-coordinate with bromine and the adjacent carbons. The nickel atom is closest to the brominated carbon (C2) with a bond length of 1.84 Å, and remains in close contact with C3 at a distance of 2.43 Å. The C2-C3 bond length remains elongated at 1.41 Å. As nickel insertion occurs in TS_{OA}, the Ni–Br bond begins to form at a length of 2.35 Å, and the bromine is bent out of plane by 36.9°. In the final structure, the Ni–Br bond length is 2.43 Å and the Ni–C2 bond length is 1.91 Å.

Polymerization of halogenated pyrrole substrates have been shown to proceed via catalyst-transfer.[47] We have found zerovalent nickel to undergo similar ring-walking behavior on 2-bromopyrrole. The reaction profile, shown in Figure 6.4, is similar to that of thiophene. The barrier to forward ring-walking is 6.8 kcal mol^{-1}, while the barrier for nickel insertion is 3.3 kcal mol^{-1}. Again, this is a highly exoergic reaction.

The nickel–substrate bond distances are slightly longer for the pyrrole substrate compared with the thiophene substrate. In the CP_{45} complex, the Ni–C4 and Ni–C5 distances are both 2.04 Å. In the transition state for ring-walking (TS_{RW}), Ni–C2, Ni–C3, Ni–C4, and Ni–C5 are 2.69 Å, 2.23 Å, 2.21 Å, and 2.69 Å, respectively. In the CP_{23} complex, the Ni–C2 and Ni–C3 distances are 1.94 Å and 2.06 Å. The transition state to nickel insertion is tri-coordinate with Ni–C2 and Ni–C3 bond distances of 1.84 Å and 2.32 Å.

Summary and Conclusions

In this report, the mechanism for zerovalent nickel ring-walking was found to be fundamentally different in 6-membered (benzene and pyridine) and 5-membered (thiophene and pyrrole) aromatic rings. In 6-membered rings, the nickel species moves along each C–C bond in η^3-coordination until nickel insertion is possible. In 5-membered rings, however, the nickel

species traverses the ring in a pseudo-η^4 manner. A tri-coordinate transition state for nickel insertion was found for all substrates with barriers below the separated reactants. Energetic barriers for motion around the ring, termed ring-walking, are lower than that of separated reactants, indicating ring-walking to be thermodynamically feasible. All barriers, for both insertion and walking, are below 15 kcal mol^{-1}, and thus are kinetically feasible in normal reaction conditions. Dispersion forces were shown to contribute to the overall energetics of the studied π-complexes, supplying 10 kcal mol^{-1} of stabilization for complexes with truncated ligands (dhpe and dhpp) and 20 kcal mol^{-1} of stabilization for the full Ni(dppp) complex. The geometric and energetic information presented here provides a better understanding of the mechanism behind intramolecular oxidative addition of zerovalent nickel with aromatic substrates.

References

(1) Tamao, K.; Sumitani, K.; Kumada, M. *J. Am. Chem. Soc.* **1972**, *94*, 4374-4376.

(2) Stille, J. K. *Angew. Chem. Int. Ed.* **1986**, *25*, 508-524.

(3) Miyaura, N.; Suzuki, A. *Chem. Rev.* **1995**, *95*, 2457-2483.

(4) Jana, R.; Pathak, T. P.; Sigman, M. S. *Chem. Rev.* **2011**, *111*, 1417-1492.

(5) Corriu, R. J. P.; Masse, J. P. *J. Chem. Soc., Chem. Commun.* **1972**, 144a-144a.

(6) Yamamoto, T.; Wakabayashi, S.; Osakada, K. *J. Organomet. Chem.* **1992**, *428*, 223-237.

(7) Churchill, D. G.; Janak, K. E.; Wittenberg, J. S.; Parkin, G. *J. Am. Chem. Soc.* **2003**, *125*, 1403-1420.

(8) Hratchian, H. P.; Chowdhury, S. K.; Gutiérrez-García, V. M.; Amarasinghe, K. K. D.; Heeg, M. J.; Schlegel, H. B.; Montgomery, J. *Organometallics* **2004**, *23*, 4636-4646.

(9) Massera, C.; Frenking, G. *Organometallics* **2003**, *22*, 2758-2765.

(10) Sontag, S. K.; Bilbrey, J. A.; Huddleston, N. E.; Sheppard, G. R.; Allen, W. D.; Locklin, J. *J. Org. Chem.* **2014**, *79*, 1836-1841.

(11) Miyakoshi, R.; Yokoyama, A.; Yokozawa, T. *J. Am. Chem. Soc.* **2005**, *127*, 17542-17547.

(12) Strawser, D.; Karton, A.; Zenkina, O. V.; Iron, M. A.; Shimon, L. J. W.; Martin, J. M. L.; van der Boom, M. E. *J. Am. Chem. Soc.* **2005**, *127*, 9322-9323.

(13) Zenkina, O. V.; Karton, A.; Freeman, D.; Shimon, L. J. W.; Martin, J. M. L.; van der Boom, M. E. *Inorg. Chem.* **2008**, *47*, 5114-5121.

(14) Fout, A. R.; Scott, J.; Miller, D. L.; Bailey, B. C.; Pink, M.; Mindiola, D. J. *Organometallics* **2008**, *28*, 331-347.

(15) Frischmann, P. D.; Gallant, A. J.; Chong, J. H.; MacLachlan, M. J. *Inorg. Chem.* **2007**, *47*, 101-112.

(16)   Strout, D. L.; Hall, M. B. *J. Phys. Chem. A* **1998**, *102*, 641-645.

(17)   Curran, K.; Risse, W.; Hamill, M.; Saunders, P.; Muldoon, J.; Asensio de la Rosa, R.; Tritto, I. *Organometallics* **2012**, *31*, 882-889.

(18)   Komber, H.; Senkovskyy, V.; Tkachov, R.; Johnson, K.; Kiriy, A.; Huck, W. T. S.; Sommer, M. *Macromolecules* **2011**, *44*, 9164-9172.

(19)   Yoshikai, N.; Matsuda, H.; Nakamura, E. *J. Am. Chem. Soc.* **2008**, *130*, 15258-15259.

(20)   Lanni, E. L.; Locke, J. R.; Gleave, C. M.; McNeil, A. J. *Macromolecules* **2011**, *44*, 5136-5145.

(21)   Yokozawa, T.; Nanashima, Y.; Ohta, Y. *ACS Macro Lett.* **2012**, *1*, 862-866.

(22)   Lee, C.; Yang, W.; Parr, R. G. *Phys. Rev. B* **1988**, *37*, 785-789.

(23)   Becke, A. D. *Phys. Rev. A* **1988**, *38*, 3098-3100.

(24)   Niu, S.; Hall, M. B. *Chem. Rev.* **2000**, *100*, 353-406.

(25)   Xu, Z.-F.; Xie, Y.; Feng, W.-L.; Schaefer, H. F. *J. Phys. Chem. A* **2003**, *107*, 2716-2729.

(26)   Hariharan, P. C.; Pople, J. A. *Theor. Chem. Acc.* **1973**, *28*, 213-222.

(27)   Rassolov, V. A.; Pople, J. A.; Ratner, M. A.; Windus, T. L. *J. Chem. Phys.* **1998**, *109*, 1223-1229.

(28)   Hay, P. J.; Wadt, W. R. *J. Chem. Phys.* **1985**, *82*, 299-310.

(29)   Shao, Y.; Fusti-Molnar, L.; Jung, Y.; Kussmann, J.; Ochsenfeld, C.; Brown, S. T.; Gilbert, A. T. B.; Slipchenko, L. V.; Levchenko, S. V.; O'Neill, D. P.; Distasio Jr, R. A.; Lochan, R. C.; Wang, T.; Beran, G. J. O.; Besley, N. A.; Herbert, J. M.; Yeh Lin, C.; Van Voorhis, T.; Hung Chien, S.; Sodt, A.; Steele, R. P.; Rassolov, V. A.; Maslen, P. E.; Korambath, P. P.; Adamson, R. D.; Austin, B.; Baker, J.; Byrd, E. F. C.; Dachsel, H.; Doerksen, R. J.; Dreuw, A.; Dunietz, B. D.; Dutoi, A. D.; Furlani, T. R.; Gwaltney, S. R.; Heyden, A.; Hirata, S.;

Hsu, C.-P.; Kedziora, G.; Khalliulin, R. Z.; Klunzinger, P.; Lee, A. M.; Lee, M. S.; Liang, W.; Lotan, I.; Nair, N.; Peters, B.; Proynov, E. I.; Pieniazek, P. A.; Min Rhee, Y.; Ritchie, J.; Rosta, E.; David Sherrill, C.; Simmonett, A. C.; Subotnik, J. E.; Lee Woodcock III, H.; Zhang, W.; Bell, A. T.; Chakraborty, A. K.; Chipman, D. M.; Keil, F. J.; Warshel, A.; Hehre, W. J.; Schaefer III, H. F.; Kong, J.; Krylov, A. I.; Gill, P. M. W.; Head-Gordon, M. *Phys. Chem. Chem. Phys.* **2006**, *8*, 3172-3191.

(30) Grimme, S. *J. Comp. Chem.* **2006**, *27*, 1787-1799.

(31) Thomas, J. R.; DeLeeuw, B. J.; Vacek, G.; Crawford, T. D.; Yamaguchi, Y.; Schaefer, H. F. *J. Chem. Phys.* **1993**, *99*, 403-416.

(32) Roy, L. E.; Hay, P. J.; Martin, R. L. *J. Chem. Theory Comput.* **2008**, *4*, 1029-1031.

(33) Chen, S.-L.; Blomberg, M. R. A.; Siegbahn, P. E. M. *J. Phys. Chem. B* **2011**, *115*, 4066-4077.

(34) Siegbahn, P. E. M.; Blomberg, M. R. A.; Chen, S.-L. *J. Chem. Theory Comput.* **2010**, *6*, 2040-2044.

(35) Margenau, H.; Kestner, N. R. *Theory of Intermolecular Forces*; Pergamon Press: Oxford, New York, 1969.

(36) Harris, S. *Organometallics* **1994**, *13*, 2628-2640.

(37) Granatier, J.; Lazar, P.; Otyepka, M.; Hobza, P. *J. Chem. Theory Comput.* **2011**, *7*, 3743-3755.

(38) Granatier, J.; Dubecký, M.; Lazar, P.; Otyepka, M.; Hobza, P. *J. Chem. Theory Comput.* **2013**, *9*, 1461-1468.

(39) Krygowski, T. M. *J. Chem. Inf. Model.* **1993**, *33*, 70-78.

(40) Cyrański, M. K.; Krygowski, T. M. *Tetrahedron* **1999**, *55*, 6205-6210.

(41) Harman, W. D. *Chem. Rev.* **1997**, *97*, 1953-1978.

(42) Ariafard, A.; Yates, B. F. *J. Am. Chem. Soc.* **2009**, *131*, 13981-13991.

(43) Davies, D. I. *Aromatic Heterocyclic Chemistry*; Oxford University Press: New York, 1991.

(44) Kiriy, A.; Senkovskyy, V.; Sommer, M. *Macromol. Rapid Commun.* **2011**, *32*, 1503-1517.

(45) Angelici, R. J. *Binding and Reactivity of Thiophene-Type Ligands in Transition Metal Complexes and Clusters*; Springer, 1998; Vol. 60.

(46) Rosini, G. P.; Jones, W. D. *J. Am. Chem. Soc.* **1992**, *114*, 10767-10775.

(47) Yokoyama, A.; Kato, A.; Miyakoshi, R.; Yokozawa, T. *Macromolecules* **2008**, *41*, 7271-7273.

CHAPTER 7

INSIGHTS INTO THE STILLE CROSS-COUPLING REACTION: INTRAMOLECULAR

OXIDATIVE ADDITION AND THE ROLE OF STERICS

Abstract

The influence of monomer properties in the Stille cross-coupling reaction is examined through small molecule competition reactions. In order for a system to be used in polymerization reactions, the palladium catalyst must undergo intramolecular oxidative addition with the monomer by remaining in association with the product after coupling. Here, monomers susceptible to intramolecular oxidative addition are shown to have a highly negative electrostatic potential about the aryl ring, while those unable to achieve intramolecular oxidative addition have more positive electrostatic potentials. Reaction sterics are also examined through the use of the exact solid angle to elucidate which steps in the catalytic cycle are most influenced by sterics. The transmetalation and reductive elimination steps show the most ligand crowding in their transition states, which indicates these steps are highly influenced by sterics involved in the catalytic complex.

Introduction

The Stille reaction, which couples two aryl or conjugated moieties, has been shown to be applicable to polymerization.[1-3] The reaction goes through repeating cycles of oxidative addition, transmetallation, and reductive elimination. In order for the Stille reaction to be a viable method for polymerization of conjugated polymers, the transition metal catalyst must stay in association with the coupled product and afford intramolecular oxidative addition.

Although the reaction cycle is similar to Kumada catalyst-transfer polycondensation (KCTP), there are two key differences: the transition metal catalyst is a zerovalent palladium and the metallating agent is an organotin reagent. The palladium catalyst can be used in both Stille coupling and KCTP, though the barrier to oxidative addition is higher for palladium than nickel, thus the reaction is typically carried out at increased temperatures.[4] The organotin reagent is less reactive than the Grignard reagent used in KCTP, which opens up the functional group compatibility to include esters, ethers, amines, and nitro groups.[5,6] Additionally, the organotin reagent can be stored in atmospheric conditions, while the Grignard reagent must be used immediately and degrades upon contact with water or atmospheric moisture.

The Stille system has not been thoroughly developed for the synthesis of conjugated polymers, thus in a joint experimental and computational study we elucidate mechanistic details of the intramolecular oxidative addition reaction, necessary for chain-growth polymerization, by studying monomer scope. This chapter will focus on the computational methods and overall findings for monomers varying in electron-withdrawing and electron-donating substituents. For more information on experimental methods see the Ph.D. dissertation of Eric Huddleston.[7] This chapter will also focos on the influence of sterics on different steps in the Stille coupling reaction cycle.

Intramolecular Oxidative Addition

Small molecule cross-coupling reactions have previously been used to investigate preferential oxidative addition in other cross-coupling systems,[8-10] so we have applied similar competitive reactions here. One equivalent of dihalogenated monomer was coupled with one equivalent of aryl-organotin reagent, as shown in Scheme 7.1. If the palladium complex does not stay in association with the coupled product, the biaryl species (**I**) will be formed. If the palladium complex stays in association with the coupled product and undergoes intramolecular oxidative addition, the triaryl species (**II**) will be preferentially formed. If palladium dissociation is on a similar time scale to intramolecular oxidative addition, a mixture of **I** and **II** will be formed.

Scheme 7.1. Stille Competition Reaction where OA = oxidative addition, TM = transmetalation, and RE = reductive elimination.
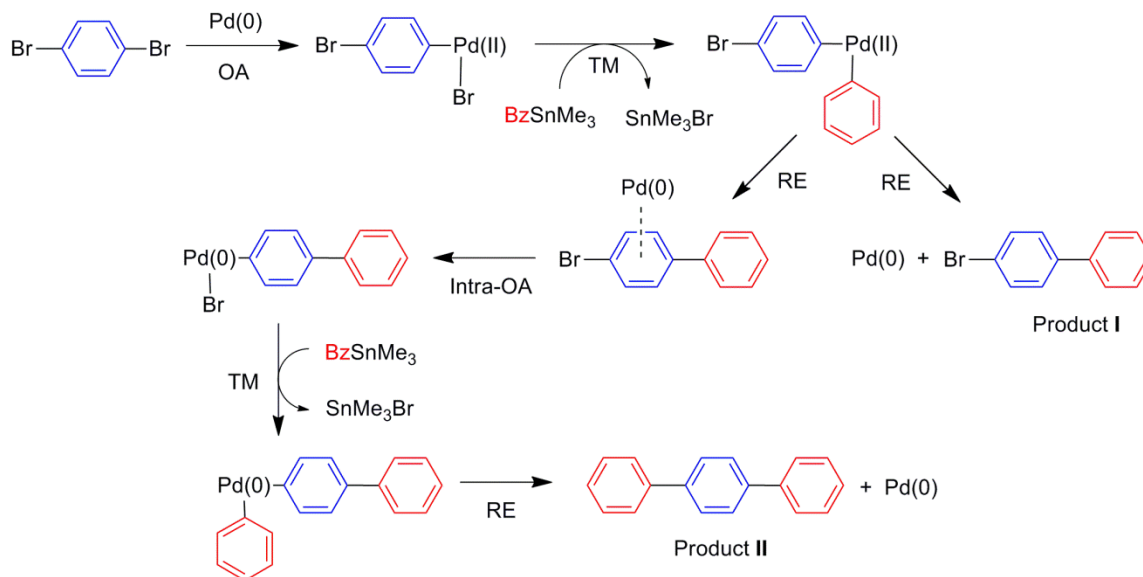

The association between the zerovalent palladium and the conjugated species is called a π-complex and behaves similarly to the nickel-aryl π-complex, discussed in Chapters 5 and 6.

Palladium has been shown to stay in association with a cross-coupled aryl product,[4] and it can be assumed that intramolecular oxidative addition occurs through a similar ring-walking process as in KCTP. Thus, by varying the monomer in the small molecule competition reaction shown above we can determine the nature of the π-complex and factors affecting its strength.

The catalyst $Pd(P^tBu_3)_2$ has been found to demonstrate intramolecular cross-coupling in the Stille reaction,[2] and thus was chosen as the catalyst for this study. Oxidative addition then occurs by a dissociative mechanism where one of the P^tBu_3 ligands is first removed to form the zerovalent monophosphine species $Pd(P^tBu_3)$, which is more active than its biphosphine counterpart.[11-13] The bulkiness of the ancillary ligand allows for the formation of a 3-coordinate complex during the reaction cycle, which speeds the oxidative addition step.[14,15] The P^tBu_3 ligand is a σ donor, which facilitates charge transfer from the metal to the antibonding orbitals of the aryl-halogen bond of the monomer.[16]

The monomer *p*-dibromobenzene was used as the parent molecule off of which the test molecules were built. Cross-coupling with this parent molecule gave 100% triaryl species, indicating that intramolecular oxidative addition happens on a much faster time scale than palladium dissociation. This can be explained by examining the electrostatic potential around the ring, though it should be noted that electrostatic potentials are only indicators of charge distribution in a molecule and don't map the electron density itself. A negative electrostatic potential corresponds to an area of attraction to a positive test charge and typically indicates concentrated electron density. A positive electrostatic potential corresponds to an area of repulsion to the positive test charge and typical indicated low electron density. Electrostatic potentials were computed at the HF/cc-pVTZ level using B3LYP/6-31G(d,p) geometries with the GAMESS program.[17-22]

As seen in Figure 7.1, the electrostatic potential of the benzene ring in both the monomer, *p*-bromobenzene, and biaryl intermediate, 4-bromobiphenyl, are highly negative. The high electron density assumed to be present in the ring is great enough to attract the d-orbitals of the zerovalent palladium and hold the complex in association until intramolecular oxidative addition is achieved.
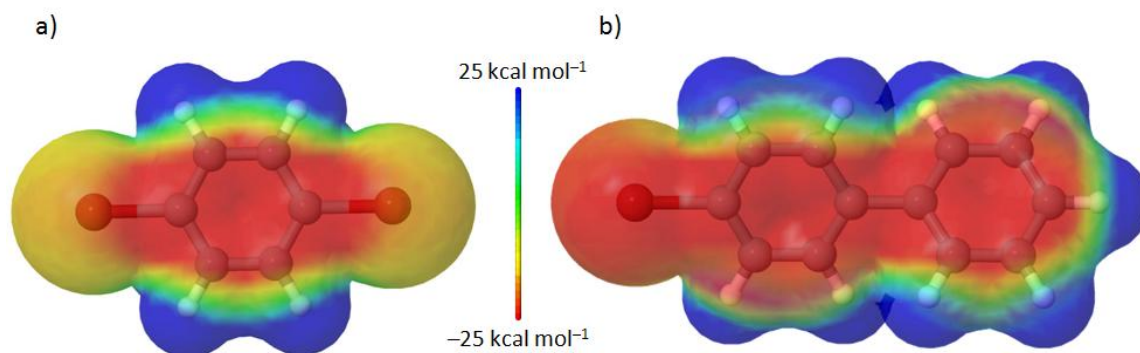
Figure 7.1. Electrostatic potential computed at HF/cc-pVTZ of a) *p*-dibromobenzene and b) 4-bromobiphenyl, the intermediate to the triaryl species formed through intramolecular oxidative addition.

We then examined the effect of electron donating and electron withdrawing groups added to the monomer. Methoxy groups, which are highly electron donating, were added at the 2 and 5 position of *p*-bromobenzene monomer. The cross-coupling reaction formed 100% triaryl species, indicating intramolecular oxidative addition. The electrostatic potential, depicted in Figure 7.2a, shows the ring to have a largely negative value, which facilitates palladium complexation. Next, a single electron withdrawing group, methyl ester, was added to the 2 position of the *p*-bromobenzene monomer. Still, 100% of triaryl species were formed. In an attempt to further decrease the electron density of the benzene ring a second methyl ester group was added at the 5 position. Even with this additional unit, 100% of triaryl species was formed upon cross-coupling.

Both of the methyl ester results can be explained by examing the electrostatic potential. Figures 7.2b and 7.2c show that the aryl rings have large negative electrostatic potentials, which indicates the presence of enough electron density to π-complex with zerovalent palladium.
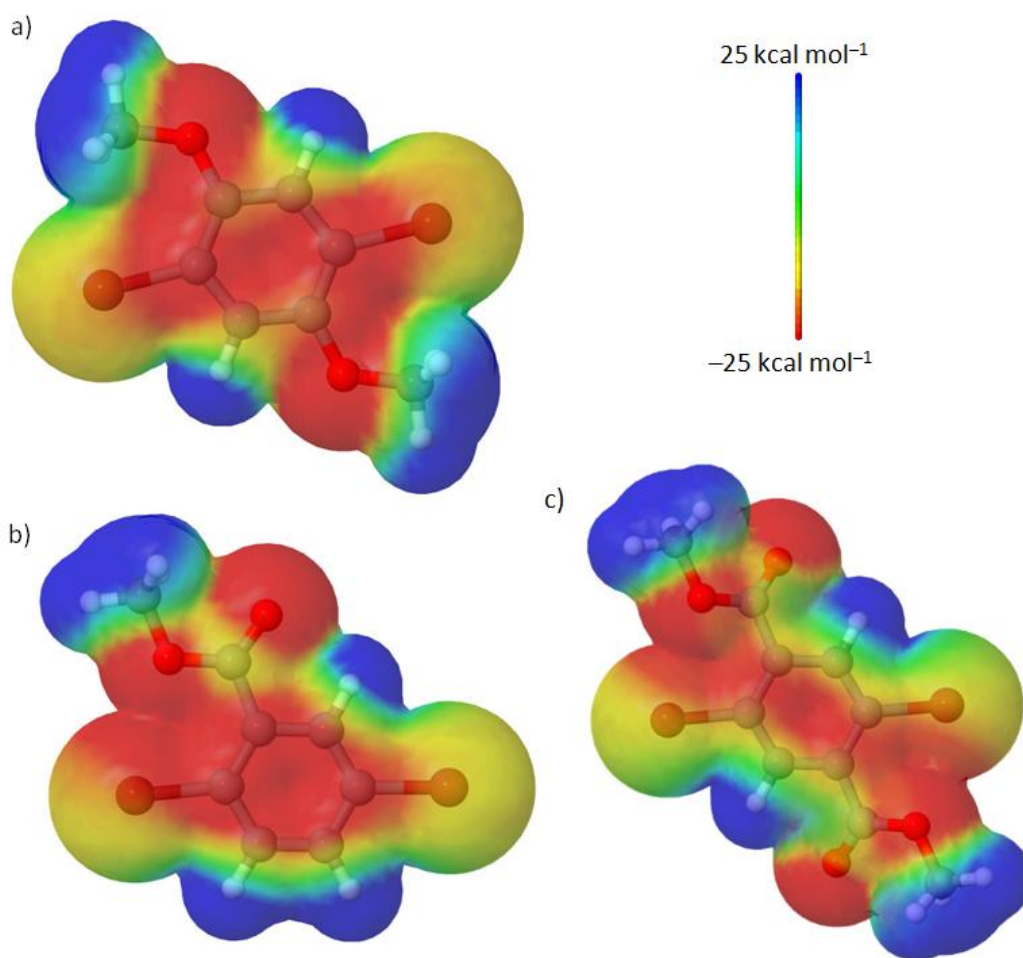
Figure 7.2. Electrostatic potential computed at HF/cc-pVTZ of a) 1,4-dibromo-2,5-dimethoxybenzene, b) methyl 2,5-dibromobenzoate, and c) dimethyl 2,5-dibromoterephthalate.

Next, fluorine atoms were added at the 2 and 5 position of *p*-bromobenzene to further remove electron density from the ring. In this case, 100% of the diaryl species was attained upon cross-coupling, which indicates intramolecular oxidative addition *does not* occur. Examining the electrostatic potential in Figure 7.3a, we find a much more positive potential than for the

previously studied molecules. Upon cross-coupling with the first aryl unit to create the biaryl species, the potential remains in the far aryl ring (Fig. 7.3b), trapping the palladium complex so that the catalyst cannot move across the ring to achieve intramolecular oxidative addition.
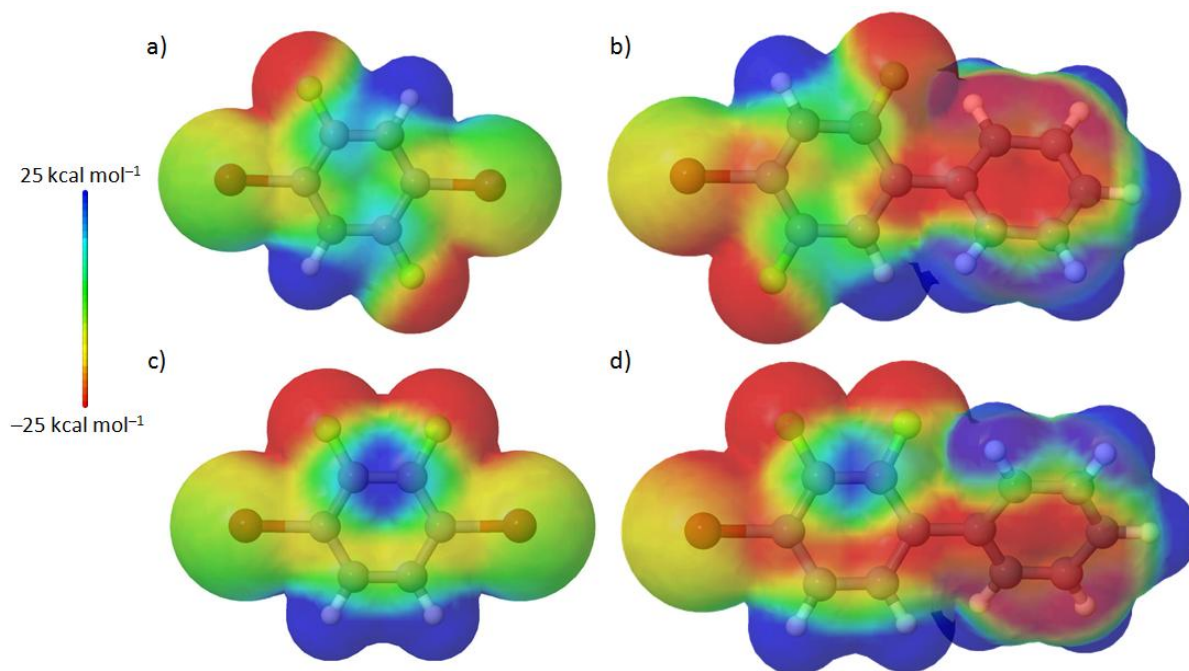
Figure 7.3. Electrostatic potential computed at HF/cc-pVTZ of a) 1,4-dibromo-2,5-difluorobenzene, its diaryl derivative b) 4-bromo-2,5-difluorobiphenyl, c) 1,4-dibromo-2,3-difluorobenzene, and its diaryl derivative d) 4-bromo-2,3-difluorobiphenyl.

When both fluorine atoms are placed on the same side of the ring, as in 1,4-dibromo-2,3-difluorobenzene, 100% of the triaryl product is formed. The electrostatic potential map in Figure 7.3c shows a localized withdrawing effect on the side of the ring which contains the fluorine atoms. The other side of the ring maintains a small negative electrostatic potential. This potential is amplified in the biaryl product (Fig. 7.3d). Presumably, the zerovalent palladium can ring-walk along the non-substituted edge of the fluorinated ring to undergo intramolecular oxidative addition.

Influence of Sterics on the Stille Mechanism

In the Stille catalytic system the transmetalation step is retarded when compared with transmetalation in KCTP. Ariafard *et al.* claim this to be a result of the large P^tBu_3 ancillary ligand blocking the complexion site of the organotin reagent.[16] Through examination of the Stille reaction with DFT computations, they showed that PPh_3 and PMe_3 ancillary ligands lowered energetic barriers for the transmetalation step when compared with P^tBu_3. In fact, the barriers were lowered enough for the rate-limiting step to switch from transmetalation to oxidative addition. Additionally, they found that truncating the ligand to PMe_3 does not produce accurate energetic profiles and stressed the importance of computing the geometry of the entire ligand.

So far, research into the steric influence of a ligand on various aspects of a reaction has been based on comparative studies where an entire reaction must be painstakingly mapped out with multiple ligands in order to make any determinations on mechanistic influence.[16,23] However, using our exact solid angle method,[24] discussed in Chapter 3, the sterics of a reaction can be directly correlated to the reaction profile. Thus, the reaction need only be mapped out a single time.

To do this, the exact solid angle ($\Omega°$) of the computed geometry for each step in the reaction is measured. Then the $\Omega°$ of each ligand separately is measured separately. Solid angles are additive when there is no overlap,[25] thus subtracting $\Omega°$ for the total and $\Omega°$ for the sum of separated ligands gives the amount of ligand overlap present in the system. This value can be turned into a percentage through use of the G-parameter.[26]

The overlap correlates to steric congestion, which drives certain reaction steps. For example, reductive elimination is known to be accelerated by sterically demanding ancillary ligands which force the geometry to resemble the coupling transition state.[27] By comparing the

change in overlap with the relative energy of the complex, the steps in the reaction that are dependent on sterics are made clear. If the overlap follows the energetic trends, one can assume increasing the steric size would increase the relative energy. If the overlap does not follow, changing the sterics of the system will have no affect on the reaction.

To test this hypothesis, I followed Ariafard's research of the Stille reaction with PhCl and (vinyl)SnMe$_3$ catalyzed by Pd(^{t}Bu$_3$).[16] It should be noted that their study did not include solvent, which could potentially coordinate with the palladium center, changing the geometries and relative energies of the various complexes during the reaction cycle.[28,29] Figure 7.4 shows the reaction profile, listing the relative energies and percent overlap for each complex.
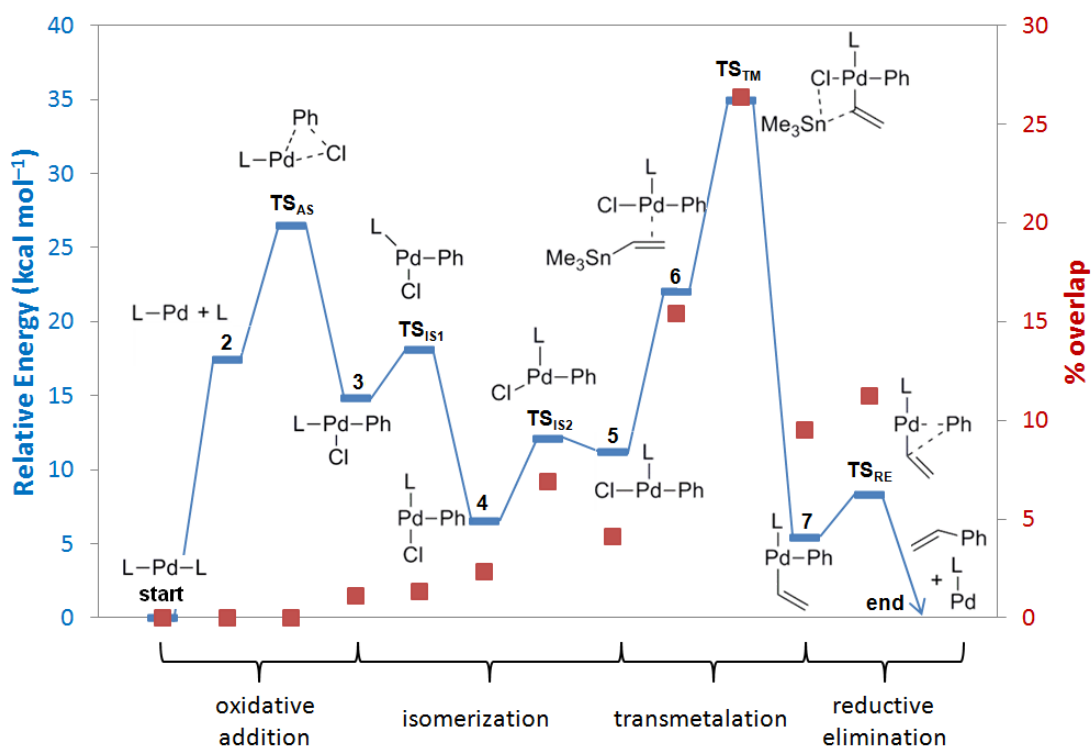
Figure 7.4. Steric and energetic reaction profile of the Stille Coupling reaction where L is P^{t}Bu$_3$. Relative energies, taken from Ref. 16, are shown as blue bars and corresponds to the left y-axis. The percent overlap in the complex is shown by red squares and corresponds to the right y-axis.

The percent overlap within the complex at each point in the reaction corresponds well with both the transmetalation and reductive elimination steps, which suggests, as supported by Ariafard's comparative studies, these reaction steps are influenced by steric crowding. The oxidative addition step, which did not change for various ancillary ligands in the Ariafard study, does not correlate with percent overlap, which confirms that this step is not influenced by sterics.

In the oxidative addition step, ligands do not overlap until the final product, and even then the overlap is only 1.3%. Crowding begins in the isomerization step, especially in intermediate **4** when the P^tBu_3 and phenyl units are adjacent. The isomerization step has the potential to block certain reaction pathways and if too energetically unfavorable may slow the reaction.[30] Figure 7.5 visualizes the overlap area of the P^tBu_3 and phenyl ligands in the solid angle of **4**, which corresponds to 2.3%. From there, the percent overlap begins to track the energetics of the reaction.
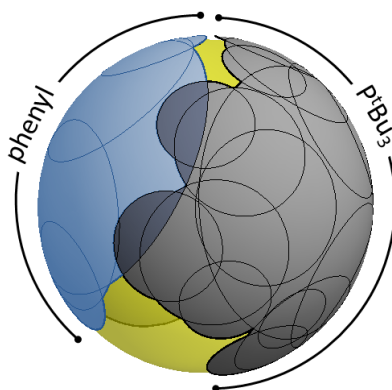
Figure 7.5. Solid angle visualization of the isomerization intermediate **4** in the Stille reaction. P^tBu_3 is shown in gray, phenyl in blue, and the overlap area in dark blue.

The transition state corresponding to the transmetalation step (TS_{TM}) is the highest in energy (34.9 kcal mol^{-1}) and is the rate-determining step in the reaction ($\Delta E = 12.9$ kcal mol^{-1}).[16] The steric overlap at this point is also greatest (26.4%), indicating the barrier is directly

influenced by steric interactions within the complex. Figure 7.6 visualizes the extensive overlap in the transition state to transmetalation. A larger ligand would increase the barrier to transmetalation creating a hindrance at the site of association and a smaller ligand would decrease the barrier by allowing more room for the organotin reagent to complex, which is precisely what was found in Ariafard's comparative study.
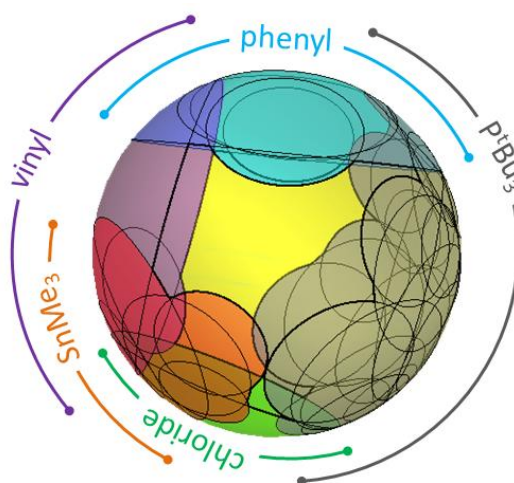
Figure 7.6. Solid angle visualization of the transmetalation transition state TS_{TM} in the Stille reaction. P^{t}Bu$_3$ is shown in gray, phenyl in blue, vinyl in purple, SnMe$_3$ in orange, and chloride in green. Overlap areas are a mixture of the overlapping colors.

The energetics in the reductive elimination steps are also tracked by percent overlap. In this case, the steric overlap was not as influential on the energetics. The relative energies are low (5.4 and 8.3 kcal mol^{-1} for the transmetalation reactant and transition state),[16] while the overlap is moderate (9.5 and 11.3%). In this case a larger ligand would slightly lower the barrier to reductive elimination, which has been shown in previous reports.[31]

Conclusions

Intramolecular oxidative addition in the Stille cross-coupling reaction was examined experimentally by small molecule competition reactions. The ability to maintain association with the aryl substrate after reductive elimination correlated to a highly negative electrostatic potential around the aromatic ring. Substrates with more positive electrostatic potentials, such as 1,4-dibromo-2,5-difluorobenzene and 1,4-dibromo-2,3,5,6-tetrafluorobenzene, do not undergo intermolecular oxidative addition. Even if only one side of the ring is available to the palladium, such as in 1,4-dibromo-2,3-difluorobenzene, intramolecular oxidative addition still occurs. By computing the electrostatic potential of a potential substrate, monomer scope for the Stille catalyst-transfer polymerization can be examined before performing physical experiments.

The technique of measuring the sterics at each step in a reaction holds for any mechanism in which there is a central atom.[24] Using a previous study on the mechanism of Stille coupling as a guide,[16] steps which are influenced by sterics, transmetalation and reductive elimination, are plainly seen by examining the percent overlap at each step in the mechanism. If other transition-metal catalyzed cross-coupling mechanisms are explored in this manner, the role of sterics on these reactions can be further elucidated, which could lead to better catalyst design and more controlled polymerization reactions.

References

(1) Littke, A. F.; Fu, G. C. *Angew. Chem. Int. Ed.* **1999**, *38*, 2411-2413.

(2) Littke, A. F.; Schwarz, L.; Fu, G. C. *J. Am. Chem. Soc.* **2002**, *124*, 6343-6348.

(3) Kang, S.; Ono, R. J.; Bielawski, C. W. *J. Am. Chem. Soc.* **2013**, *135*, 4984-4987.

(4) Huddleston, N. E.; Sontag, S. K.; Bilbrey, J. A.; Sheppard, G. R.; Locklin, J. *Macromol. Rapid Commun.* **2012**, *33*, 2115-2120.

(5) Stille, J. K. *Angew. Chem. Int. Ed.* **1986**, *25*, 508-524.

(6) Mitchell, T. N. *Synthesis* **1992**, *1992*, 803-815.

(7) Huddleston, N. E. *Metal-mediated interfacial cross coupling reactions: the development of new strategies and catalysts for the preparation of conjugated polymer films*, Ph.D. Thesis, University of Georgia, 2013.

(8) Dong, C.-G.; Hu, Q.-S. *J. Am. Chem. Soc.* **2005**, *127*, 10006-10007.

(9) Zenkina, O. V.; Karton, A.; Freeman, D.; Shimon, L. J. W.; Martin, J. M. L.; van der Boom, M. E. *Inorg. Chem.* **2008**, *47*, 5114-5121.

(10) Bryan, Z. J.; McNeil, A. J. *Chem. Sci.* **2013**, *4*, 1620-1624.

(11) Hartwig, J. F. *Angew. Chem. Int. Ed.* **1998**, *37*, 2046-2067.

(12) Galardon, E.; Ramdeehul, S.; Brown, J. M.; Cowley, A.; Hii, K. K.; Jutand, A. *Angew. Chem. Int. Ed.* **2002**, *41*, 1760-1763.

(13) Li, Z.; Fu, Y.; Guo, Q.-X.; Liu, L. *Organometallics* **2008**, *27*, 4043-4049.

(14) Espinet, P.; Echavarren, A. M. *Angew. Chem. Int. Ed.* **2004**, *43*, 4704-4734.

(15) Lam, K. C.; Marder, T. B.; Lin, Z. *Organometallics* **2006**, *26*, 758-760.

(16) Ariafard, A.; Yates, B. F. *J. Am. Chem. Soc.* **2009**, *131*, 13981-13991.

(17) Dill, J. D.; Pople, J. A. *J. Chem. Phys.* **1975**, *62*, 2921-2923.

(18) Francl, M. M.; Pietro, W. J.; Hehre, W. J.; Binkley, J. S.; Gordon, M. S.; DeFrees, D. J.; Pople, J. A. *J. Chem. Phys.* **1982**, *77*, 3654-3665.

(19) Lee, C.; Yang, W.; Parr, R. G. *Phys. Rev. B* **1988**, *37*, 785-789.

(20) Dunning, T. H. *J. Chem. Phys.* **1989**, *90*, 1007-1023.

(21) Schmidt, M. W.; Baldridge, K. K.; Boatz, J. A.; Elbert, S. T.; Gordon, M. S.; Jensen, J. H.; Koseki, S.; Matsunaga, N.; Nguyen, K. A.; Su, S.; Windus, T. L.; Dupuis, M.; Montgomery, J. A. *J. Comp. Chem.* **1993**, *14*, 1347-1363.

(22) Becke, A. D. *J. Chem. Phys.* **1993**, *98*, 5648-5652.

(23) Kozuch, S.; Martin, J. M. L. *ACS Catalysis* **2011**, *1*, 246-253.

(24) Bilbrey, J. A.; Kazez, A. H.; Locklin, J.; Allen, W. D. *J. Chem. Theory Comput.* **2013**, *9*, 5734–5744.

(25) White, D.; Taverner, B. C.; Leach, P. G. L.; Coville, N. J. *J. Comp. Chem.* **1993**, *14*, 1042-1049.

(26) Guzei, I. A.; Wendt, M. *Dalton Trans.* **2006**, *0*, 3991-3999.

(27) van Leeuwen, P. W. N. M.; Kamer, P. C. J.; Reek, J. N. H.; Dierkes, P. *Chem. Rev.* **2000**, *100*, 2741-2770.

(28) Casado, A. L.; Espinet, P.; Gallego, A. M. *J. Am. Chem. Soc.* **2000**, *122*, 11771-11782.

(29) Casares, J. A.; Espinet, P.; Salas, G. *Chem. Eur. J.* **2002**, *8*, 4843-4853.

(30) Pérez-Temprano, M. n. H.; Gallego, A. M.; Casares, J. A.; Espinet, P. *Organometallics* **2011**, *30*, 611-617.

(31) Hartwig, J. F.; Richards, S.; Barañano, D.; Paul, F. *J. Am. Chem. Soc.* **1996**, *118*, 3626-3633.

CHAPTER 8

CONCLUSIONS AND OUTLOOK

Overall Conclusions

This work has focused on mechanistic aspects of transition metal catalyzed cross-coupling reactions, specifically the Kumada and Stille reactions. Both methods can be amended to chain-growth polymerizations to produce conjugated polymers of narrow dispersity and controlled end groups.[1-3] Each mechanism relies on a repeated cycle of oxidative addition of a zerovalent group 10 metal into the halogen-aryl bond of the substrate, transmetalation of a monomer with suitable metalating substituent (a Grignard reagent for Kumada and an organotin reagent for Stille), and reductive elimination of the newly coupled molecule.

Ancillary ligands have been shown to play a large role in polymerization, altering the catalyst resting state and kinetics of reaction.[4,5] Thus, we have developed two methods for quantifying the sterics of ligands: the exact cone angle and the exact solid angle.[6-8] The mathematical formulation and computational testing are presented in Chapters 2 and 3. Both methods build on previous ligand steric descriptors. The exact cone angle is an extension of the Tolman cone angle that has been expanded to include any type of ligand bound to any atom center, whereas before the cone angle was limited to monodentate phosphine and amine ligands.[9] The exact solid angle improves on the mathematics of previous solid angle formulations.[10-12] Programs created in *Mathematica* and freely available on the Internet at http://www.ccqc.uga.edu/references/software.php (as of 2014), require only the atomic radii of

included atoms and the Cartesian coordinates of the complex, determined experimentally by crystallography or through computational studies. The cone angle still suffers from the limitation of describing the ligand as a right, circular cone, meaning entirely symmetrical. This is valid for freely rotating ligands, but not as accurate for rotationally confined ligands such as multidentate ligands. In that case, the solid angle should be used to describe the ligand sterics.

Deviations from ideal polymerization, as shown for the Kumada system in Chapter 4, stem from a homocoupling side reaction, termed disproportionation.[13] The likelihood for an initiating complex to undergo disproportionation comes at least in part from the choice in ancillary ligand and can be quantified by the thermodynamic energy of reaction, termed disproportionation energy. Complexes with a lower disproportionation energy more easily undergo disproportionation and result in uncontrolled end groups and widened dispersity. Previously reported dispersities are compared to the disproportionation energy of the initiating complex and found to follow the same trend, which suggest that disproportionation is the main cause for an increase in dispersity in the Kumada system.

Kumada coupling is discussed in more detail in Chapters 5 and 6. These chapters focus on mechanistic aspects of a key step in such coupling reactions: intramolecular oxidative addition. Without the formation of some type of associated pair between the zerovalent nickel catalyst and the aryl substrate, polymerization would not be chain-growth in manner.[14,15] Thus, the focus of Chapters 5 and 6 are the identification of this associated pair and the mechanism of intramolecular oxidative addition. Both chapters use a standard ligand, diphenylphosphino propane (dppp), involved in the nickel complex and, instead, focus on monomer scope of Kumada coupling and accurate modeling techniques.

In Chapter 5 a combination of experimental and theoretical techniques are used to show that the association is a π-complex between the nickel catalyst and aryl substrate. The nickel initially associates with the aryl substrate then "walks" around the ring. Reaction barriers to such ring-walking are, in general, below 10 kcal mol^{-1} for a variety of benzene- and thiophene-based substrates. After ring-walking, intramolecular oxidative addition occurs with barriers below 15 kcal mol^{-1}.

Chapter 6 outlines the geometric profile of ring-walking and nickel insertion for two six-membered rings, 1-bromo-2-methylbenzene and 2-bromopyridine, and two five-membered rings, 2-bromo-3-methylthiophene and 2-bromopyrrole. The ring-walking mechanism is fundamentally different for six-membered and five-membered rings. In the six-membered systems, the nickel catalyst moves in a three-coordinate transition state alone each face of the ring. In the five-membered systems, the catalyst transverses the ring, moving from one carbon-carbon double bond to the other across the ring. The role of dispersion and effect ancillary ligand truncation in modeling the system is also discussed.

Finally, Chapter 7 focuses on the Stille cross-coupling reaction. The main difference between Stille cross-coupling and Kumada cross-coupling is the use of a zerovalent palladium, rather than nickel, and an organotin metalating agent, rather than a Grignard reagent. Again the intramolecular oxidative addition reaction is examined, but this time through small molecule competition reactions. The reaction was carried out with equal equivalents of dibromonated monomer and metalating agent, both aryl species. If the palladium diffuses away after coupling the two species, more monomer will be initiated and the majority of product will be diaryl species. If the palladium stays in association with the aryl species, a triaryl system will be formed. The ability to stay in association with a monomer can be examined computationally through

electrostatic potential maps. Species with highly negative areas of electrostatic potential around the ring are able to hold the palladium complex in association to cause intramolecular oxidative addition. Species with positive areas of electrostatic potential do not retain the palladium and intramolecular oxidative addition does not occur. Additionally, the exact solid angle descriptor from Chapter 3 can be used to show which steps in the Stille cross-coupling reaction are influenced by sterics by measuring the amount of overlap between the ligands in the palladium complex. By this method, the transmetalation and reductive elimination steps are most influenced by sterics, as shown in previous reports.[16,17]

Future Work

As the methods developed in Chapters 2 and 3 can be applied to any complex with an atomic center, the sterics of majority of transition-metal catalyzed cross-coupling reactions can be explored by the exact cone angle and exact solid angle. Quantifying the sterics can be used in conjunction with energetic computations to determine which steps in the catalytic cycles are influenced by sterics. For the first time, the change in steric size of ancillary ligands in a complex can be studied throughout a reaction. This may elucidate additional details of how ancillary ligands effect a reaction while not explicitly being involved.

An array of methods are presented in Chapters 4–7 to elucidate reaction mechanisms and guide the creation of an optimized catalyst in transition metal catalyzed cross-coupling reactions. Computing disproportionation energy, as discussed in Chapter 4, can help determine the appropriate ancillary ligand to use so that harmful side reactions are minimized. The kinetic isotope effect in conjunction with energetic reaction profiles, shown in Chapter 5, helps determine substrate scope by understanding the energetics involved in π-complexation and

intramolecular oxidative addition. This method can also be used to test whether a new catalyst will produce controlled polymerization. Chapter 6 details explicit mechanistic aspects and computational details involved in computing such reaction profiles. The computed electrostatic potentials in Chapter 7 can be used to test substrates for an optimal density for intramolecular oxidative addition to occur.

The polymerization of n-type materials is hindered by the low electron density in the monomer, which causes the catalyst to diffuse from the growing chain rather than undergo intramolecular oxidative addition. The computational tools presented in this thesis could be used to predict an optimized a monomer and catalyst system for chain-growth polymerization without performing a single wet experiment.

Final Remarks

This thesis focuses on using computational methods to elucidate the mechanisms of two prominent cross-coupling reactions, Kumada coupling and Stille coupling. Chapters 2 and 3 present new methods to quantify sterics about an atom center, which are later applied to cross-coupling systems. Additionally, intramolecular oxidative addition is examined and shown to occur for both systems. Computational methods were used to verify experimental findings in Chapters 4, 5, and 7, while Chapter 6 expounds on the mechanism of ring-walking in the Kumada system. The computational methods presented herein could also be used before experiment as a predictive measure of ligand or substrate scope, as well as predicting if a catalytic complex will undergo intramolecular oxidative addition and, thus, if it would be suitable for polymerization. By first examining reaction systems computationally, the "brute force" method of experimental chemistry can be avoided.

References

(1) Kiriy, A.; Senkovskyy, V.; Sommer, M. *Macromol. Rapid Commun.* **2011**, *32*, 1503-1517.

(2) Bryan, Z. J.; McNeil, A. J. *Macromolecules* **2013**.

(3) Littke, A. F.; Fu, G. C. *Angew. Chem. Int. Ed.* **1999**, *38*, 2411-2413.

(4) Miyakoshi, R.; Yokoyama, A.; Yokozawa, T. *J. Polym. Sci., Part A: Polym. Chem.* **2008**, *46*, 753-765.

(5) Lanni, E. L.; Locke, J. R.; Gleave, C. M.; McNeil, A. J. *Macromolecules* **2011**, *44*, 5136-5145.

(6) Bilbrey, J. A.; Allen, W. D. In *Annual Reports in Computational Chemistry*; Ralph, A. W., Ed.; Elsevier: 2013; Vol. Volume 9, p 3-23.

(7) Bilbrey, J. A.; Kazez, A. H.; Locklin, J.; Allen, W. D. *J. Comp. Chem.* **2013**, *34*, 1189–1197.

(8) Bilbrey, J. A.; Kazez, A. H.; Locklin, J.; Allen, W. D. *J. Chem. Theory Comput.* **2013**, *9*, 5734–5744.

(9) Tolman, C. A. *Chem. Rev.* **1977**, *77*, 313-348.

(10) Immirzi, A.; Musco, A. *Inorg. Chim. Acta* **1977**, *25*, L41-L42.

(11) Taverner, B. C. *J. Comp. Chem.* **1996**, *17*, 1612-1623.

(12) White, D.; Taverner, B. C.; Leach, P. G. L.; Coville, N. J. *J. Comp. Chem.* **1993**, *14*, 1042-1049.

(13) Bilbrey, J. A.; Sontag, S. K.; Huddleston, N. E.; Allen, W. D.; Locklin, J. *ACS Macro Lett.* **2012**, *1*, 995-1000.

(14) Iovu, M. C.; Sheina, E. E.; Gil, R. R.; McCullough, R. D. *Macromolecules* **2005**, *38*, 8649-8656.

(15) Miyakoshi, R.; Yokoyama, A.; Yokozawa, T. *J. Am. Chem. Soc.* **2005**, *127*, 17542-17547.

(16) Ariafard, A.; Yates, B. F. *J. Am. Chem. Soc.* **2009**, *131*, 13981-13991.

(17) Hartwig, J. F.; Richards, S.; Barañano, D.; Paul, F. *J. Am. Chem. Soc.* **1996**, *118*, 3626-3633.

Thank you for reading.